P-ISSN 0126-3188
E-ISSN 2443-3926

BRIN
BADAN RISET
DAN INOVASI NASIONAL

METALURGI

VOLUME 37 ISSUE 3, DECEMBER 2022
SCIENTIFIC JOURNAL ACCREDITATION NUMBER NO.3/E/KPT/2019

National Research and Innovation Agency

Publisher :
National Research and Innovation Agency (BRIN)
Kawasan Puspiptek Serpong, Tangerang Selatan, Banten, Indonesia, 15314
E-mail: ejurnalmetalurgi@mail.lipi.go.id

Science and technology magazine, regularly published every year; one volume consists of 3 editions

METALURGI

VOLUME 37 NUMBER 3, DECEMBER 2022

P-ISSN 0126-3188
E-ISSN 2443-3926

ACCREDITATION : SK No. 3/E/KPT/2019

PREFACE

Thanks to Allah SWT, the Metalurgi Journal, Volume 37 Number 3, December 2022, could present six articles.

Miftakhur Rohmah and colleagues conducted research on the Effect of Nickel Addition and Quench-Temper Process on Mechanical and Corrosion Properties of ASTM A588 Weathering Steel. The second paper, Anodizing-Electrodeposition Hybrid Coating by Using Synthesized Natrium Silicate and Zirconium Oxide on the Surface Magnesium AZ31B, was presented by Aprilia Erryani and colleagues. Aptri Mira and colleagues presented Morphology and Resistivity Values of Fluorine-Doped Tin Oxide (FTO) Using Local Dimethyl Tin Dichloride (DMTC) Precursors from Indonesia. Mochamad Afriansyah Zunaidi and his colleagues discussed The Iron Removal Process from Nickel Pregnant Leach Solution Using Sodium Hydroxide in the fourth article. Gyan Prameswara and his colleagues talked about Optimizing the Laterite Ore Grinding Process with A Ball Mill Using the Response Surface Method. Resetiana Dwi Desiati and colleagues discussed the Structure, Mechanical Properties, and Oxidation Resistance of Mn-Rich Fe-Mn-Al Alloys in their six article.

The publication of this volume in the Metalurgi Journal should, hopefully, help to advance research in Indonesia.

EDITORIAL

METALURGI
ISSN 0126 – 3188 Vol. 37 No. 3 December 2022
Keywords sourced from articles. This abstract is reproduced without permission or fee.

UDC (OXDCF) 553.4

Miftakhur Rohmah[a], Gilang Ramadhan[b], Dedi Irawan[a], Dedi Pria Utama[a], Toni Bambang Romijarso[a] ([a] Research Center for Metallurgy, National Research and Innovation Agency, [b] Departments of Metallurgical and Materials Engineering, Institut Teknologi Kalimantan)

Metalurgi, Vol. 37 No. 3 December 2022

Effect of Nickel Addition and Quench-Temper Process on Mechanical and Corrosion Properties of ASTM A588 Weathering Steel

Mechanical improvement and "self-protection" properties are mainly needed to develop weather-resistant steel materials. In this study, A588 steel was given thermomechanical treatment (hot-rolling) followed by a quenching-tempering process. The A588 steel is modified by adding 1, 2, and 3 wt.% nickel to the primary alloy. Steel is made using a hot rolling process at 1050 ℃ for 1 hour with 70% thickness reduction. The sample is heat-treated at 850 ℃ temperature for 1 hour and quenched in water, oil, and open air. The tempering process is conducted at 400 ℃ for 30 minutes. The metallography test confirmed the final microstructural and compared it with CCT (continuous cooling transformation) by Jmatpro simulation result. The fast cooling (water and oil quenchant) followed by the tempering process produces tempered martensite, ferrite, and pearlite, while the air-cooled forms a ferrite-pearlite. The cooling rate significantly affects strength and hardness and the nickel addition on hardness, and both factors have no significant on ductility. The sample owns the highest tensile strength value (~1226 MPa) with 1 %Ni, and the highest ductility value (around 17.1–27.43%) is obtained by air cooling. With 3% Ni, the corrosion rate decreases to 0.072 MPY with -432.5 mV for corrosion potential and 0.12μA/cm^{-2} for current density.

Keywords: A588, tempered martensite, cooling medium, nickel addition, quench-temper

METALURGI
ISSN 0126 – 3188 Vol. 37 No. 3 December 2022
Keywords sourced from articles. This abstract is reproduced without permission or fee.

UDC (OXDCF) 669.723

Aprilia Erryani[a], Bunga Rani Elvira[a], Syifa Ranggayoni Nurbaiti[b], Amalia Syahiddah[b], Hafsah Mujahidah[b], Yudi NugrahaThaha[a], Esmar Budi[b] ([a]Research Center for Metallurgy National Research and Innovation Agency, [b]Fisika, Universitas Negeri Jakarta)

Metalurgi, Vol. 37 No. 3 December 2022

Anodizing-Electrodeposition Hybrid Coating by Using Synthesized Natrium Silicate and Zirconium Oxide on The Surface Magnesium AZ31B

In this study, sodium silicate was synthesized, and zirconia was characterized as a suspension solution for anodization and electrodeposition processes. The results of the FTIR (fourier transform infrared) synthesis demonstrated the success of producing Na_2SiO_3 with the appearance of absorption from functional groups such as silanol (Si-OH) and siloxane (Si-O-Si) According to the SEM (scanning electron microscope) data, each batch contains oxygen, sodium, and silicon, indicating that Na_2SiO_3 was successfully synthesized without any detectable impurities. SEM images revealed that the calcination of $ZrOCl_2.8H_2O$ was dominated by zircon elements, with batch 3 having the highest zircon content at 88.81%. The XRD (x-ray diffraction) results show that ZrO_2 (monoclinic) dominates, with Cl_2 present in batches 1 and 3. As a result, the ZrO_2 used without calcination is in batch 3. Anodizing and electrodeposition processes can be performed in three ways: a. anodizing, b. two steps (anodizing-electrodeposition), and c. one step hybrid (anodizing and electrodeposition) with the addition of Al_2O_3 and $Na_2O_7SiO_3$ elements to the electrolyte. After coating, the surface of magnesium appears to be a pale white line. SEM images revealed that all three methods are coated and contain elements such as O, Na, Mg, Zr, Si, K, and Al in method c. The three samples also revealed that the sanding process was not optimal and that the Zr particles on the surface were not evenly distributed.

Keywords: Anodizing, electrodeposition, ZrO_2, sodium silicate, magnesium

METALURGI
ISSN 0126 – 3188 Vol. 37 No. 3 December 2022
Keywords sourced from articles. This abstract is reproduced without permission or fee.

UDC (OXDCF) 553.95

Aptri Mira Rizki[1], Fariza Eka Yunita[2], Latifa Hanum Lalasari[2], Januar Irawan[2], Tri Arini[2], F.Firdiyono[2], Akhmad Herman Yuwono[4], Lia Andriyah[2], Nadia Chrisayu Natasha[2] ([1]Department of Chemistry, Sebelas Maret University (UNS), [2]Research Center for Metallurgy, National Research and Innovation Agency, Department of Metallurgical and Materials Engineering, Universitas Indonesia)

Metalurgi, Vol. 37 No. 3 December 2022

Morphology and Resistivity Values of Fluorine-Doped Tin Oxide (FTO) Using Indonesian Local Dimethyl Tin Dichloride (DMTC) Precursors

TCO (transparent conductive oxide) is the main component for solar cell fabrication. One of the promising types of TCO is FTO (fluorine-doped tin oxide). The method used in depositing the conductive layer of FTO is spray pyrolysis with an ultrasonic nebulizer. The precursor used is a local Indonesian product, DMTC (dimethyltin dichloride) with doping ammonium fluoride (NH_4F). The variable that used in this study were variations in deposition time (5, 10, 15, 20, and 25 minutes) with a fixed substrate temperature at 300 °C and doping variations (un-doped, 2 wt.% doped, and 8 wt.% doped) to see the effect of adding F doping to the precursor solution. The resistivity values with a variation of deposition time 5, 10, 15, 20, and 25 minutes (2 wt.% doped) are $0.218x10^{0}$; $0.449x10^{-1}$; $1,567x10^{-2}$; $0.676x10^{-2}$ $0.377x10^{-2}$ Ω.cm. For doping variations (un-doped, 2 wt.% doped, and 8 wt.% doped) the values are $0.883x10^{-2}$; $0.377x10^{-2}$; $0.506x10^{-3}$ Ω.cm. The resistivity values tend to decrease with an increase in deposition time and doping addition, resulting in enhanced conductivity. The grain size will increase as deposition time and doping are both increased. In this study, the optimal resistivity value of $0.377x10^{-2}$.cm was obtained at a deposition time of 25 minutes with 2 wt.% doping.

Keywords: FTO (fluorine-doped tin oxide), DMTC (dimethyltin dichloride), deposition time, doping, resistivity

METALURGI
ISSN 0126 – 3188 Vol. 37 No. 3 December 2022
Keywords sourced from articles. This abstract is reproduced without permission or fee.

UDC (OXDCF) 553.4

Mochamad Afriansyah Zunaidi[a], Iwan Setiawan[b], Soesaptri Oediyani[a], Januar Irawan[b], Ahmad Rizky Rhamdani[b], Adi Noer Syahid[b] ([a]Metallurgical Engineering, Faculty of Engineering, University of Sultan Ageng Tirtayasa, [b]Research Center for Metallurgy, National Research and Innovation Agency)

Metalurgi, Vol. 37 No. 3 December 2022

Iron Removal Process from Nickel Pregnant Leach Solution Using Sodium Hydroxide

Indonesia is a country that has abundant mineral resources, including nickel resources in laterite ore. Nickel demand has risen significantly because of the need for nickel precursors for battery production. Nickel laterite can be processed via the hydrometallurgical route to obtain nickel precursor by leaching the laterite ore with an acid solution to produce a nickel-rich solution or PLS (pregnant leach solutions). This nickel-rich solution is then precipitated with a base solution to produce MHP hydroxides (mixed hydroxides precipitate). MHP is the primary product containing nickel and cobalt for the production of lithium battery material. PLS often contains iron impurities, which dissolve when the ore is leached. As a result, the iron must be separated in order to produce high-purity MHP. To address this issue, synthetic PLS with nickel, cobalt, and iron were created, and their concentration was simulated to match the general PLS composition. The experiment revealed that iron could be precipitated in two stages using 2.5 M NaOH solution at solution pH of 3 and 3.5. At a higher pH, nickel and cobalt can be precipitated. To investigate the effect of pH and temperature on the yield of nickel and cobalt precipitation, precipitation was carried out at pH 7, 8, and 9 and temperatures of 70, 80, and 90 °C. The results show that the highest yield was obtained at a pH of 9 and a temperature of 90 °C, with nickel and cobalt precipitation yields of 99.03% and 98.78%, respectively.

Keywords: MHP (mixed hydroxide precipitate), iron removal, pH, temperature, precipitate

METALURGI
ISSN 0126 – 3188 Vol. 37 No. 3 December 2022

UDC (OXDCF) 553.4

Gyan Prameswara, Flaviana Yohanala Prista Tyassena, Idi Amin, Husnul Hatimah (Mineral Chemical Engineering, Makassar ATI Polytechnic)

Metalurgi, Vol. 37 No. 3 December 2022

Optimization of Laterite Ore Grinding Process Using Ball Mill with Response Surface Method

This study used a CCD (central composite design) of RSM to determine the dependence and interaction between several operating conditions that affect the grinding process using a ball mill, such as the number of balls, grinding duration, and rotational speed, on particle size at 80% product mass (P80) and mineral liberation (response surface method). The grinding process was carried out in a cylindrical ball mill with a diameter and length of 18.6 cm and 21.5 cm, respectively, as well as a steel ball with a diameter of 2.5 cm and a weight of 100 grams/ball. A sieve aperture of 180-600 microns is used to analyze the particle size distribution. The optimum data for the grinding process was obtained with the smallest response value of P_{80} (513.294 μm). It was known that the number of balls and grinding duration significantly affected the reduction of the P_{80} value in the sample. The model that can describe the influence of process variables on the P_{80} value was obtained with good accuracy. The elemental concentration and the XRD (x-ray diffraction) pattern were used to determine the mineral content of the sample. Minerals with a lower hardness scale are more easily liberated and exposed. The initial material's P_{80} value was 1560.89 μm, while the P80 grinding process was reduced to 513.29 μm under optimal conditions.

Keywords: CCD (central composite design), grinding, RSM (response surface method), laterite, nickel

METALURGI
ISSN 0126 – 3188 Vol. 37 No. 3 December 2022
Keywords sourced from articles. This abstract is reproduced without permission or fee.

UDC (OXDCF) 620.16

Resetiana Dwi Desiati, Edi Sutiawan, Toto Sudiro, Bambang Hermanto (Research Center for Advanced Materials, National Research and Innovation Agency)

Metalurgi, Vol. 37 No. 3 December 2022

Structure, Mechanical Properties, and Oxidation Resistance of Mn-Rich Fe-Mn-Al Alloys

In this study, Mn-rich Fe-Mn-Al alloys with different Al content (Al = 0, 3, and 5 wt.%) were fabricated from ferromanganese lumps using a conventional powder metallurgy technique. The samples were compacted in 1 cm steel dies using a load of 8 tons and then sintered at 1100 ℃ for 2 h in a tubular furnace under a vacuum condition of around 0.5 mbar. To evaluate the effect of Al addition to Fe-Mn-Al alloy, the Archimedes principle and Vickers hardness were applied to estimate the density and hardness of the compact alloys. Moreover, the high-temperature oxidation resistance of the alloy was evaluated at 800 ℃ for 8 cycles. The structure of the alloy before and after oxidation was studied using XRD (x-ray diffractometer) and SEM-EDS (scanning electron microscope-energy dispersive spectrometry). The XRD analysis results show that the FeMn-0Al alloy is mainly composed Fe_3Mn_7 phase, with the presence of FeAl phase at 3 wt.% Al, and Al_8Mn_5 phase at 5 wt.% Al. The density and hardness of Fe-Mn-Al alloys decreased with the increased Al content. Fe-Mn-Al alloy without Al addition exhibits poor oxidation resistance since the first cycle of the test. The results of the microstructural analysis showed that although the alloy with the addition of 3 wt.% Al showed less mass gain after being exposed for 8 cycles at 800 ℃, the Fe-Mn-Al alloy with 5 wt.% tended to be more resistant to oxidation and had no cracking defects. The structure of the oxide formed on the surface of the alloy is composed of two layers (ie; outer and inner layer) which are affected by each alloy composition.

Keywords: Fe-Mn-Al alloy, conventional powder metallurgy, density, hardness, oxidation

Metalurgi (2022) 3: 87 - 96

METALURGI
Majalah Ilmu dan Teknologi
p-ISSN 0126-3188 | e-ISSN 2443-3926
ejurnalmaterialmetalurgi.lipi.go.id

EFFECT OF NICKEL ADDITION AND QUENCH-TEMPER PROCESS ON MECHANICAL AND CORROSION PROPERTIES OF ASTM A588 WEATHERING STEEL

Miftakhur Rohmah[a,*], Gilang Ramadhan[b], Dedi Irawan[a], Dedi Pria Utama[a], Toni Bambang Romijarso[a]

[a] Research Center for Metallurgy, National Research and Innovation Agency
Management Building 720, B.J. Habibie Sains and Technology Area, Banten, Indonesia 15314
[b] Departments of Metallurgical and Materials Engineering, Institut Teknologi Kalimantan
Jl. Soekarno Hatta KM 15, Balikpapan, Kalimantan, Indonesia
*E-mail: miftakhur.rohmah@brin.go.id

Received: 24-02-2022, Revised: 26-09-2022, Accepted: 31-12-2022

Abstract

Mechanical improvement and "self-protection" properties are mainly needed to develop weather-resistant steel materials. In this study, A588 steel was given thermomechanical treatment (hot-rolling) followed by a quenching-tempering process. The A588 steel is modified by adding 1, 2, and 3 wt.% nickel to the primary alloy. Steel is made using a hot rolling process at 1050 ℃ for 1 hour with 70% thickness reduction. The sample is heat-treated at 850 ℃ temperature for 1 hour and quenched in water, oil, and open air. The tempering process is conducted at 400 ℃ for 30 minutes. The metallography test confirmed the final microstructural and compared it with CCT (continuous cooling transformation) by Jmatpro simulation result. The fast cooling (water and oil quenchant) followed by the tempering process produces tempered martensite, ferrite, and pearlite, while the air-cooled forms a ferrite-pearlite. The cooling rate significantly affects strength and hardness and the nickel addition on hardness, and both factors have no significant on ductility. The sample owns the highest tensile strength value (~1226 MPa) with 1 %Ni, and the highest ductility value (around 17.1–27.43%) is obtained by air cooling. With 3% Ni, the corrosion rate decreases to 0.072 MPY with -432.5 mV for corrosion potential and 0.12μA/cm^{-2} for current density.

Keywords: *A588, tempered martensite, cooling medium, nickel addition, quench-temper*

1. INTRODUCTION

Nowadays, WS (weathering steel) is progressively popular in demand. Good weldability, high strength, and good resistance to atmospheric corrosion due to the patina layer formed are the reasons for many enthusiasts of weather-resistant steel materials. WS is designed as low-alloy steel because the carbon level is kept under 0.2%, and the total amount of alloying elements of Cu, P, Cr, Ni, Mn, and Si did not exceed 5% [1]. As a used connection for bridge steel structures, high-strength bolts are predominantly made of medium carbon alloy steel, and weathering steel is rarely used. Therefore, it is urgent to develop special high-strength bolts for the atmospheric environment. The national steel industry is expected to produce WS using local raw materials, independently. Alternative sources of high-grade iron ore, such as laterite ore processed into laterite steel, are critical to meeting Indonesia's demand for weathering steel.

The nickel content of traditional WS is generally less than 0.4%. The last study affirmed that the Ni addition of up to 1% in the conventional WS will reduce the hot shortness during the rolling process and improve the corrosion resistance [2]. Cheng et. al., [3] claimed that nickel not exceeding 3.5% induces fine crystalline formation-compact rust and increases the ratio of α/γ FeOOH in acidic and marine atmospheric. Therefore, the weathering steel design not only focuses on its weathering characteristics but should also comprehensively

DOI : 10.14203/metalurgi.v37i3.630

Metalurgi is Sinta 2 Journal (https://sinta.ristekbrin.go.id/journals/detail?id=3708) accredited by Ministry of Research & Technology, Republic Indonesia

consider the strength, elasticity, and ease of processing.

To achieve the desired combination of strength and elasticity, WS must be quenched and tempered with minimal residual stress, distortion, and crack formation. Quenching effectiveness is dependent on the steel composition, type of quenchant, or the quenchant use condition [4]. Also, the tempering temperature is one of the critical roles of microstructural evolution, carbide formation, and coarsening behavior, which influences the mechanical properties [5]-[6]. Tempering temperature, holding time, and cooling rate from the tempering temperature significantly affect steel's final properties. As the previous study, the low temperature (150 ℃) of the tempering process caused the fine carbide deposition and the phase transformation of martensite to bainite in small quantities, so it is no significant impact on strength and elongation [7]. Besides that, the influence of alloying elements on mechanical and corrosion behavior is convoluted. Chen et. al., [8] inferred that high tempering temperature causes the carbide forming element (Cr dan Mn) to be enriched in the cementite, while the non-carbide forming element (Ni) is rejected from the cementite.

Although the mechanical properties of WS can be estimated from the composition, the effect of quench-temper has few reported previously. Atapek et. al., [9] showed that the steel-tempered microstructure directly affects corrosion. When these steel are immersed in NaCl solution, the anodic dissolution starts along the amorphous grain boundary within the martensitic matrix. Martensite has a deleterious effect on electrochemical corrosion due to residual stress and the formation of micro-galvanic corrosion between martensite and the other phase [10].

In this study, the quench-temper experiment was carried out on the A-588 modified. Media quenchant variation was investigated, corresponding to the relationship between microstructure, mechanical, and corrosion properties. The primary purpose of this experiment is to provide proper media quenching at specific compositions and the development of high-strength steel to broaden its industrial application.

2. MATERIALS AND METHODS

Lateritic steel was created through the refining and re-melting of NPI (nickel pig iron). Scraps and alloying elements (ferromanganese, ferrosilicon, nickel, copper, vanadium, and tungsten) were melted in an induction furnace at 1700 - 1800 °C. The primary composition was based on the ASTM A-588 standard. The alloying effect was determined by modifying the molten metal by adding 1, 2, and 3 wt.% Ni to the primary alloy composition. Table 1 shows the chemical composition obtained from an OES (optical emission spectroscopy) test.

Table 1. Chemical composition of ASTM A588 (wt.%)

Elements	Samples Code			
	A	B	C	D
C	0.177	0.177	0.161	0.161
Al	0.02	0.05	0.19	0.016
S	0.0026	0.0024	0.0030	0.0024
Cr	0.49	0.49	0.50	0.51
Mn	1.08	1.06	1.01	1.07
Ni	0.41	1.21	1.95	2.91
P	0.011	0.001	0.014	0.001
Cu	0.32	0.34	0.32	0.32
Si	0.43	0.41	0.32	0.37
V	0.064	0.064	0.062	0.062
Fe	Bal.	Bal.	Bal.	Bal.

Casted ingot steel was homogenized at 900 ℃ for a few hours to remove a dendritic structure. The ingot was cut into 10 x 5 x 1 cm^3 of dimension, which is then used as rolling samples. The hot rolling process was performed by heating at 1050 ℃ for 1 hour. The hot rolling was carried out in 2 cycles to obtain a thickness reduction of 70% and a final plate thickness of 0.3 cm. Then, the samples were given a heat-treatment process by austenitized at 850 ℃ for 1 hour and subsequently quenched into different media to obtain martensite structure. The quenching media used are water, oil, and open air. Jmat-Pro software predicted the martensitic start temperature. In addition, the martensite and bainite start were estimated by Eq.1-2 [11]-[12]. The tempering process was conducted at 400 ℃ for 30 minutes. The sequence of heat treatment processes was schematically shown in Fig. 1.

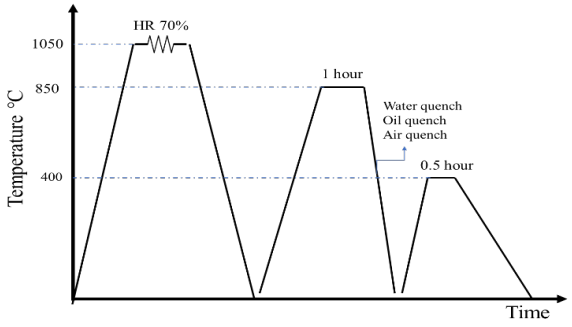

Figure 1. Schematic diagram of heat treatment process on modified laterite steel A-588

A metallographic test was used for confirmed the microstructure. Before the test, the samples were prepared by cut into 5 x 5 mm, mounted with epoxy resin, wet-ground with SiC papers (80-1200 grit gradually), and polished with alumina slurry (5 and 1 μm). After

obtaining a like mirror surface without a scratch, they were etched with a picral solution to reveal microstructure. The volume fraction of the phase was determined using the systematic manual Point Count method, prescribed in the ASTM standard E562.

$$Ms\ (^{o}C) = 539 - 423C - 30.4Mn - 12.1 - 17.7Ni - 7.5Mo\ (wt.\%) \quad (1)$$

$$Bs\ (^{o}C) = 656 - 57.7\ C - 35Mn - 75Si - 15.3Ni - 34\ Cr - 41.2Mo\ (wt.\%) \quad (2)$$

The tensile and hardness test was used to determine mechanical properties. The hardness measurement was carried out by the Brinell method with 1000 kgf of indentation for 10 seconds. The samples were prepared according to the ASTM E8 standard for the tensile test.

A polarization test confirmed the corrosion properties in NaCl 3.5% solution at room temperature. The test was conducted at the cell-system electrode. The three electrodes consist of SCE (saturated calomel) as a reference, the Platine wire as counter, and the sample as a working electrode. The swept potential was used from -200 to +200 mV with 1mV/s of scan rate.

3. Result and Discussion

3.1 CCT Diagram of Laterite Nickel-Based A588 Alloy Steel

The CCT (continuous cooling transformation) diagram shows the possibility of each alloy forming a different phase: austenite, ferrite, pearlite, bainite, and martensite. The phase distribution in all samples depends on the cooling rate, temperature, and holding time. CCT diagram images from the simulation of the JMatPro software are shown in Fig. 2.

From the CCT diagram in Fig. 2, the Ni addition significantly affects the ferrite phase (black line) formed and has little impact on other phases such as pearlite (light green line), bainite (blue line), retained austenite (dark green line) and martensite (thin purple line). The ferrite and retained austenite phases were formed with a cooling rate of 1 to 5 in sample A (Fig. 2(a)) and underwent a significant shift in sample D (Figure 2d). In Sample A, the starting line for the ferrite and austenite formation lies in the same period (cooling rate region 1).

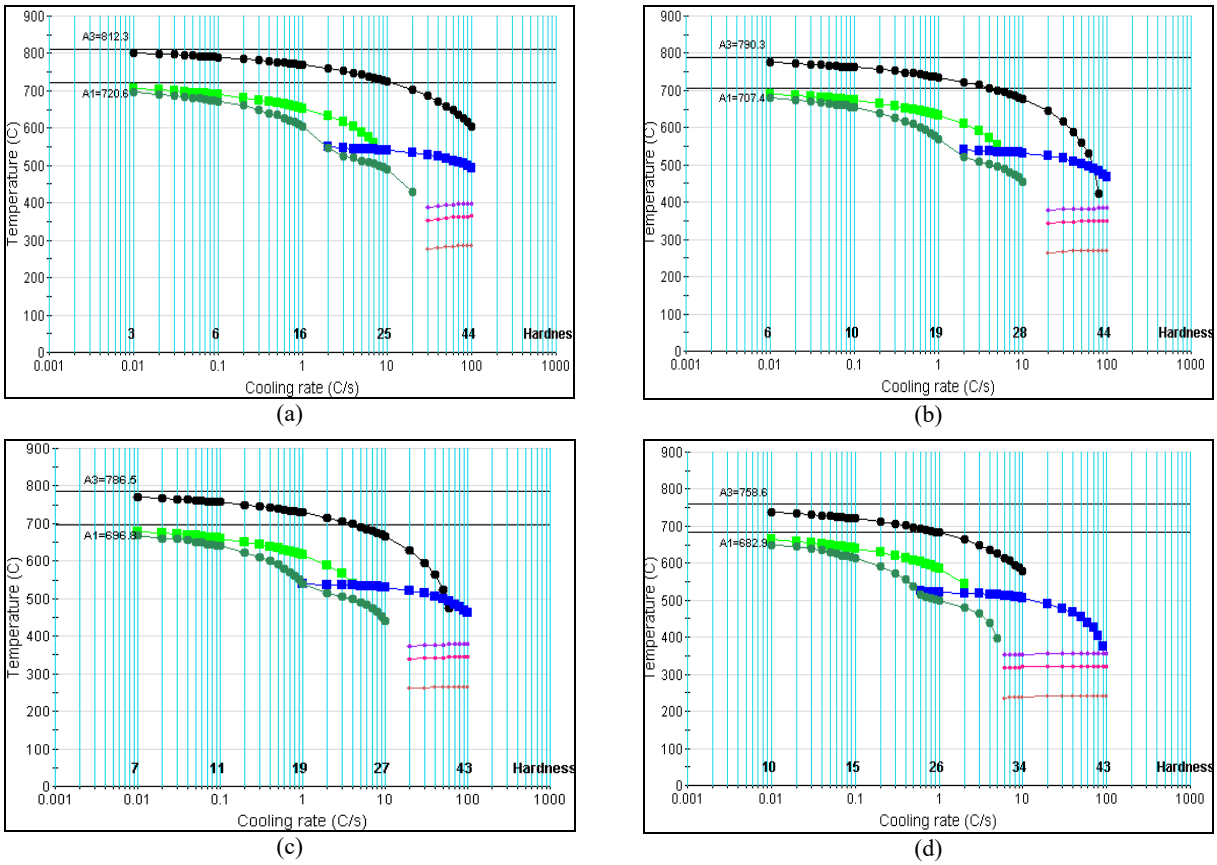

Figure 2. CCT (continuous cooling transformation) diagrams for: (a) Sample A (0.41 wt.% Ni); (b) Sample B (1 wt.% Ni); (c) Sample C (2 wt.% Ni); (d) Sample D (3 wt.% Ni)

As the Ni content increased from Sample B to Sample D, ferrite and austenite formation moved at different timescales and tended longer. The addition of 3 wt.% Ni shifted the ferrite and austenite areas towards the slower cooling rate line and increased the bainite area. As a result, ferrite and retained austenite will only form heat treatment in the cooling rate region 2 of sample D. This shift in the ferrite area towards the slower cooling rate line indicates that increasing the Ni content expands the austenite area.

Nickel is a stabilizer of austenite and can reduce the critical cooling rate of bainite formation [13]. Mo, Cr, and Ni are responsible for broadening the bainitic transformation region and obtaining bainitic fraction after quenching [14]. The presence of nickel shifts the CCT curve to the right, thus delaying the reaction of ferrite, pearlite, and bainite [7]. In this simulation, the addition of Ni will affect the formation of bainite with a range of cooling rates towards a slower cooling rate, which is around 0.6 ℃/s to 100 ℃/s. For the martensite formation, the addition of Ni in each sample resulted in a change in area by shifting the initial line of transformation to a lower temperature. Ms (Martensite Start) was calculated to be 398 ℃ for sample A and decreased to 355 ℃ for sample D. This indiciated that the low-temperature bainite was successfully attained by increasing the nickel [15]. Based on the CCT results, the initial temperatures of martensite and bainite are shown in Table 2.

Table 2. The calculated of martensite and bainite start temperature in A588 steel from JMatPro software simulation

Sample Code	Ni content (wt.%)	Martensite Start (℃)	Bainite Start (℃)
A	0.41	398	553
B	1.21	383	539
C	1.95	378	540
D	2.91	355	523

3.2 Microstructure Analysis

The microstructure of A588 steel based on nickel laterite with variations in cooling is shown in Fig. 3. Figure 3 shows the effect of media quenchant (water, oil, and open-air cooling) on the A588 microstructure after the quench-temper process. In general, the microstructure of the water-oil quenched subsequently a tempered process was consisting of tempered martensite or bainite (finer needle lathe-like structure), fine pearlite (black color lamellar structure), and ferrite (white light color). The microstructure of water quench (Fig. 3(a)) consists of 24% ferrite, 57% tempered martensite, and 19% pearlite, whereas the oil quench (Fig. 3(b)) consists of 62% tempered martensite, 22% ferrite, and 16% pearlite. This difference in phase fraction results in higher strength values and lower ductility than air cooling.

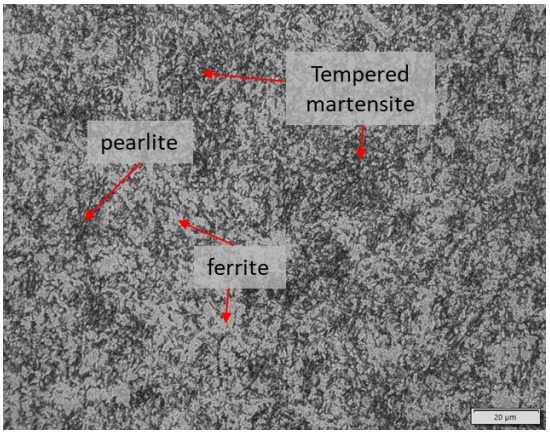

(a)

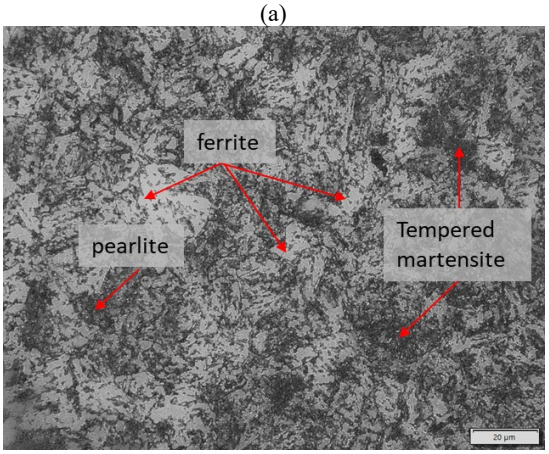

(b)

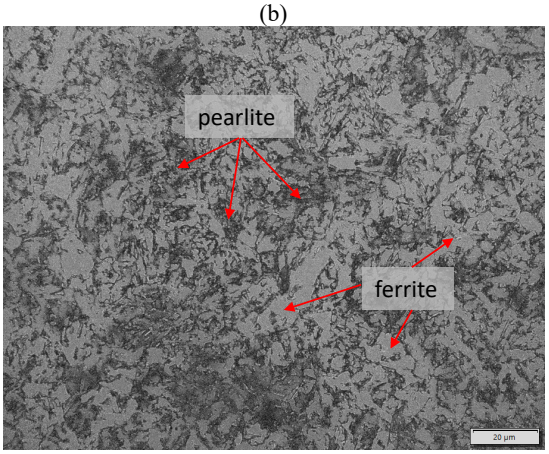

(c)

Figure 3. Microstructure of A588 steel with a composition of 0.42% Ni after quench-temper process with cooling media of (a) water, (b) oil, and (c) open air. Etching with Picral solution

The tempered martensite, which consists of recrystallization ferrite (equiaxed α phase) and cementite phase, is formed as a result of single-phase martensite (BCT-body centered tetragonal) saturated with carbon undergoing a reaction due to low energy activation for diffusion during reheating process [16]-[17]. As a result of the tempered martensite formation, the mechanical properties are not as hard as martensite but more

ductile than martensite [17]. As tempered at 400 °C, the ferrite increases due to the reduction in the martensite phase and facilitates the fine pearlite precipitation. Quench media is closely related to cooling rate and residual stresses formed due to carbon supersaturated solute atoms during cooling [18]. The water and oil quenchant leads to rising in cooling rate more than air cooling and accelerates the austenite decomposition into martensite form (tetragonal structure) with diffusion-less transformation. But, slow cooling within the materials leads to the laminar phases of pearlite, bainite, and ferrite [19]. In lower C concentration (0.17 wt.%C), tempering 400 °C will improve the ductility and young modulus due to the different shear modulus of tempered martensite, which simultaneously leads to generating the prevalent unstable martensite structure, ferrite, cementite, and a carbide precipitate, which associated with the change in lattice distortion (BCT to BCC-body centered cubic lattice).

However, as the carbide particle expands during the dislocation process under tensile force, the shearing stress rises as well [20]. Oil-tempered martensite has a different form than water-cooled tempered martensite. It is because the cooling rate of oil is slightly slower than that of water. As a result, this affects the transformation time of austenite into martensite so that the resulting martensite becomes larger and tends to form blocks. Like the water quenched, austenite does not have enough time to transform into the ferrite phase. As a result, the final martensite is smaller than the martensite with oil cooling [7]. The tempered martensite was not visible (Fig. 3(c)) on decreasing the cooling rate of heat treatment i.e., with open-air cooling. The tempering process does not alter the microstructure of ferrite and pearlite.

Figure 4 shows the nickel content effect on the microstructure of A588 steel. In general, the microstructure consisted of tempered martensite (bainite form or needle-like structure in the black part), ferrite, and pearlite. As increasing the nickel, the grain size increased and the irregular block of bainite was observed (Figs. 4(c)-4(d)) [15]. With the increase of nickel level, the coarse austenite was more likely formed and provided a driving force for the bainite growth. Therefore, there is a large amount of bainite in the sample with 3% Ni [15],[21].

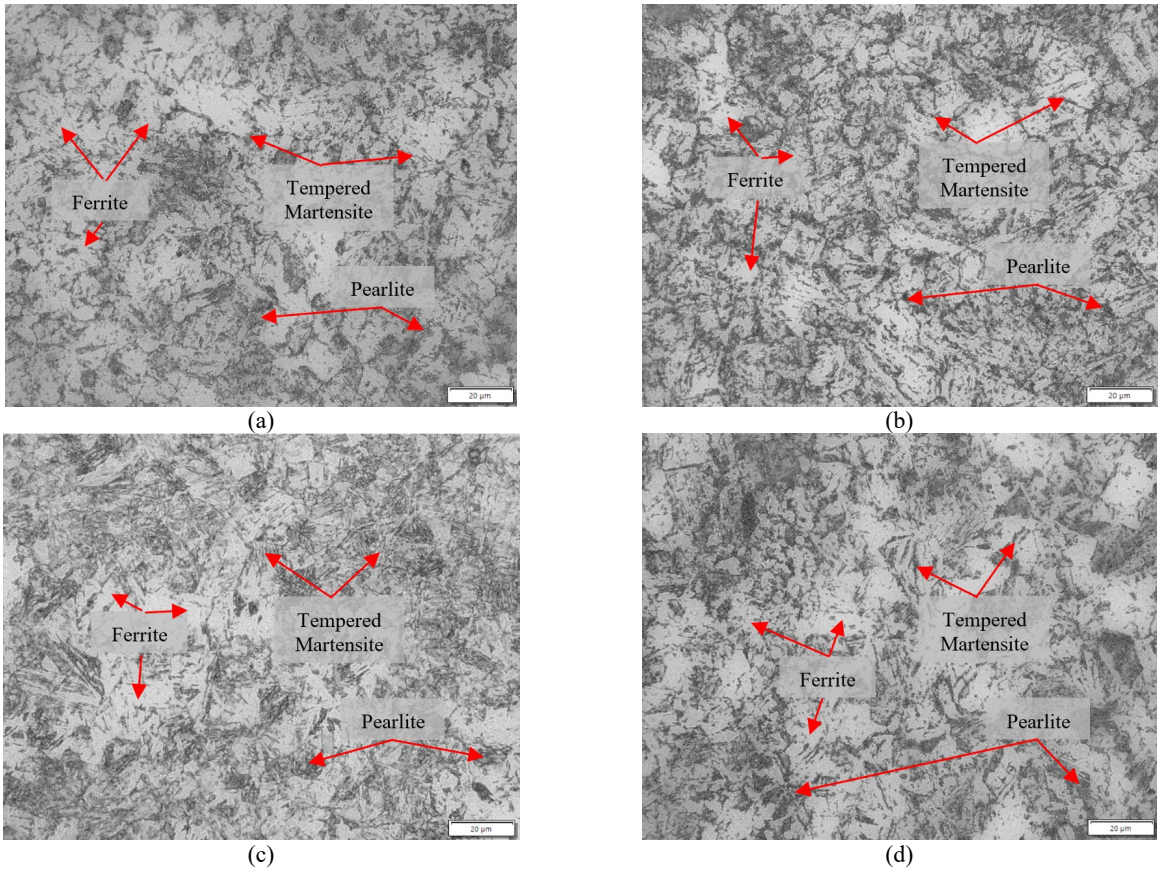

Figure 4. The effect of nickel level of (a) 0.41%, (b) 1%, (c) 2%, and 3% after water quench and followed by tempering at 400 °C. Etching with Picral solution

The bainite structure is formed as a result of austenite transformation during water quench (according to Fig. 2) while martensite is transformed to tempered martensite (mixture of ferrite+cementite) during tempering at 400 °C.

3.2 Mechanical Properties

The mechanical properties of A588 with nickel addition in varying quench was successfully represented by tensile and hardness test. The tensile result is shown in Fig. 5, and the hardness result is shown in Fig. 6.

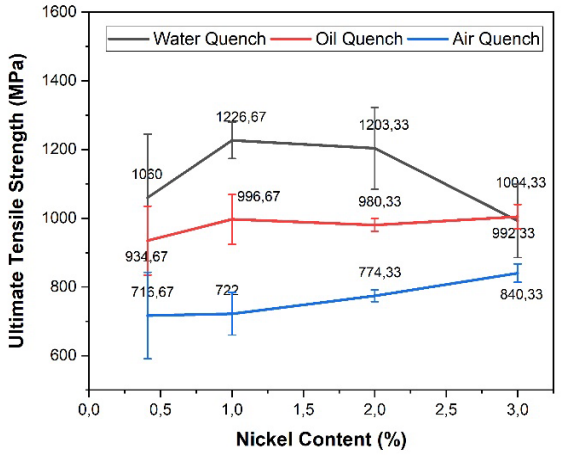

(a)

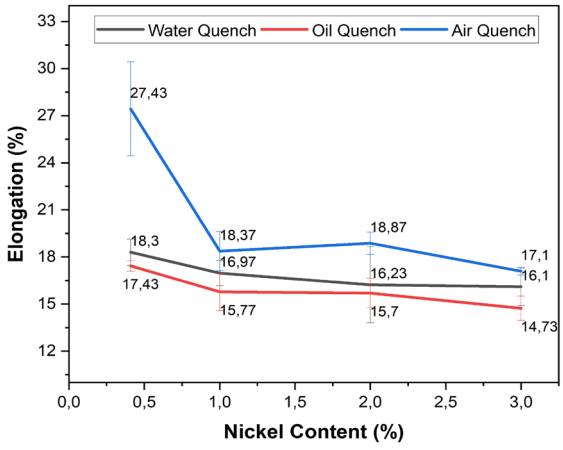

(b)

Figure 5. Effect of nickel and quenchant medium on (a) ultimate tensile strength and (b) elongation of A588 steel

Based on Figure 5, the cooling medium significantly affects the strength value in A588, while the nickel addition is slightly affected. The fast cooling, i.e. water quench, produces the highest strength value compared to other cooling media, is 1060 Mpa for 0.41% Ni, 1226.67 for 1% Ni, 1203.33 MPa for 2% Ni, and 1004.33 MPa for 3% Ni. The strength increases considerably with the cooling rate during quenching. By reducing the martensite transformation temperature and producing enormous martensite (high volume phase), nickel is a common austenite stabilizer which subsequently increases strength in an indirect manner [22]. Also, UTS can be strengthened using a substitusional solid solution. This result follows the simulation using JMAtPro software that the faster the cooling rate, the less perfect the sample will diffuse and resulting in the presence of a martensite phase [16].

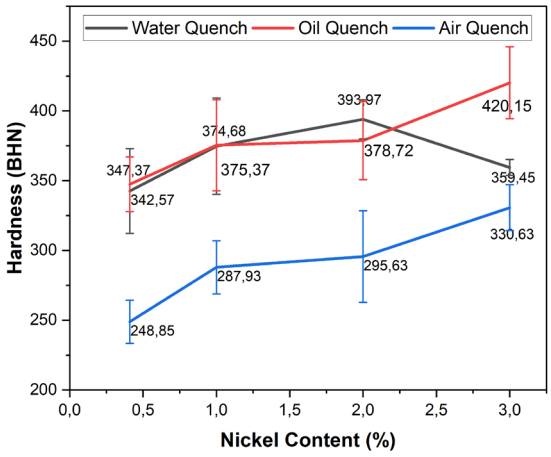

Figure 6. Effect nickel and quenchant medium on hardness of A588 steel

In opposition, the excessive nickel could also increase the stability of retained austenite, increase carbon's activity coefficient, and further decrease strength [23]. With fast cooling, the nickel addition improves the strength to 1226.67 MPa for water quenched and 996.67 MPa for oil quenched.

In addition, the rule of ductility is inversely proportional to the value of tensile strength. As increase the cooling rate, the elongation decreases. The air-quenched sample had the highest elongation the other, which is 17.1–27.43%. Air-quench allows the austenite phase to diffuse more entirely to have a more ductile phase and form a ferrite-pearlite phase. The tempered martensite did not carry excellent strength and microhardness, but its plasticity and toughness are relatively better [16].

In low alloy, the tempering process induces the decomposition of tempered martensite, static recovery of dislocation, and residual stress released. The ductility after quenching is close to the air cooling value. Besides that, the nickel addition causes a slight decrease in the ductility value due to the high fraction of martensite.

In Figure 6, the water and oil quenched samples had a similar hardness of above 340 BHN, and the air-quenched sample had a lower hardness of 240-330 BHN. The hardness results have a similar pattern to the strength value. During the 400 °C tempering process, the diffusion kinetics of atoms is feasible, which results in a moderate rate of softening effect [18].

DOI : 10.14203/metalurgi.v37i3.630

Metalurgi is Sinta 2 Journal (https://sinta.ristekbrin.go.id/journals/detail?id=3708) accredited by Ministry of Research & Technology, Republic Indonesia

The results obtained for tensile and hardness are subjected to statistical analysis using the ANOVA (analysis of variance) - two ways factor with a 5% significance level.

Table 3. Result of ANOVA-two way for strength

	DF	Sum of Squares	Mean Square	F Value	P Value
Nickel Addition	3	13160.84	4386.95	0.694	0.588
Cooling Medium	2	258914.02	129457.01	20.486	0.002
Error	6	37916.13	6319.35		
Total	11	309990.99			

The F-critical is 4.757 for nickel addition and 5.143 for the cooling medium factor. If the F-value < F-critical, the nickel addition or cooling medium aspect is not affected. On the contrary, if the F-value > F-critical, the nickel addition or cooling medium significantly affects the properties.

Table 4. Result of ANOVA-two way for elongation

	DF	Sum of Squares	Mean Square	F Value	P Value
Nickel Addition	3	45.74	15.25	3.278	0.101
Cooling Medium	2	45.44	22.72	4.884	0.055
Error	6	27.91	4.65		
Total	11	119.09			

The ANOVA results in Table 3-5 show that the nickel addition does not significantly affect the strength, but the cooling medium factor is worked substantially on. It is indicated that the microstructure differences after the quench-temper have to involve the strength value considerably, while the grain size does not. In addition, elongation is not significantly affected by cooling media and nickel addition.

Table 5. Result of ANOVA-two way for hardness

	DF	Sum of Squares	Mean Square	F Value	P Value
Nickel Addition	3	5325.98	1775.33	4.864	0.048
Cooling Medium	2	18815.03	9407.51	25.774	0.001
Error	6	2189.97	364.99		
Total	11	26330.98			

The ductility value of the oil-water quench sample is almost equivalent to that of air cooling. The hardness is greatly influenced by cooling and nickel level differences.

3.3 Corrosion Properties in 3.5% NaCl

The corrosion behavior of steel mainly depends on chemical composition and microstructure. The corrosion of tempered A588 steel in 3.5 wt% NaCl solution was examined

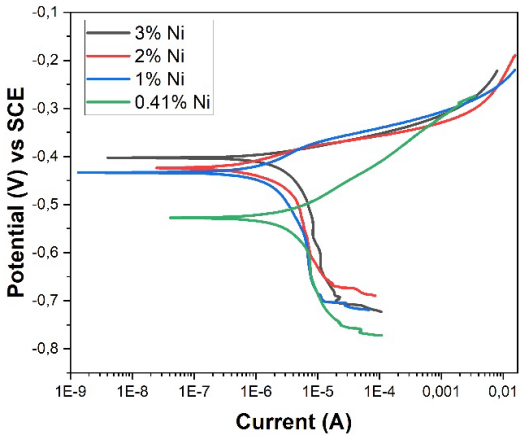

(a)

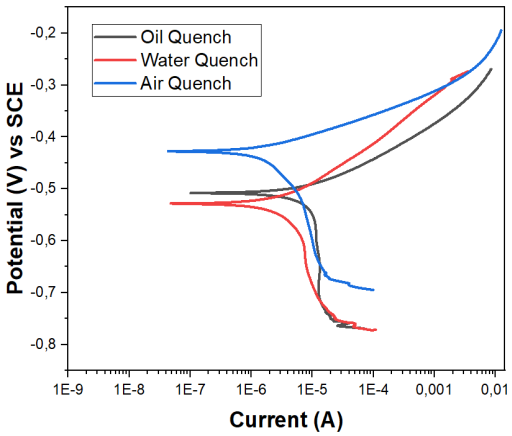

(b)

Figure 7. Effect of (a) nickel addition and (b) cooling media on the polarization curve of A588 steel

using the Tafel extrapolation technique, shown in Fig 7. The electrochemical parameter obtained from the extrapolation of anodic and cathodic Tafel fit lines are listed at Table 6.

From Figure 7(a), the nickel addition in tempered A588 steel shifted the curve upward and remarkably changed the corrosion potential (*Ecorr*) – current corrosion (*Icorr*).

Table 6. The fitted value of the polarization paramater of A588

	Beta ($x10^{-3}$ V/dec)	Ecorr (mV)	Icorr ($\mu A/cm^2$)	Corrosion Rate (mpy)
0.41% Ni - Water quench	533.8	-528.0	5.343	2.879
1% Ni - water quench	618.7	-471.8	4.940	2.697
2% Ni - water quench	481.7	-424.6	3.336	1.944
3% Ni - water quench	26.26	-432,5	0.12	0.072
0.41% Ni - Oil quench	58.19	-508.9	7.728	4.504
0.41% Ni - Air Quench	38.13	-427.6	1.443	0.841

The corrosion current density (*Icorr*) decreased from 5.343 μA/cm^2 to 0.12 μA/cm^2 with the nickel addition of up to 3%. With the increase of nickel level, the mixed-corrosion potential tends to be more positive, and further, the corrosion rate became slower. The less positive potential probably indicates the higher ability of 3%Ni in developing a thicker layer of corrosion product compared to 0.41% Ni [24]. Besides that, the grain size of the bainite phase (Figs. 4(a)-4(d)) also works on the corrosion rate. The more refined martensite structure could improve corrosion resistance [25].

The cooling medium influences the polarization curve shifting according to Fig. 7(b). As the cooling rate increase, the curve moves downward and Icorr becomes more negative. It indicates that the corrosion rate increases from 0.841 to 4.504 mpy as the cooling rate accelerates. The pearlite was preferably corroded, and the lamellar Fe_3C inside the pearlite/bainite structure could push forward the Fe^{2+} dissolution because the pearlite's zero current potential is more negative than ferrite. After the pearlite phase was totally corroded, the corrosion entered the ferrite phase from the ferrite/pearlite phase boundary. It was noticed that the multiphase formed a micro-galvanic between martensite island with bainite-ferrite couple corrosion and advanced the higher corrosion [25]. Compared with bainite and martensite, pearlite has better corrosion resistance.

The difference in volume fraction of each phase in the oil and water quenched sample causes differences in the corrosion rate. Tempered martensite of volume fraction plays a vital role in the corrosion mechanism, and the martensite phase is less noble than the bainite phase. The corrosion is preferred to occur at the interface and the lath of tempered martensite with high grain boundary [26]-[27]. The oil-quenched sample has a higher martensite volume fraction (Fig. 3(a)-3(b)), so the corrosion is more aggressive than a water-quench sample.

4. CONCLUSION

The combined effects of nickel addition and the quench-temper method on the mechanical and corrosion properties of A-588 steel were examined in this study. Nickel is a typical austenite stabilizer that indirectly boosts strength by lowering the martensite transformation temperature and creating large martensite. Bainite's and martensite's temperature is often lowered when nickel is added up to 3%, to 355 for Ms and 523 for Bs, respectively. Due to the out-diffusion of carbon, the ferrite fraction increases as the temperature is tempered to 400 by rapid cooling (water and oil quenchant). Its favors the formation of fine cementite (tempered martensite). The air quench-temper method was used to create the ferrite-pearlite structure. The tensile strength value and the ductility rule have an inverse relationship. The water quench prepared the strongest specimens, and its strength increases with the addition of 1% nickel (1226.67 MPa), but it drops to 1004.33 MPa when an excess of 3% nickel is applied due to the increased retained austenite. The elongation (%) decreased as the cooling rate increased, typically 17.43-14.73 for oil quench, 18.3-16.1 for water quench, and 27.43-17.1 for open-air cooling. The addition of nickel had no impact on the strength and elongation, according to the results of the ANOVA statistical test; however, the change of the cooling medium significantly impacted the tensile properties (P values 0.588 and 0.101). The hardness of the water- and oil-quenched samples were both above 340 BHN, while the hardness of the air-quenched sample was between 240 and 330 BHN. Both factors have a significant impact on hardness.

ACKNOWLEDGMENT

The authors acknowledge the facilities, scientific, and technical support from Research Center for Metallurgy, National Research and Innovation Agency.

REFERENCES

[1] J. Jia, Z. Liu, X. Cheng, C. Du, and X. Li, "Development and optimization of Ni-advanced weathering steel: A review," *Corros. Commun.*, vol. 2, pp. 82-90, 2021. Doi: 10.1016/j.corcom.2021.09.003.

[2] M. Morcillo, I. Díaz, H. Cano, B. Chico, and D. de la Fuente, "Atmospheric corrosion of weathering steels. Overview for engineers. Part I: Basic concepts," *Constr. Build. Mater.*, vol. 213, pp. 723-737, 2019. Doi: 10.1016/j.conbuildmat.2019.03.334.

[3] X. Cheng, Z. Jin, M. Liu, and X. Li, "Optimizing the nickel content in weathering steels to enhance their corrosion resistance in acidic atmospheres," *Corros. Sci.*, vol. 115, pp. 135-142, 2017. Doi: 10.1016/j.corsci.2016.11.016.

[4] S. . Tukur, M. M. Usman, I. Muhammad, and N. A. Sulaiman, "Effect of tempering temperature on mechanical properties of medium carbon steel," *Int. J. Eng. Trends Technol.*, vol. 9, no. 15, pp. 798-800,

2014. Doi: 10.14445/22315381/ijett-v9p350.

[5] Y. K. Bao, M. Wu, K. X. Liu, Y. Y. Feng, and X. M. Zhao, "Effect of tempering temperature on carbide precipitation and mechanical properties of marine atmospheric corrosion resistant steel," *J. Mater. Eng. Perform.*, vol. 31, pp. 2517-2524, 2022. Doi: 10.1007/s11665-021-06335-6.

[6] D. Ning, C.R. Dai, J. L Wu, Y.D Wang, Y.Q Wang, Y. Jing, and J. Sun., "Carbide precipitation and coarsening kinetics in low carbon and low alloy steel during quenching and subsequently tempering," *Mater. Charact.*, vol. 176, pp. 111111, 2021. Doi: 10.1016/j.matchar.2021.111111.

[7] M. Rohmah, D. Irawan, D. P. Utama, and T. B. Romijarso, "Pengembangan baja laterit modifikasi A588 menggunakan proses termomekanikal diikuti dengan proses temper temperatur rendah untuk aplikasi baja tahan cuaca," *TEKNIK*, vol. 42, no. 2, pp. 149-159, 2021. Doi: 10.14710/teknik.

[8] C. Zhu, X. Y. Xiong, A. Cerezo, R. Hardwicke, G. Krauss, and G. D. W. Smith, "Three-dimensional atom probe characterization of alloy element partitioning in cementite during tempering of alloy steel," *Ultramicroscopy*, vol. 107, no. 9, pp. 808-812, 2007. Doi: 10.1016/j.ultramic.2007.02.033.

[9] Ş. H. Atapek, Ş. Polat, and S. Zor, "Effect of tempering temperature and microstructure on the corrosion behavior of a tempered steel," *Prot. Met. Phys. Chem. Surfaces*, vol. 49, no. 2, pp. 240-246, 2013. Doi: 10.1134/S2070205113020111.

[10] A. Kalhor, M. Soleimani, H. Mirzadeh, and V. Uthaisangsuk, "A review of recent progress in mechanical and corrosion properties of dual phase steels," *Arch. Civ. Mech. Eng.*, vol. 20, no. 3, pp. 1-14, 2020. Doi: 10.1007/s43452-020-00088-0.

[11] Y. K. Lee, "Empirical formula of isothermal bainite start temperature of steels," *J. Mater. Sci. Lett.*, vol. 21, no. 16, pp. 1253-1255, 2002. Doi: 10.1023/A:1016555119230.

[12] J. Platl, H. Leitner, C. Turk, and R. Schnitzer, "Determination of martensite start temperature of high-speed steels based on thermodynamic calculations," *Steel Res. Int.*, vol. 91, no. 8, 2020. Doi: 10.1002/srin.202000063.

[13] H. Martin, P. A. Yirenkyi, A. Pohjonen, N. K. Frempong, J. Komi, and M. Somani, "Statistical modeling for prediction of CCT diagrams of steels involving interaction of alloying elements," *Metall. Mater. Trans. B Process Metall. Mater. Process. Sci.*, vol. 52, no. 1, pp. 223-235, 2021. Doi: 10.1007/s11663-020-01991-w.

[14] R. Neugebauer, A. Rautenstrauch, and E. Meza-García, "Influence of the alloying elements on phase transitions of high strength steels," *Adv. Mater. Res.*, vol. 337, pp. 358-362, 2011. Doi: 10.4028/www.scientific.net/AMR.337.358.

[15] H. Y. Dong, C. Y. Hu, G. H. Wu, K. M. Wu, and R. D. K. Misra, "An effect of nickel on hardening behavior and mechanical properties of nanostructured bainite-austenite steels," *Mater. Sci. Eng.*, vol. 817, pp. 141410, 2021. Doi: 10.1016/j.msea.2021.141410.

[16] Z. Yao, W. Dai, B. Cai, C. Li, H. Zhang, and Y. Zhang, "Effect of quenching temperature on tensile strength and fatigue behavior of an EA4T steel," *J. Mater. Eng. Perform.*, vol. 30, no. 12, pp. 9015-9028, 2021. Doi: 10.1007/s11665-021-06117-0.

[17] H. Jo, M. Kang, G. Park, B. Kim, C. Y. Choi, H. S. Park, S. Shin, W. Lee, Y. Ahn, and J. B. Jeon., "Effects of cooling rate during quenching and tempering conditions on microstructures and mechanical properties of carbon steel flange," *Materials (Basel)*, vol. 13, no. 18, pp. 1-16, 2020. Doi: 10.3390/MA13184186.

[18] B. Laxmi, S. Sharma, J. PK, and A. Hegde, "Quenchant oil viscosity and tempering temperature effect on mechanical properties of 42CrMo4 steel," *J. Mater. Res. Technol.*, vol. 16, pp. 581-587, 2022. Doi: 10.1016/j.jmrt.2021.11.152.

[19] P. Singh and S. Singh, "Effect of quenching media on microstructural evolution, mechanical and wear properties of AISI4135 steel," *Proc. Inst. Mech. Eng. Part C J. Mech. Eng. Sci.*, vol. 235, no. 21, pp. 5616-5625, 2021. Doi: 10.1177/0954406221990050.

[20] C. Baron, H. Werner, and H. Springer, "On the effect of carbon content and tempering on mechanical properties and stiffness of martensitic Fe–18.8Cr–1.8B–

xC high modulus steels," *Mater. Sci. Eng. A*, vol. 809, 2020, pp. 141000, 2021. Doi: 10.1016/j.msea.2021.141000.
[21] M. Grade and L. Carbon, "The effect of nickel contents on the microstructure evolution deposited metal," *Crystals*, vol. 11, no. 709, pp. 1-16, 2021.
[22] J. Wang, X. Di, C. Li, and D. Wang, "The influence of ni on bainite/martensite transformation and mechanical properties of deposited metals obtained from metal-cored wire," *Metals (Basel).*, vol. 11, no. 12, 2021. Doi: 10.3390/met11121971.
[23] C. G. Norwood, "The effect of nickel content on the mechanical properties and microstructure of a high toughness secondary hardening steel," Carnegie Mellon University, pp. 45, 2016.
[24] N. Alharthi, E. S. M. Sherif, H. S. Abdo, and S. Z. El Abedin, "Effect of nickel content on the corrosion resistance of iron-nickel alloys in concentrated hydrochloric acid pickling solutions," *Adv. Mater. Sci. Eng.*, vol. 2017, article no. 1893672, 2017. Doi: 10.1155/2017/1893672.
[25] Z. Li, W. Xue, Y. Chen, W. Yu, and K. Xiao, "Microstructure and grain boundary corrosion mechanism of pearlitic material," *J. Mater. Eng. Perform.*, vol. 31, no. 1, pp. 483-494, 2022. Doi: 10.1007/s11665-021-06171-8.
[26] D. Zhang, X. Gao, G. Su, Z. Liu, N. Yang, L. Du, and R. D. K. Misra, "Effect of tempered martensite and ferrite/bainite on corrosion behavior of low alloy steel used for flexible pipe exposed to high-temperature brine environment," *J. Mater. Eng. Perform.*, vol. 27, no. 9, pp. 4911-4920, 2018. Doi: 10.1007/s11665-018-3587-0.
[27] I. Bösing, I. Bobrov, J. Epp, M. Baune, and J. Thöming, "Influence of systematically changed martensite content on the passive film properties of austenitic stainless steel in neutral electrolyte," *Int. J. Electrochem. Sci.*, vol. 15, no. 1, pp. 319-333, 2020. Doi: 10.20964/2020.01.09.

Metalurgi (2022) 3: 97 - 104

METALURGI
Majalah Ilmu dan Teknologi
p-ISSN 0126-3188 | e-ISSN 2443-3926
ejurnalmaterialmetalurgi.lipi.go.id

ANODIZING-ELECTRODEPOSITION HYBRID COATING BY USING SYNTHESIZED NATRIUM SILICATE AND ZIRCONIUM OXIDE ON THE SURFACE MAGNESIUM AZ31B

Aprilia Erryani[a], Bunga Rani Elvira[a], Syifa Ranggayoni Nurbaiti[b], Amalia Syahiddah[b], Hafsah Mujahidah[b], Yudi NugrahaThaha[a], Esmar Budi[b]

[a]Research Center for Metallurgy, National Research and Innovation Agency
Management Building 720, B.J. Habibie Sains and Technology Area, Banten, Indonesia 15314
[b]Fisika, Universitas Negeri Jakarta
Jl. R. Mangun Muka Raya No.11, Jakarta Timur, Indonesia
*E-mail: apri005@brin.go.id

Received: 02-10-2022, Revised: 08-11-2022, Accepted: 31-12-2022

Abstract

In this study, sodium silicate was synthesized, and zirconia was characterized as a suspension solution for anodization and electrodeposition processes. The results of the FTIR (fourier transform infrared) synthesis demonstrated the success of producing Na_2SiO_3 with the appearance of absorption from functional groups such as silanol (Si-OH) and siloxane (Si-O-Si) According to the SEM (scanning electron microscope) data, each batch contains oxygen, sodium, and silicon, indicating that Na_2SiO_3 was successfully synthesized without any detectable impurities. SEM images revealed that the calcination of $ZrOCl_2.8H_2O$ was dominated by zircon elements, with batch 3 having the highest zircon content at 88.81%. The XRD (x-ray diffraction) results show that ZrO_2 (monoclinic) dominates, with Cl_2 present in batches 1 and 3. As a result, the ZrO_2 used without calcination is in batch 3. Anodizing and electrodeposition processes can be performed in three ways: a. anodizing, b. two steps (anodizing-electrodeposition), and c. one step hybrid (anodizing and electrodeposition) with the addition of Al_2O_3 and $Na_2O_7SiO_3$ elements to the electrolyte. After coating, the surface of magnesium appears to be a pale white line. SEM images revealed that all three methods are coated and contain elements such as O, Na, Mg, Zr, Si, K, and Al in method c. The three samples also revealed that the sanding process was not optimal and that the Zr particles on the surface were not evenly distributed.

Keywords: *Anodizing, electrodeposition, ZrO_2, sodium silicate, magnesium*

1. INTRODUCTION

Biomaterials are materials that have direct contact with biological systems in living things, these materials are required to have several requirements, including not causing adverse effects on the body, having corrosion resistance, and having good strength [1]. In their application, biomaterials are used to replace or restore the function of bone components that have failed or been damaged. [2]. Several biomedical components such as artificial joints, implants, and drug delivery systems require the use of materials with biocompatible and biodegradable properties, thus requiring the development of new biomaterials that can be used for these applications [3]-[4]. In recent years, all attention has focused on biodegradable materials that serve to provide temporary support for fractures and will dissolve in the human body without harming their health [5].

Implants are a type of biomaterial used to replace bone tissue that has been damaged or is no longer functional as a result of disease or accident [6]. The term biodegradable on implants refers to the material's ability to corrode or degrade in the human body [7].

At present, magnesium metal (Mg) and its alloys are of concern because they are the right materials for implant applications that can be degraded in the body gradually, beneficial in

DOI : 10.14203/metalurgi.v37i3.680

Metalurgi is Sinta 2 Journal (https://sinta.ristekbrin.go.id/journals/detail?id=3708) accredited by Ministry of Research & Technology, Republic Indonesia

their absorption, if excessive levels can be excreted (excreted) through urine [8]-[11]. The release of Mg^{2+} ions into the body can help the growth of bone tissue and speed up healing time. Mg has good biocompatibility, low density, high specific strength, and a modulus of elasticity that is almost the same as a bone so that it can avoid stress shielding on bone [12]-[13].

Magnesium is the lightest metal that can be degraded through corrosion that occurs in body fluids [9]. However, its high solubility is also a weakness for magnesium, which can corrode rapidly in physiological pH (7.4-7.6) and high chloride physiological environment, so mechanical properties decrease before healing and new tissue growth [14]-[16].

Proper surface treatment can increase the wear and corrosion resistance of the substrate [17]. There are several surface treatment techniques developed to protect magnesium and its alloys. These techniques include chemical conversion coating, electrodeposition, anodizing, gas-phase deposition, organic coating, and sol-gel techniques [18].

The coating methods used in this research are anodizing and electrodeposition (electrodeposition). Anodizing can produce a passive film on the magnesium surface. The passive layer formed can reduce the corrosion rate of magnesium [19]. This method is very simple compared to other methods, so it reduced processing time. The coating results have a strong adhesion between the coating and the substrate, so it is good at controlling the corrosion rate of magnesium. [20].

In the electrodeposition process, charged particles or polymer macromolecules in suspension will move toward the electrode under the influence of an electric field [21]. The quality of the coating is determined by the length of time and the stress of the coating used. The longer the coating time, the thickness of the layer formed will increase [22]-[23].

An electrolyte solution containing a mixture of chemical compounds is required to carry out the anodizing and electrodeposition processes. The chemical compound $ZrOCl_2.8H_2O$ was calcined and silica was synthesized in this study. Zirconia can improve osteointegration and inhibit bacterial growth on the implant surface [24]. The calcination and synthesis processes were repeated three times in this study to determine suitable variables in the anodizing and electrodeposition processes. This research can prove that the synthesis of Na_2SiO_3 and the calcination of ZrO_2 can be used as a coating on magnesium through anodizing and electrodeposition processes. As a result, the purpose of this study was to investigate the effect of chemical compounds in suspension solution on magnesium coating using the electrodeposition method. The electrolyte solution and ZrO_2 electrodeposition coating process is expected to reduce corrosion while inhibiting the formation of a bacterial layer on the implant surface.

2. MATERIALS AND METHODS

2.1 Material Preparation

Magnesium AZ31B is the material used in this study. The following step is to make Na_2SiO_3 by dissolving 16 gr of NaOH in 100 ml of distilled water. A hotplate at 100 °C was used to heat 82.5 ml of the solution with 10 g of silica until crystals formed. Table 1 shows that the synthesis was performed three different times. Following that, all samples were heated for 30 minutes in a 500 °C furnace.

Table 1. Time in the synthesis process

Sample	Time (minute)
Bacth 1	120
Bacth 2	40
Bacth 3	25

Three experiments conditions for zircon calcination were carried out, as shown in Table 2.

Table 2. Content in the calcination zircon

Sample	Zircon (g)	Citric Acid (g)
Batch 1	3	1
Bacth 2	3	0.5
Bacth 3	3	0

To form a sol-gel, all materials were dissolved in 50 ml of distilled water in batches 1 and 2. After all the samples were ready, they were heated for 90 minutes in a muffle furnace at 200 °C and then for 3 hours in a muffle furnace at 700 °C.

Table 3. Suspended electrolytic for batch 1

Process	Contents
Anodizing	20 g Na_2SiO_3 3 g ZrO_2 7 g NaOH 7 g KF 7 g NaF

Following the calcination and synthesis processes, the results can be used as an electrolyte solution. To begin anodizing and electrodeposition, a suspended electrolyte is prepared.

Table 4. Suspended electrolytic for batch 2

Process	Contents
Anodizing	20 g Na_2SiO_3
	3 g ZrO_2
	7 g NaOH
	7 g KF
	7 g NaF
Electrodeposition	0.5 g Al_2O_3
	0,2 g Na_2HPO_4

The materials used to make the electrolyte solution are listed in Tables 3, 4, and 5. For both processes, all ingredients are dissolved in 500 mL of distilled water.

Table 5. Suspended electrolytic for batch 3

Process	Contents
Anodizing	20 g Na_2SiO_3
	3 g ZrO_2
	7 g NaOH
	7 g KF
	7 g NaF
Electrodeposition	0.5 g Al_2O_3
	0,25 g Na_2HPO_4
	0.5 g $Na_2O_7SO_3$

The anodization and electrodeposition process begins with two platinum anodes facing each other and a magnesium cathode. The three experiments were completed in 30 minutes using a rectifier.

2.1 SEM (Scanning Electron Microscope)

The surface topography and structural defects of the composite structure are examined using a SEM (scanning electron microscope). The SEM is a JEOL JSM6390A model. To determine the distribution of ZrO_2 in composites, SEM is supplemented by EDS (energy dispersive spectroscopy). Before testing, composite samples were coated with suspension.

2.2 FTIR (Fourier Transform Infrared)

The infrared absorption or emission spectra of solid, liquid, or gaseous substances can be obtained using the FTIR (fourier transform infrared) technique. FTIR's basic operation is to identify compounds, detect functional groups, and analyze desired mixtures and samples. In general, FTIR is frequently used to quantitatively and qualitatively identify organic compounds. FTIR is used in quantitative research to determine the concentration of analytes in a sample. FTIR was performed by Bruker in the wavenumber range 4000-350 cm^{-1} to identify the presence of functional groups on the sample with spectra resolution of 4 cm^{-1}, 45 scans, and Blackman-Harris 3-Term apodization.

2.3 XRD (X-Ray Diffraction)

XRD (x-ray diffraction) is used for material characterization and quality control of crystalline or non-crystalline materials such as powders, solid blocks, thin films or liquids. XRD is also used to determine composition and determine elements. From the XRD results it will be known which structure is formed. The working principle of the XRD tool is to use x-ray crystals which will then appear in a material to see the structure of the material. XRD test was performed by Smartlab Rigaku, carried out at 2θ from 20° to 90°. XRD measurements were operated at 15 mA and 40 kV using Cu Kα radiation.

3. RESULT AND DISCUSSION

3.1 Analysis Results SEM of Synthesis Na_2SiO_3

The synthesis of Na_2SiO_3 from SiO_2 can be seen from the SEM (scanning electron microscope) and EDS (energy dispersive spectrometry) images. The difference in heating time in the sol-gel process did not significantly affect the composition of Na_2SiO_3. The difference is seen in the shape of the crystals.

In batch 1 (Fig. 1(a)) the crystal form is the most lumpy and coarser. This is caused by unstable heating, making the process take a long time. In batch 2 (Fig. 2(b)), the crystal form is relatively finer than batch 1, however, the surface looks more porous than batch 2. In batch 3 (Fig. 3(c)), the crystal form is relatively cleaner and smoother than the two previous batches. This is because the heating is done at the right time and gets a good texture. The test results in all batches showed the detected water content. That's because, the nature of Na_2SiO_3 which is hygroscopic.

The results of qualitative analysis using EDS (Table 6) showed that pure sodium silicate was successfully synthesized in this experiment. This is indicated by the absence of impurities in the form of C or carbon atoms and impurity metals in all batches. It also shows that the length of time and temperature in the heating process did not affect the success of the synthesis. But it affects the shape of the synthesized crystal. When NaOH melts at high temperatures, it completely

dissociates to form Na+ ions and OH- ions. The high electronegativity of the O atom in SiO2 makes more Si electropositive, resulting in the formation of an unstable $[SiO_2OH]^-$ intermediate and dehydrogenation.

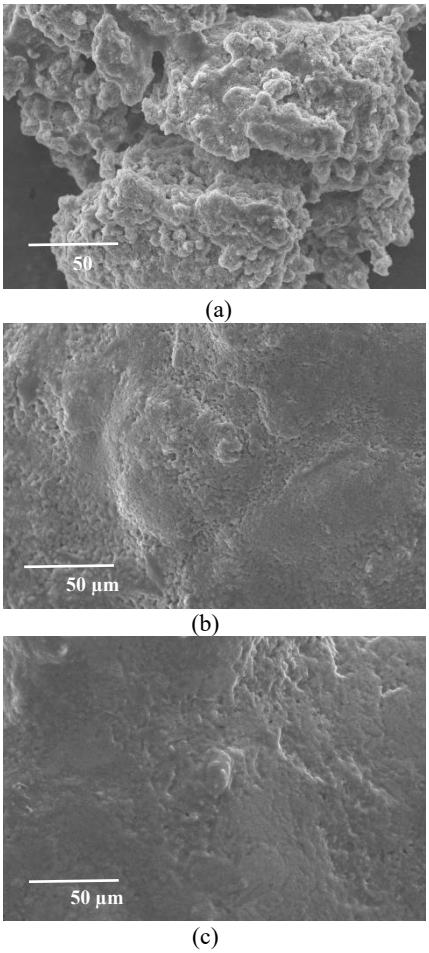

Figure 1. SEM images of Na_2SiO_3 synthesis at (a) Batch 1, (b) Batch 2, and (c) Batch 3

Melting at 500 °C is based on the melting point of NaOH, which is 318 °C, at which point NaOH completely dissociates to form Na^+ and OH^- ions. NaOH was chosen because it has a lower melting point than Na_2SiO_3 around 851 °C, allowing for the formation of sodium silicate at lower temperatures [25].

Tabel 6. EDS of synthesized Na_2SiO_3

		Batch 1	Batch 2	Batch 3
Element		Mass%	Mass%	Mass%
O	K	51.8177	50.6603	58.1238
Na	K	33.6874	36.8691	29.7613
Si	K	14.4949	12.4506	12.1149

The second OH^- ion will form a water molecule by bonding with hydrogen, and two Na^+ ions will balance the negative charge of SiO_3^{2-} ions to form sodium silicate [26].

The EDS data obtained revealed differences in the content of each sample, with batch 1 containing 37.14% O elements, 40.35% Na elements, and 22.50% Si elements. In batch 2, the EDS results contain 38.70% O elements, 44.87% Na elements, and 16.42% Si elements. Batch 3 contains 50.51% element O, 34.69% Na, and 12.79% Si.

3.2 Analysis Results FTIR of Synthesis Na_2SiO_3

The results of the analysis of sodium silicate with FTIR are shown in peaks chart. The results of the FTIR test on 3 batches did not show a significant difference in the wave pattern. The analysis of the FTIR results was carried out by characterizing the wave number range of 500-3500 cm^{-1} to determine the functional group of the main peak.

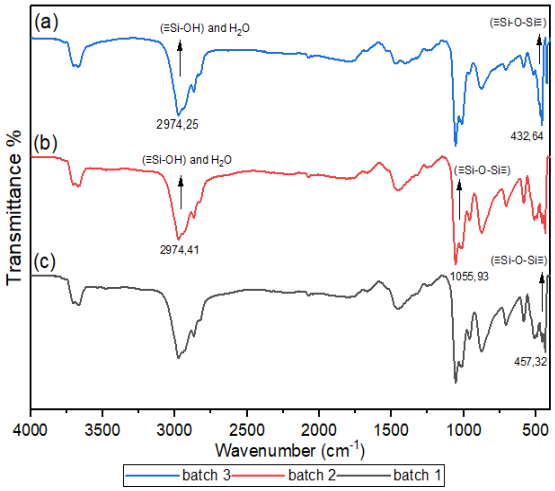

Figure 2. FTIR test results for Na_2SiO_3 synthesis at (a) Batch 3, (b) Batch 2, and (c) Batch 1

Silica absorption patterns that appear generally are silanol (≡Si-OH) and siloxane (≡Si-O-Si≡) groups. The absorption pattern obtained has a pattern that is quite similar to the results of research on the synthesis of Na_2SiO_3 conducted by Linda where the absorption band results obtained at wave numbers 432.64 cm^{-1}, and 457.32 cm^{-1} shows the bending vibration of the siloxane group (≡Si-O-Si≡). The absorption band at wavenumber at 1055.93 cm^{-1} show the Si-O asymmetric stretch vibration of siloxane (≡Si-O-Si≡), and the absorption band at wavenumber at 2974.25 cm^{-1}, and 2974.41 cm^{-1} indicates the -OH group of silanol (≡Si-OH) and H_2O [25].

The FTIR results show that SiO_2 is formed. The reaction that occurs for the formation of SiO2 is as follows:

C, H, and Si + $3O_2 \rightarrow CO_2(g) + 2H_2O(g) + SiO_2(s)$

as well as a condensation of silanol groups (≡Si-OH) such as:

$2 \equiv Si\text{-}OH \equiv Si\text{-}O\text{-}Si \equiv + H_2O$ [27]

Variations in heating time had no effect on the synthesis of Na_2SiO_3. As shown in Fig. 2, the absorption peak of the synthesized Na_2SiO_3 is relatively constant across all time variations.

3.3 Analysis Results SEM of Calcination ZrO_2

Figure 3 shows the SEM (scanning electron microscope) images from ZrO_2 calcination.

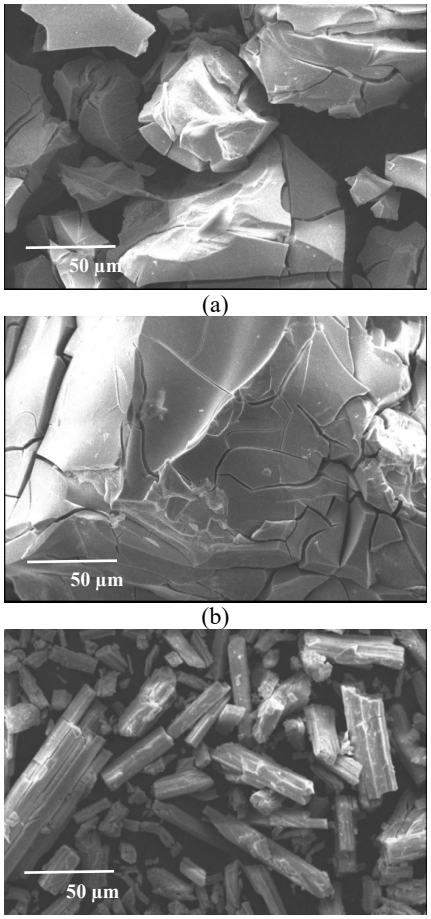

Figure 3. SEM results of ZrO_2 synthesis at (a) Batch 1, (b) Batch 2, and (c) Batch 3

In Figures 3(a) and 3(b), the solid crystal form is almost identical, which is like a lump.

Tabel 7. EDS of synthesized ZrO_2

		Batch 1	Batch 2	Batch 3
Element		Mass%	Mass%	Mass%
O	K	14.3314	56.4202	11.1863
Zr	L	85.6686	43.5798	88.8137

In contrast to Fig. 3(c), where only $ZrOCl_2.8H_2O$ is seen in the form of crystals-like chunks that are longer and scattered. According to the results of the EDS test, there were no impurities in the three batches tested, and the ZrO_2 had been calcined.

The ZrO_2 calcination process from $ZrOCl_2.8H_2O$ was carried out with three different citric acid contents (can be seen in the method). The EDS results (Table 7) for each batch show a different amount of ZrO_2. Batch 2 produces the most oxide of ZrO_2 (56.42%). Batches 1 and 3 were only 14.33% and 11.18%, respectively. According to the EDS results, the optimal amount of citric acid used to produce better calcination of ZrO_2 is 0.5 gram for 3 grams of $ZrOCl_2.8.H_2O$. The EDS results are also supported by XRD data, which will be discussed in the following sub-chapter.

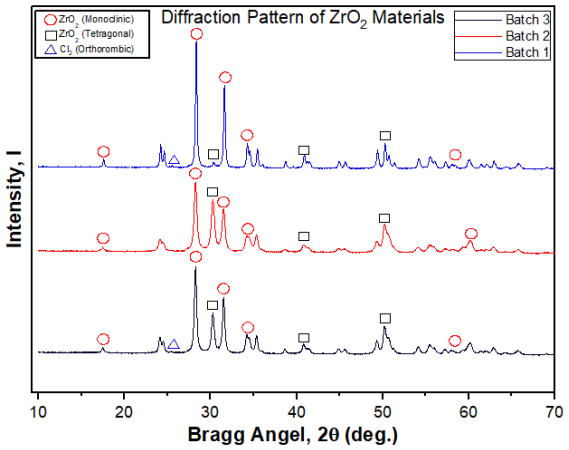

Figure 4. XRD pattern of syntesized ZrO_2

The ZrO_2 phase of the calcination results described previously in SEM images and EDS can be clarified using XRD measurements. Batches 1 and 3 of $ZrOCl_2.xH_2O$ calcination still left Cl_2. The presence of Cl_2 indicates that the calcination results of batches 1 and 3 are still incomplete due to the presence of Cl_2 impurities. There is no Cl_2 impurity in batch 2. Furthermore, ZrO_2 from batch 2 will be used in the Mg coating process.

3.5 Process Anodizing Electrodeposition Analysis Results

The hybrid coating process is accomplished through two methods, the first of which is accomplished in two stages (anodizing followed by electrodeposition). The second method, anodizing-electrodeposition, was carried out concurrently.

Figure 5(a) shows anodized magnesium AZ31B with a porous surface in several places; the striped structure is caused by the grounding process, which is not smooth and flat.

Magnesium AZ31B is well anodized, as shown in Fig. 5(a). The presence of elements O, Na, Mg, and Si was discovered using EDS data.

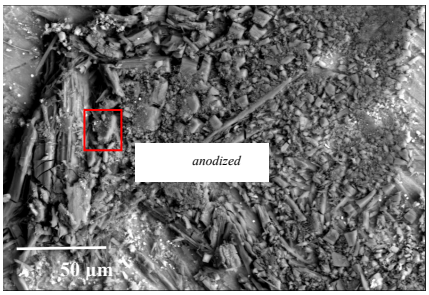

(a)

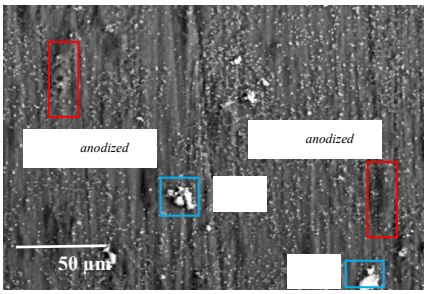

(b)

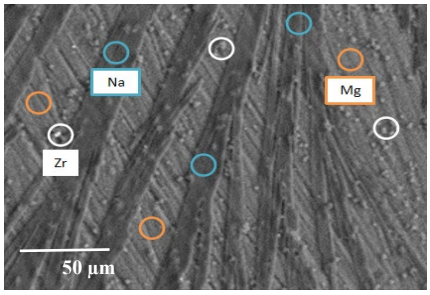

(c)

Figure 5. Photos of SEM results for the following processes; (a) Anodizing (b) Anodizing-electrodeposition in two step (c) Anodizing-electrodeposition hybrid

Following that, a two-stage coating process was carried out in which the surface of Magnesium AZ31B was anodized for 35 minutes to produce a porous structure. After Magnesium AZ31B had dried at room temperature, the process was resumed. The coating process was then continued for 35 minutes using the electrophoretic deposition method with ZrO_2. The dried product appears slightly blackened and pale whitish in color, indicating that it has been coated with Magnesium AZ31B.

Figure 5(b) shows anodized magnesium AZ31B. The ribbed structure is caused by the non-smooth and flat grounding process of Magnesium AZ31B. In several places, the surface is porous. Magnesium AZ31B is well anodized, as shown in Fig. 5(b), despite the fact that not many Zr particles are evenly distributed on the Mg surface during the electrodeposition process due to the large particle size of ZrO_2. ZrO_2 must be measured on a nanoscale to achieve optimal electrodeposition results [28].

In Figure 5(c), the coating was applied in a single step, with anodizing and electrophoretic deposition occurring concurrently for 30 minutes at a constant electric current of 1 A. Because of the rectifier used, the coating does not function as intended. The rectifier used has a maximum capacity of 15 volts and 1 amp current. The rectifier did not reach that number during the experiment using a variable volt with 5 volts, 10 volts, and 15 volts because the current generated was very large. Changing the variables into a suspension solution requires the addition of the chemical compounds $Na_2O_7SiO_3$ and Al_2O_3.

The coating process has an effect on the surface of Magnesium AZ31B when the dry color changes slightly to black and a pale white line appears. The surface of Magnesium AZ31B forms a porous layer in several places, indicating that it is well anodized, despite the fact that not many Zr particles are evenly distributed on the Mg surface during the electrodeposition process, as shown in Fig. 5(c). Many factors can contribute to this, including a coarse sanding process for Mg and zircon particles that are not yet nanoscale.

The two-stage coating process produces better results than the one-stage coating process. Figure 5(b) shows that the pores formed by the anodizing results and the ZrO2 attached to the magnesium surface are becoming more evenly distributed across the entire surface. When compared to a single-stage coating process, less adhering ZrO_2 occurs because fewer pores or oxide layers are formed (Fig. 5(c)).

Tabel 8. EDS of hybrid coating magnesium AZ31B

Element	Mass%
O k	14.9482
Na k	10.6089
Mg k	68.5592
Al k*	2.4567
Si k	1.707
K k	1.353
Zr k*	0.3647

The two-stage coating process achieves better results on the surface coating of Magnesium AZ31B. Oxide formed on the surface of the AZ31B magnesium substrate while forming a porous surface. With an oxidant layer and pores on the surface, ZrO_2

adheres more easily and is more evenly distributed on the surface during the electrodeposition process. According to the EDS results, several elements were detected on the surface of Magnesium AZ31B, which are listed in Table 6.

4. CONCLUSION

Using synthesized Na_2SiO_3 and ZrO_2, anodizing electrodeposition hybrid coating on the surface of Magnesium AZ31B was successfully completed. The synthesis of Na_2SiO_3 yielded nearly identical results in all three batches, with only the crystal form differing. This result indicated the presence of silanol and siloxane groups. Batch 2 calcination yields the best ZrO_2 calcination results in the absence of Cl_2 impurities.

The two-stage coating process outperforms the one-stage coating process. Because the two-stage coating process maximizes the formation of the oxide layer, ZrO_2 in the electrodeposition process adheres better and is more evenly distributed on the surface. However, producing ZrO_2 with a smaller size (nm scale) is required so that ZrO_2 can be more easily attached to the magnesium surface.

ACKNOWLEDGMENT

The author would like to thank the "National Research and Innovation Agency's Research Center for Metallurgy" for organizing this activity.

REFERENCES

[1] D. Bombac, M. Brojan, P. Fajfar, and F. Kosel, "Review of materials in medical applications", *RMZ-Materials and Geoenvironment.*, vol. 54, no. 4, pp. 471-499, 2007.

[2] O.O. Ige, L. E. Umoru, M. O. Adeoye, A. R. Adetunji, O. E. Olorunniwo, and I. I. Akomolafe, "Monitoring, control, and prevention practices of biomaterials corrosion-an overview", *Trends in Biomaterials Artificial Organs.*, vol. 23, pp. 93-104, 2009.

[3] S. V. Gohil, S. Suhail, J. Rose, T. Vella, and L. S. Nair, "Polymers and composites for orthopedic applications," *Journal of Materials and Devices for Bone Disorders,* chapter. 8, pp. 349-395, 2020.

[4] E. Göktürk and H. Erdal, "Biomedical applications of polyglycolic acid (PGA)," *Journal of Sakarya Üniversitesi Fen Bilimleri Enstitüsü Dergis,* vol. 21, no. 6, pp. 1237-1244, 2017. Doi: 10.16984/saufenbilder.283156.

[5] Nowosielski, R; Cesarz, K; Babilas, R. "Structure and corrosion properties of Mg70-xZn30Cax(x=0.4) alloys for biomedical applications." *Journal of Achievements in Materials and Manufacturing Engineering,* vol. 58, no. 1, pp. 7-15, 2013.

[6] G. Chandra, and A. Pandey, "Biodegradable bone implants in orthopedic applications: a review", *Biocybernetics and Biomedical Engineering*, vol. 40, pp. 596-610. 2020. Doi : 10.1016/j.bbe.2020.02.003.

[7] Y. F. Zheng, X. N. Gu, F. Witte, "Biodegradable metals." *Materials Science and Engineering Reports*, vol. 77, pp. 1-34, 2014. Doi : 10.1016/h. mser.2014.01.001.

[8] S. X. Zhang, C. Zhang, J. Zhao, J. Li, Y. X. Song, H. Tao, Y. Zhang, Y. Hey, Y. Jiang, and Y. Bian. "Research on an Mg-Zn Alloy as a degradable biomaterial." *Acta Biomaterialia*, vol. 6, no. 2, pp. 626-40, 2010. Doi:10.1016/j.actbio.2009.06.028.

[9] H. Waizy, J. M. Seits, R. Janin, "Biodegradable magnesium implants for orthopedic applications", *Journal of Materials Science.*, vol. 48, pp. 39-50, 2013.

[10] L. Chang, L. Tian, W. Liu, "Formation of dicalcium phosphate dihydrate on magnesium alloy by micro-arc oxidation coupled with hydrothermal treatment" *Corrosion Science*, vol. 72, pp. 118-124, 2013.

[11] P. Rosemann, and J. Schmidt, "Short and longterm degradation behavior of Mg-1Ca magnesium alloys and protective coatings based on plasma-chemical oxidation and biodegradable polymer coating in synthetic body fluid" *Materials and Corrosion*, vol. 64, no. 8, pp. 714-722, 2013.

[12] H. S. Brar, and B. P Jordan, "A study of a biodegradable Mg–3Sc–3Y alloy and the effect of self-passivation on the in vitro degradation" *Acta Biomaterialia*, vol. 9, no. 2, pp. 5331-5340, 2013.

[13] G. Song, "Control of biodegradation of biocompatable magnesium alloys," *Corrosion Science*, vol. 49, no. 4, pp. 1696-1701, 2007.

[14] F. Witte, V. Kaese, H. Haferkamp, E. Switzer, and A. M. Linderberg, C. J.

Wirth, H. Windhagen, “In vivo corrosion of four magnesium alloys and the associated bone response”, *Biomaterials*, vol. 26, pp. 3557-3563, 2005.

[15] C. E. Wen, M. Mabuchi, Y. Yamada, K. Shimojima, Y. Chino, “Processing of biocompatible porous Ti and Mg”, *Scripta Material*, vol. 45, pp.1147-53, 2001.

[16] M. B. T. Sofyan, O. Susanti, “Magnesium and its alloys as biomaterials: A literature review,” *Proceeding of Annual National Seminar on Mechanical Engineering XV*, 2016.

[17] G. B. Darband, M. Aliofkhazraei, PHamghalam, N. Valizade, “Plasma electrolytic oxidation of magnesium and its alloys: Mechanism, properties and applications”, *Journal of Magnesium and Alloys*, vol. 5, pp. 74-132, 2017.

[18] A. Galio, S. Lamaka, M. Zheludkevich, L. Dick, I. Müller, M. Ferreira, “Inhibitor-doped sol–gel coatings for corrosion protection of magnesium alloy AZ31”. *Surface & Coatings Technology*, vol. 204, pp. 1479-1486, 2010. Doi : 10.1016/j.surfcoat.2009.09.067.

[19] Yin Zheng-Zheng., Qi Wei-Chen. “Advances in coating on biodegradable magnesium alloys”. *Journal of Magnesium and Alloys*, vol. 8, pp. 42-65, 2020. Doi : 10.1016/j.jma.2019.09.008.

[20] J. Gayle and A. Mahapatro,” Magnesium based biodegradable metallic implant materials: Corrosion control and evaluation of surface coatings”, *Journal of Innovations in Corrosion and Materials Science,* vol. 9, pp. 3-27, 2019. Doi : 10.2174/2352094909666190228113315.

[21] Riszki, I. Trivina and Harmami, “The effect of temperature on the quality of coating type 304 stainless steel with chitosan by electrophoresis”, *Jurnal Sains dan Seni ITS*, vol. 4, no.1, pp. 2337-3520, 2015.

[22] I. K. Suarsana, “The effect of nickel plating time on copper in decorative chromium plating on the brightness level and layer thickness”, *Cakram: Scientific Journal of Mechanical Engineering*, vol. 2, pp. 48-60, 2008.

[23] Basmal, Bayuseno, S. Nugroho, ”Pengaruh suhu dan waktu pelapisan tembaga nikel pada baja karbon rendah secara electroplating terhadap nilai ketebalan dan kekasaran”, *Rotasi*, vol. 14, no. 2, pp. 23-28, 2013.

[24] F. H. Shünemann, M. E. G. Vinueza, R. Margini, M. Fredel, F. Silva, J. C. M. Souza, Y. Zhang, B. Henriques, “Zirconia surface modifications for implant dentistry”, *Journal of Materials Science & Engineering*, vol. 98, pp. 1294-1305, 2019. Doi : 10.1016/j.msec.2019.01.062.

[25] L. Trivana, S. Sugiarti, and E. Rohaeti, “Synthesis and characterization of sodium silicate (Na_2SiO_3) from rice husk”, *Journal of Environmental Science & Technology*, vol 7, no. 2, pp. 66-75, 2015.

[26] I. Nurhidayati, E. T. Wahyuni, H. A. Nurul, and R. H. Sarwendah, “Effect of stirring time on sodium silicate synthesis from mount kelud volcanic ash”, *Alchemy: Journal of Chemistry*, vol. 9, no. 2, pp. 48-53, 2021.

[27] Sriyanti, Taslimah, Nuryono, and Narsito, “Sintesis bahan hibrida amino-silika dari abu sekam padi melalui proses sol-gel”, *Jurnal Kimia Sains dan Aplikasi*, vol. 8, no. 1, pp. 1-8, 2005. Doi : 10.14710/jksa.8.1.1-8.

[28] R. Chaharmahali, A. Fattah-alhosseini, M. Nouri, and K. Babaei, “ Improving surface characteristics of PEO coatings of Mg and its alloys with zirconia nanoparticles: A review”, *Applied Surface Science Advances*, vol. 6, 100131, 2021. Doi : 10.1016/j.apsadv.2021.100131.

Metalurgi (2022) 3: 105 - 112

METALURGI
Majalah Ilmu dan Teknologi
p-ISSN 0126-3188 | e-ISSN 2443-3926
ejurnalmaterialmetalurgi.lipi.go.id

MORPHOLOGY AND RESISTIVITY VALUES OF FLUORINE-DOPED TIN OXIDE (FTO) USING INDONESIAN LOCAL DIMETHYL TIN DICHLORIDE (DMTC) PRECURSORS

Aptri Mira Rizki[1], Fariza Eka Yunita[2], Latifa Hanum Lalasari[2], Januar Irawan[2], Tri Arini[2,*], Florentinus Firdiyono[2], Akhmad Herman Yuwono[3], Lia Andriyah[2], Nadia Chrisayu Natasha[2]

[1]Department of Chemistry, Universitas Sebelas Maret
Jalan Ir. Sutami 36 Kentingan, Surakarta, Jawa Tengah, Indonesia 57126
[2]Research Center for Metallurgy, National Research and Innovation Agency
Management Building 720, B.J. Habibie Sains and Technology Area, Banten, Indonesia 15314
[3] Departments of Metallurgical and Materials Engineering, Universitas Indonesia
Kampus UI Depok, Jawa Barat, Indonesia, 16425
*E-mail: tria009@brin.go.id

Received: 07-11-2022, Revised: 23-11-2022, Accepted: 31-12-2022

Abstract

TCO (transparent conductive oxide) is the main component for solar cell fabrication. One of the promising types of TCO is FTO (fluorine-doped tin oxide). The method used in depositing the conductive layer of FTO is spray pyrolysis with an ultrasonic nebulizer. The precursor used is a local Indonesian product, DMTC (dimethyltin dichloride) with doping ammonium fluoride (NH_4F). The variable that used in this study were variations in deposition time (5, 10, 15, 20, and 25 minutes) with a fixed substrate temperature at 300 °C and doping variations (un-doped, 2 wt.% doped, and 8 wt.% doped) to see the effect of adding F doping to the precursor solution. The resistivity values with a variation of deposition time 5, 10, 15, 20, and 25 minutes (2 wt.% doped) are $0.218x10^{0}$; $0.449x10^{-1}$; $1,567x10^{-2}$; $0.676x10^{-2}$ $0.377x10^{-2}$ Ω.cm. For doping variations (un-doped, 2 wt.% doped, and 8 wt.% doped) the values are $0.883x10^{-2}$; $0.377x10^{-2}$; $0.506x10^{-3}$ Ω.cm. The resistivity values tend to decrease with an increase in deposition time and doping addition, resulting in enhanced conductivity. The grain size will increase as deposition time and doping are both increased. In this study, the optimal resistivity value of 0.377x10-2.cm was obtained at a deposition time of 25 minutes with 2 wt.% doping.

Keywords: *FTO (fluorine-doped tin oxide), DMTC (dimethyltin dichloride), deposition time, doping, resistivity*

1. INTRODUCTION

Indonesia is an archipelagic country located on the equator and in a ring of fire, so it has potential sustainable power such as wind, solar, and geothermal. The angle of the sunlight is shallow on the equator, so the solar energy that falls per unit area is more extensive. The utilization of solar energy can be used as an alternative energy source in overcoming the energy crisis because it enhances sustainability and reduces pollution. The radiant light from the sun can generate electricity by utilizing solar cell technology. DSSC (dye-sensitized solar cell) is among the solar cells that can be used which is simple and flexible so that it can be used in various applications, and its fabrication requires low costs [1].

In DSSC manufacturing, one of several main components needed is a TCO (transparent conductive oxide) or transparent conductive glass. Tin oxide (SnO_2) is a semiconductor with good electrical and optical performance, so it is extensively utilized as a transparent conductor for various applications [2]. SnO_2 has been developed as a result of its low production costs, its resistance to atmospheric conditions [3], and responsiveness to several gase [4]. The optical and electrical performance of the tin oxide film could be improved thru doping with ITO (indium

DOI : 10.14203/metalurgi.v37i3.685

Metalurgi is Sinta 2 Journal (https://sinta.ristekbrin.go.id/journals/detail?id=3708) accredited by Ministry of Research & Technology, Republic Indonesia

tin oxide) [5], ATO (antimony tin oxide) [6], or FTO (fluorine tin oxide) [7]. The most common tin oxide film commercialized is ITO. However, the material cost for ITO is extremely limited and expensive, so FTO is an alternative to ITO because it is less expensive [4] and requires more accessible raw materials. The electrical properties of tin oxide film are highly dependent on oxygen stoichiometry [3]. Various types of deposition techniques are chemical vapor deposition [8], sputtering [9], sol-gel method [10], spin coating [11], and spray pyrolysis [12].

The most widely used precursors in FTO manufacturing are $SnCl_2.2H_2O$ (dihydrated tin (II) chloride) [13]-[14] and $SnCl_4.5H_2O$ (Tin (IV) chloride pentahydrate) [15]. Several previous studies have conducted experiments using DMTC (dimethyltin dichloride) precursors, but most used CVD (chemical vapor deposition) method in their research. Mannie, G.J.A studied the surface characteristics of tin oxide thin films through CVD method utilizing TTC (tin tetrachloride) precursors, DMTC, and MBTC (monobutyl tin trichloride) [8]. Van Mol et. al., [16] studied the decomposition of DMTC in pure N_2 using a CSTR reactor at T = 370-630 °C and p = 1 bar. He observed the production of methane, ethane, ethylene, and propane by FTIR and QMS during the decomposition of DMTC at 500 °C and found no evidence of the presence of HCl and CH_3Cl.

This research used a local product precursor produced in Indonesia as DMTC as an alternative precursor to make FTO conductive layer utilizing the ultrasonic spray pyrolysis nebulizer technique. In this investigation, the influence of deposition time and fluorine (NH_4F) doping on the morphology and physical properties of the FTO conductive layer was determined.

2. MATERIALS AND METHODS

The first stage of this research was to wash the substrate glass (soda lime glass) gradually. First, the substrate is cleaned using detergent to eliminate grease and dirt. Then it is placed within a beaker filled with acetone and vibrated using an ultrasonic cleaner for 15 minutes, dried, and put in a storage container.

The precursor solution was made by mixing 0.9 M of Indonesian $C_2H_6Cl_2Sn$ (dimethyl tin dichloride) with 86 ml of distilled water for 30 minutes. The solution was then treated for 30 minutes with various concentrations of ammonium fluoride (98%, Merck Ltd., Germany). The method chosen for depositing the solution in this study was spray pyrolysis using an ultrasonic nebulizer (GEA Medical 402A1) at a speed of ± 30 ml / 10 minutes and a distance of 10 cm. Spray pyrolysis, in particular, is one of the promising deposition techniques because it is simple, reliable, and economical [17]. The variations used in this study were deposition times of 5, 10, 15, 20, and 25 minutes at 300 °C temperature. The morphology of this FTO (fluorine tin oxide) thin layer was characterized utilizing a SEM-EDS (scanning electron microscope-energy dispersive spectrometry) (JEOL-JSM 6390A) while the electrical parameter, such as resistivity, was measured using a four-point probe (FPP5000).

3. RESULT AND DISCUSSION

3.1 Deposition Time Effect

SEM (scanning electron microscope) analysis in Fig. 1 shows that adding deposition time will result in significant morphological changes.

Figure 1(a) reveals that after 5 minutes of deposition, the surface morphology of the layer is flat and smooth. It consists of small refined grains with a particle size diameter in the range of 39.40-53.81 nm. The particle size diameter increased to 46.65-100.32, 82.07-34.40, and 99.04-150.31 nm as deposition time was increased to 10, 15, and 20 minutes. The granules become denser and more interconnected as the porosity is significantly decreased. The largest particle size was obtained at the deposition time of 25 minutes. According to Table 1, the diameter of the particles was between 604.37 and 832.01 nm. The particle size will grow as deposition time increases. After allowing new nucleation to form, adjacent grains start to collide, causing an increase in internal stress that is reduced by the forming of a more excellent crystalline structure [18].

Table 1. The particle size of the FTO conductive layer with variations in deposition time with a doping ratio of 2 wt.% and a substrate temperature of 300 °C using SEM analysis

Time (minutes)	Particle Size (nm)
5	37.95 - 53.81
10	46.65 - 100.32
15	82.07 - 134.40
20	99.04 - 146.48
25	604.37 - 832.01

According to the semi-qualitative and semi-quantitative EDS (energy dispersive spectrometry) analysis, the conductive FTO (fluorine tin oxide) layer depicted in Figure 2 contains O and Sn, which are obtained from the precursor solution of dimethyl tin dichloride. ($C_2H_6Cl_2Sn$). In contrast, Mg, Ca, Na, Si are derived from substrate constituent elements (glass soda-lime) [19]. The presence of a glass element in the film indicates that the positioning process has not occurred completely. Figure 2 depicts a semi-quantitative

analysis showing that the FTO thin layer consists primarily of SnO_2.

Figure 2 indicates that the concentrations of Sn and O fluctuate. Sn elements are dominant from time to time because Sn elements with larger molecular weights tend to stick more to the substrate than the F dopant when given heating treatment and at a longer deposition process. This phenomenon proves that as the deposition time getting longer, the higher the probability that the F dopant in the form of gas will experience two conditions when the substrate is heated, namely, some of the F dopant sticks to the substrate and the other evaporates into the air [20]. The F content appears undetectable by the semi-quantitative EDS test because the F content is minimal. This finding is in agreement with the experiment performed by Bilgin et. al., [21], that the F doping element only functions as a catalyst to produce SnO_2 compounds with better structure and quantity.

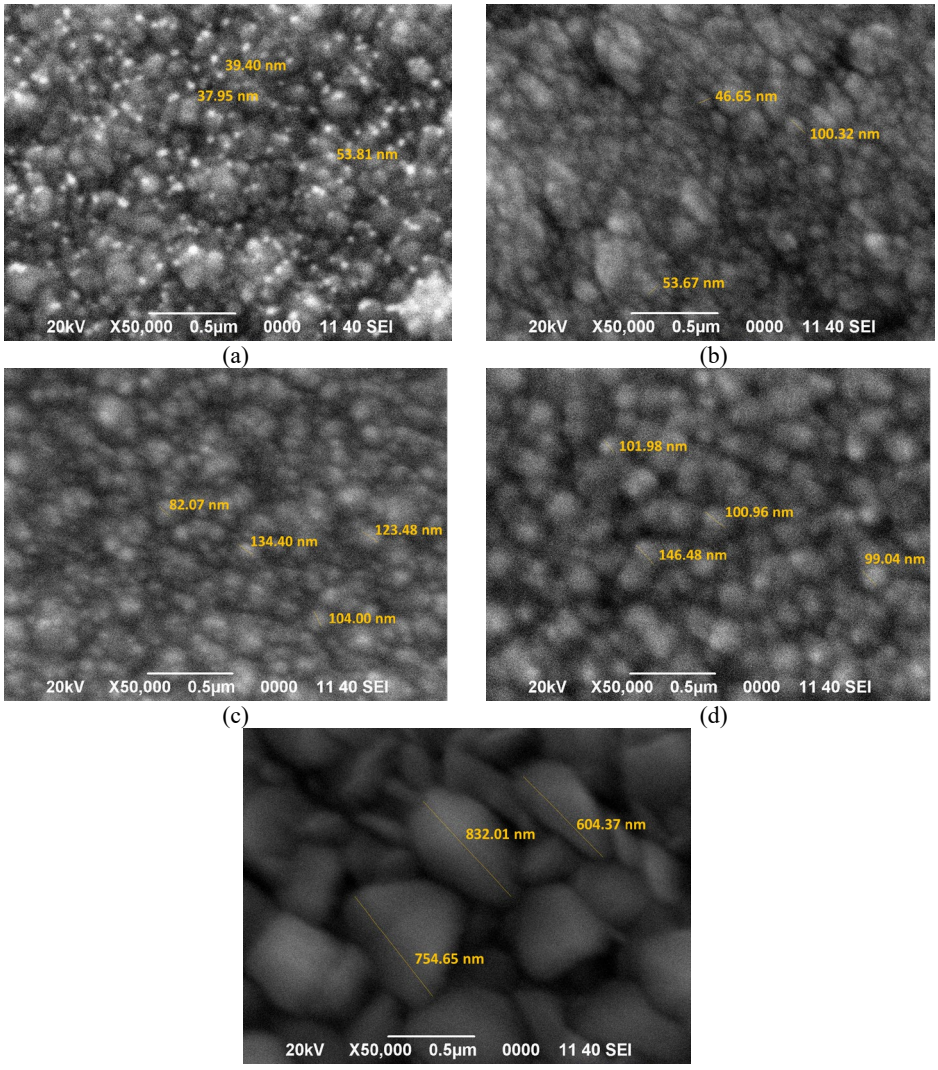

Figure 1. Morphology of SnO_2 thin layer, doping ratio 2 wt.% and substrate temperature 300 °C with variation of deposition time; (a) 5, (b) 10, (c) 15, (d) 20, and (e) 25 minutes

Figure 3 is a cross-sectional SEM image of the FTO conductive layer (top side) and glass substrate (bottom side), resulting from deposition on the substrate within 20 and 25 minutes. From Figure 3, it can be seen that the layer thickness is 560-600 nm at 20 minutes and the layer thickness is 1.28-1.36 µm at 25 minutes. With increasing deposition time, the collision of elemental fluorine ions on SnO_2 will continue. The longer the collision, the thicker the surface layer will be [22]. There was a linear relationship between the thickness and the deposition time between 20 and 25 minutes. This result is consistent with the report from previous authors [23]-[24].

Table 2. Resistivity values with varying deposition time, doping ratio 2 wt.% and substrate temperature 300 °C

Time (minutes)	Resistivity (Ω.cm)
5	0.218×10^{0}
10	0.449×10^{-1}
15	1.567×10^{-1}
20	0.676×10^{-2}
25	0.377×10^{-2}

The resistivity of the SnO_2 thin layer versus deposition time is shown in Table 2. The resistivity value decreases as deposition time increases. This finding suggests that the conductivity value improves with increasing deposition time. Generally, an increase in the thickness of a thin layer causes the resistivity to decrease [25]. Conductivity is the ability of a material to conduct electric current. It is the inverse of electrical resistivity. Therefore, increasing the thickness of the thin layer increases its conductivity. As deposition time increases, the SnO_2 particles become denser, thereby lowering porosity, and the interconnection becomes more interconnected, electronic transfer between particles becomes smoother, and the resistivity is considerably decreased [26].

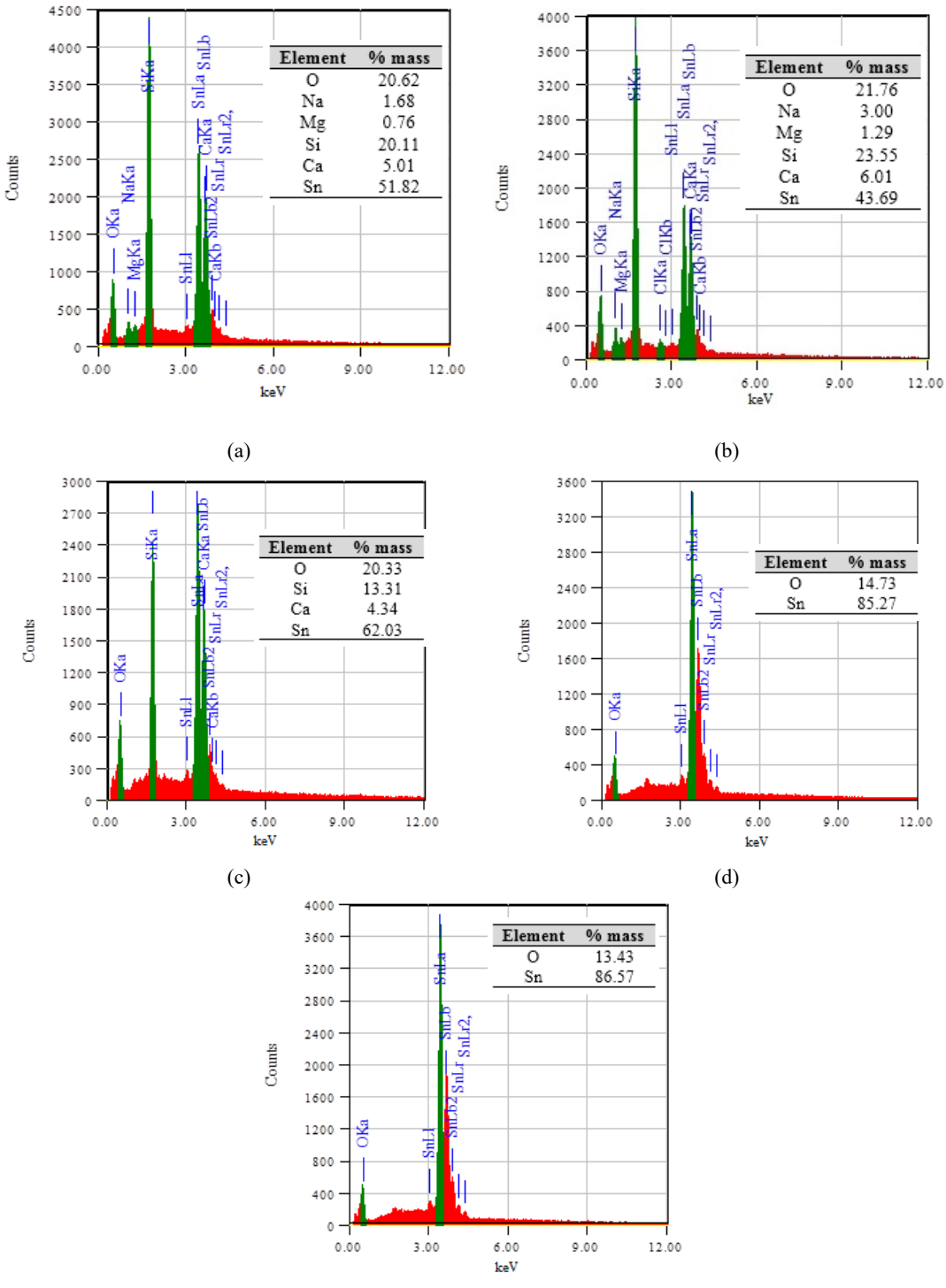

Figure 2. Semi-qualitative graph of EDS of the FTO conductive layer at deposition time variations with a doping ratio of 2 wt.% and a substrate temperature of 300 °C using EDS-SEM analysis (a) 5, (b) 10, (c) 15, (d) 20, and (e) 25 minutes

3.2 Doping Effect

Figure 4 depicts the surface morphology of FTO thin films with varying doping levels, coated for 25 minutes and 300 °C substrate. The surface morphology of the non-doped layer has a particle size diameter of 99.66-228.04 nm. There was an increase in the particle size diameter to 496.06-596.01 and 868.00-1290.00 nm with the addition of 2 wt.% and 8 wt.%, respectively, as shown in Table 3.

According to the SEM analysis, the surface morphology of the undoped thin layer consists of small grains, whereas the particle size increases with the addition of doping. According to research conducted by P. Yao [27] and D. Tatar [28], the grain size increases as the doping level rises. The results are consistent with these findings. The morphology of the crystals gets bigger with increasing doping levels because the crystals are getting denser, and there is an agglomeration process [29]. The agglomeration process involves the accumulation of nanoparticle-sized solids in order to produce larger crystals.

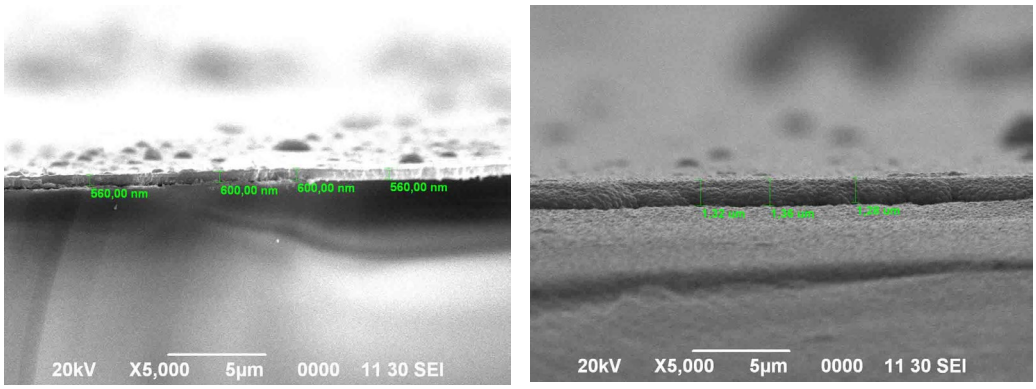

(a) (b)

Figure 3. Cross-sectional view of the FTO thin layer, doping ratio 2 wt.% And substrate temperature 300 °C with varying deposition time (a) 20, and (b) 25 minutes

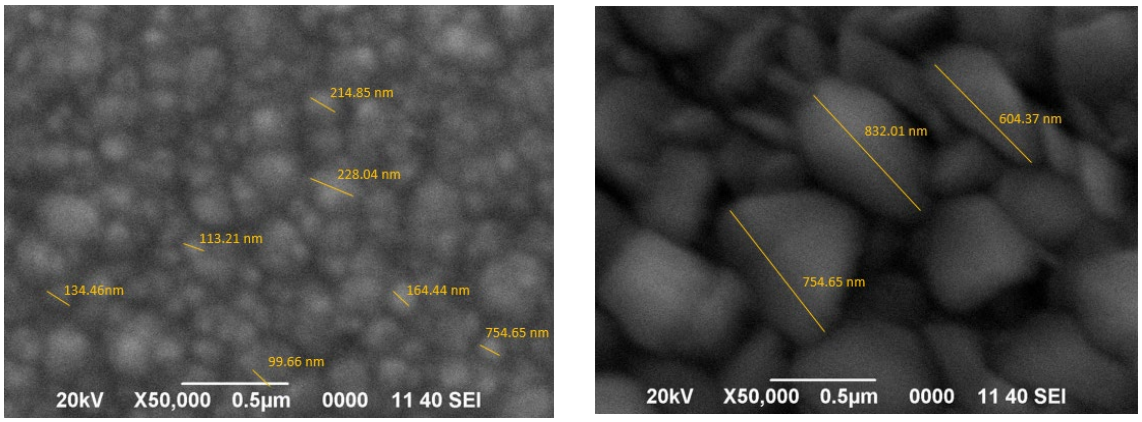

(a) (b)

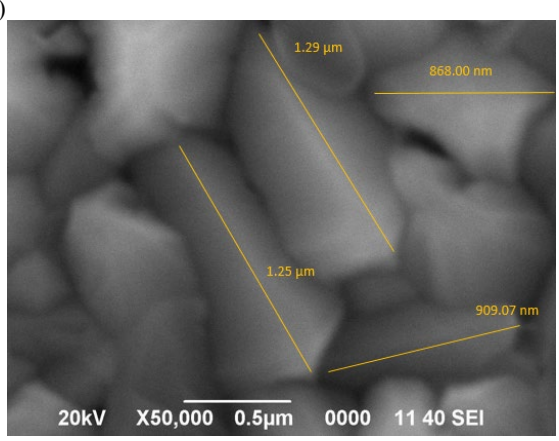

(c)

Figure 4. Morphology of the SnO_2 thin layer, deposition time of 25 minutes and substrate temperature of 300 °C with doping variations; (a) undoped, (b) 2 wt.%, (c) 8 wt.%

DOI : 10.14203/metalurgi.v37i3.685

Metalurgi is Sinta 2 Journal (https://sinta.ristekbrin.go.id/journals/detail?id=3708) accredited by Ministry of Research & Technology, Republic Indonesia

EDS analysis of chemical content of thin films in Fig. 5 shows that the elements of Sn and O are more dominant in thin films. However, element F was not detected in the thin layer. Gaseous Element F is difficult to identify with EDS. Furthermore, the small concentration of this element in the original solution may limit the detection of this element. Figure 5 shows that the incorporation of F increases the number of Sn elements. Since the diameter of the fluorine ion (F^-: 0.133 nm) is nearly identical to oxygen (O^{2-}: 0.132 nm), a rise in the Sn/O ratio shows the effective doping of F through to the lattice as either an interstitial or an oxygen substitution [7], [21].

According to Table 4, NH_4F addition will impact the resistivity of the thin layer. The undoped film has a greater resistivity value than the doped layer. As doping increases, the resistivity value lowers. According to prior studies, the doping amount effects the stoichiometric of the SnO2 thin layer. As the doping level increases, the thin film becomes nonstoichiometric, wherein fluorine atoms with ionic surface mobility scattered on the specimen surface increase with doping, causing the grain size to increase, grain boundaries decrease so that the electrical properties increase [28].

Table 3. The particle size of the conductive FTO layer with the effect of adding doping, deposition time of 25 minutes, and substrate temperature of 300 °C using SEM analysis

Doping	Particle Size (nm)
Undoped	99.66 – 228.04
2 wt.%	496.06 – 596.01
8 wt.%	868.00 – 1290.00

This is in accordance with previous studies, which demonstrates that the resistance drops with increasing doping concentrations after doping with 30 F/Sn atomic% but then increases at doping levels greater than 70 F/Sn atomic% [30]-[31].

Table 4. The results of the resistivity test for doping variations with a deposition time of 25 minutes and a substrate temperature of 300 °C

Doping	Resistivity (Ω.cm)
0 wt.%	0.883×10^{-2}
2 wt.%	0.377×10^{-2}
8 wt.%	0.506×10^{-3}

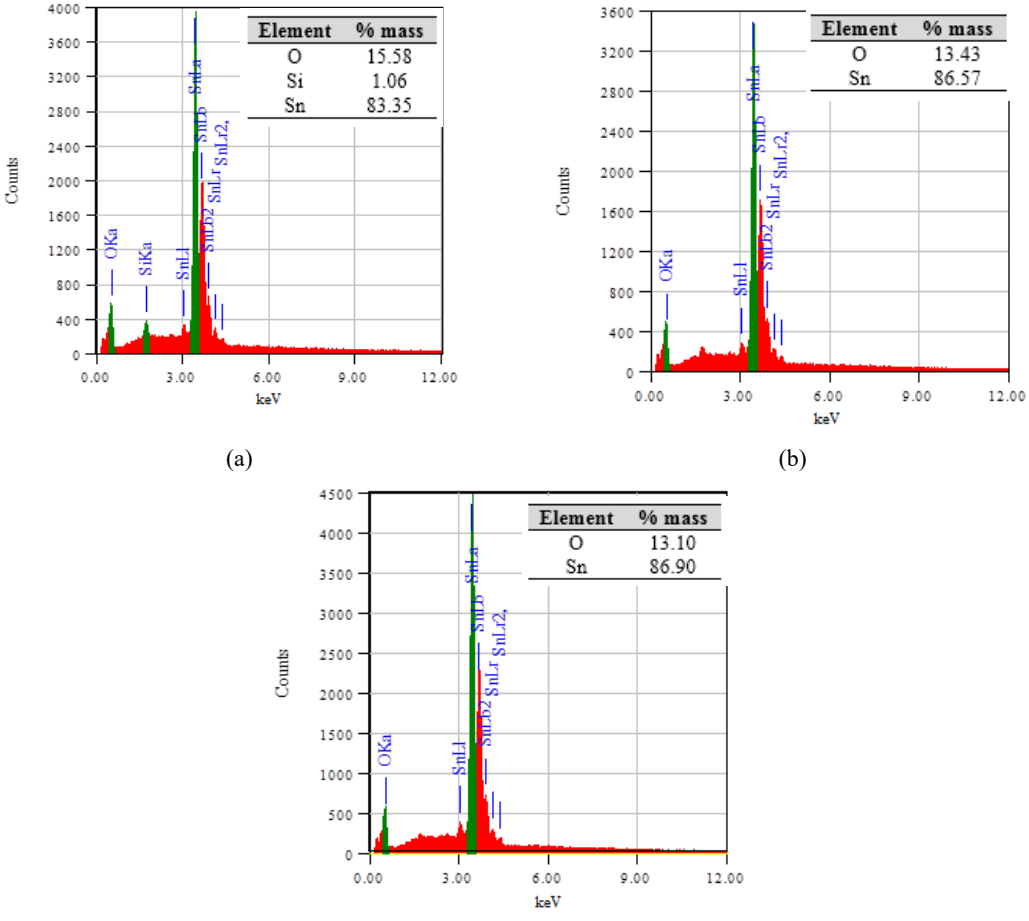

Figure 5. Semi-qualitative graph of EDS of the conductive FTO layer at doping variations with a deposition time of 25 minutes and a substrate temperature of 300 °C using EDS-SEM analysis (a) Undoped, (b) 2 wt.%, and (c) 8 wt .%

DOI : 10.14203/metalurgi.v37i3.685

Metalurgi is Sinta 2 Journal (https://sinta.ristekbrin.go.id/journals/detail?id=3708) accredited by Ministry of Research & Technology, Republic Indonesia

4. CONCLUSION

FTO (flourine tin oxide) conductive layer production by spray pyrolysis method utilizing an ultrasonic nebulizer generated a comparatively good layer with the smallest resistivity value of $0.377x10^{-2}$ Ω.cm at a time deposition of 25 minutes and 2 wt.% doping. As deposition time increases, the larger the grain size will be, which causes the conductive layer to be thicker. The effect of increasing the thickness of the conductive layer will result in a decrease in the resistivity value so that better conductive properties will be obtained.

ACKNOWLEDGMENT

This study was supported by the National Research and Innovation Agency's Thematic Research Grant Year 2019 for the Research Center for Metallurgy. The author would also like to thank PT Timah Industri for the assistance provided by the precursors and all parties who assisted in the completion of this research.

REFERENCES

[1] B. R. Koo, D. H. Oh, D. H. Riu, and H. J. Ahn, "Improvement of transparent conducting performance on oxygen-activated fluorine-doped tin oxide electrodes formed by horizontal ultrasonic spray pyrolysis deposition," *ACS Appl. Mater. Interfaces*, vol. 9, no. 51, pp. 44584-44592, 2017. Doi : 10.1021/acsami.7b12968

[2] A. V. Moholkar, S. M. Pawar, K. Y. Rajpure, S. N. Almari, P. S. Patil, and C. H. Bhosale, "Solvent-dependent growth of sprayed FTO thin films with mat-like morphology," *Sol. Energy Mater. Sol. Cells*, vol. 92, no. 11, pp. 1439-1444, 2008. Doi :10.1016/j.solmat.2008.06.010

[3] N. Memarian, S. M. Rozati, E. Elamurugu, and E. Fortunato, "Characterization of SnO_2:F thin films deposited by an economic spray pyrolysis technique," *Phys. Status Solidi Curr. Top. Solid State Phys.*, vol. 7, no. 9, pp. 2277-2281, 2010. Doi :10.1002/pssc.200983738.

[4] Z. Ramdhan and A. Doyan, "Preliminary study flourine tin oxide (FTO) using sol-gel spin coating techniques," vol. 10, no. 2, pp. 27-30, 2018. Doi : 10.9790/4861-1002032730.

[5] H. Cho and Y. Yun, "Characterization of indium tin oxide (ITO) thin films prepared by a sol-gel spin coating process," *Ceram. Int.*, vol. 37, no. 2, pp. 615-619, 2011. Doi :10.1016/j.ceramint.2010.09.033.

[6] T. M. Hammad, N. K. Hejazy, G. Strip, and G. Branch, "Structural, electrical and optical properties of ATO thin films fabricated by dip coating method," *Int. Nano Lett.*, vol. 1, no. 2, pp. 123-128, 2011. Doi : 10.1186/2228-5326-2-7.

[7] Z. Y. Banyamin, P. J. Kelly, G. West, and J. Boardman, "Electrical and optical properties of fluorine doped tin oxide thin films prepared by magnetron sputtering," *Coatings*, vol. 4, pp. 732-746, 2014. Doi : 10.3390/coatings4040732.

[8] G. J. Mannie, *Surface chemistry and morphology of tin oxide thin films grown by chemical vapor deposition*. Dissertation, Eindhoven University of Technology, The Netherlands, 2013. Doi : 10.6100/IR751861.

[9] T. Jäger, B. Bissig, M. Döbeli, A. N. Tiwari, and Y. E. Romanyuk, "Thin films of SnO2:F by reactive magnetron sputtering with rapid thermal post-annealing," *Thin Solid Films*, vol. 553, pp. 21-25, 2014. Doi : 10.1016/j.tsf.2013.12.038.

[10] Y. Lin and C. Wu, "The properties of antimony-doped tin oxide thin films from the sol-gel process," *Surf. Coatings Technol.*, vol. 88, pp. 239-247, 1996. Doi : 10.1016/S0257-8972(96)02926-X.

[11] L. Muliyadi, A. Doyan, S. Susilawati, and S. Hakim, "Synthesis of SnO_2 thin layer with a doping fluorine by sol-gel spin coating method," *J. Penelit. Pendidik. IPA*, vol. 5, no. 2, pp. 175, 2019. Doi : 10.29303/jppipa.v5i2.257.

[12] Y. Ren, G. Zhao, and Y. Chen, "Fabrication of textured SnO_2: F thin films by spray pyrolysis," *Appl. Surf. Sci.*, vol. 258, no. 2, pp. 914-918, 2011. Doi : 10.1016/j.apsusc.2011.09.026.

[13] D. S. D. Amma, V. K. Vaidyan, and P. K. Manoj, "Structural, electrical and optical studies on chemically deposited tin oxide films from inorganic precursors," *Mater. Chem. Phys.*, vol. 93, no. 1, pp. 194-201, 2005. Doi : 10.1016/j.matchemphys.2005.03.045.

[14] D. Fikri, A. H. Yuwono, N. Sofyan, T. Arini, and L. H. Lalasari, "The effect of substrate heating temperature upon spray pyrolysis process on the morphological and functional properties of fluorine tin oxide conducting glass," *AIP Conf. Proc. 1826*, vol. 20003-1-0, 2017. Doi : 10.1063/1.4979219.

DOI : 10.14203/metalurgi.v37i3.685

Metalurgi is Sinta 2 Journal (https://sinta.ristekbrin.go.id/journals/detail?id=3708) accredited by Ministry of Research & Technology, Republic Indonesia

[15] C. Luyo, I. Fabregas, L. Reyes, J. L. Solís, J. Rodríguez, W. Estrada, and R. J. Candal, "SnO_2 thin-films prepared by a spray-gel pyrolysis: Influence of sol properties on film morphologies," *Thin Solid Films*, vol. 516, no. 1, pp. 25-33, 2007. Doi : 10.1016/j.tsf.2007.05.023.

[16] A. M. B. Van Mol, M. H. J. M. De Croon, C. I. M. A. Spee, and J. C. Schouten, "Kinetic mechanism of the decomposition of dimethyltin dichloride," *J. Phys. IV JP*, vol. 9 I, no. 8, 1999. Doi : 10.1051/jp4:1999820.

[17] A. Paraskevi and N. Munkegade, "Structural and sensing properties of nanocrystalline SnO_2 films deposited by spray pyrolysis from a $SnCl_2$ precursor," *Appl. Phys. A Mater. Sci. Process.*, vol. 91, pp. 667-670, 2008. Doi : 10.1007/s00339-008-4505-3.

[18] F. A. Garcés, N. Budini, R. R. Koropecki, and R. D. Arce, "Structural mosaicity and electrical properties of pyrolytic SnO_2:F thin films," *Thin Solid Films*, vol. 531, pp. 172–178, 2013. Doi : 10.1016/j.tsf.2013.01.020.

[19] T. Taniguchi and S. Ito, "Molecular dynamics simulation of the structure of soda-lime-silica glass," *Reports res. Lab. Asahi Glas. Ltd*, vol. 53, pp. 1-7, 2003.

[20] L. H. Lalasari, T. Arini, A. H. Yuwono, and F. Firdiyono, "Pengaruh pencampuran dan rasio dopan/prekursor dalam pembuatan lapisan tipis fluorine doped tin oxide (FTO) berbasis timah (II) klorida," pp. 105-114, 2015. Doi : 10.14203/metalurgi.v30i3.68.

[21] V. Bilgin, I. Akyuz, E. Ketenci, S. Kose, and F. Atay, "Electrical, structural and surface properties of fluorine doped tin oxide films," *Appl. Surf. Sci.*, vol. 256, no. 22, pp. 6586-6591, 2010. Doi : 10.1016/j.apsusc.2010.04.052.

[22] R. Rinaldi, A. Amri, and Khairat, "Sintesa fluorinated tin oxide (FTO) menggunakan prekursor ramah lingkungan dan penambahan graphene dengan metode deposisi spray coating untuk aplikasi material konduktif transparan," *Jom FTEKNIK*, vol. 3, no. 2, p. 10, 2016.

[23] G. C. Morris and A. E. McElnea, "Fluorine doped tin oxide films from spray pyrolysis of stannous fluoride solutions," *Appl. Surf. Sci.*, vol. 92, pp. 167-170, 1996. Doi : 10.1016/0169-4332(95)00224-3.

[24] A. E. Hassanien, H. Hashem, G. Kamel, S. Soltan, A. Moustafa, M. Hammam, and A. A. Ramadan, "Performance of transparent conducting fluorine-doped tin oxide films for applications in energy efficient devices performance of transparent conducting fluorine-doped Tin oxide films for applications in energy efficient devices," *Int. Journalof Thin Film. Sci. Technol.*, vol. 5, no. 1, pp. 55-65, 2016. Doi : 10.18576/ijtfst/050109.

[25] A. V Moholkar, S. M. Pawar, K. Y. Rajpure, P. S. Patil, and C. H. Bhosale, "Properties of highly oriented spray-deposited fluorine-doped tin oxide thin films on glass substrates of different thickness," *J. Phys. Chem. Solid*, vol. 68, pp. 1981-1988, 2007. Doi :10.1016/j.jpcs.2007.06.024.

[26] T. Arini, A. H. Yuwono, L. H. Lalasari, N. Sofyan, G. Ramahdita, F. Firdiyono, A. Subhan, and C. Hudaya, "The Influence of deposition time and substrate temperature during the spray pyrolysis process on the electrical resistivity and optical transmittance of 2 wt.% fluorine-doped tin oxide conducting glass," *Int. J. Technol.*, vol. 8, pp. 1335-1343, 2016. Doi : 10.14716/ijtech.v7i8.7065.

[27] P. Yao, "Effects of Sb doping level on the properties of Ti / SnO_2-Sb electrodes prepared using ultrasonic spray pyrolysis," vol. 267, pp. 170-174, 2011. Doi : 10.1016/j.desal.2010.09.021.

[28] D. Tatar and B. Duzgun, "The relationship between the doping levels and some physical properties of SnO_2:F thin films spray-deposited on optical glass," *J. Phys.*, vol. 79, no. 1, pp. 137-150, 2012. Doi : 10.1007/s12043-012-0288-3.

[29] S. N. Sadikin, M. Y. A. Rahman, A. A. Umar, and M. M. Salleh, "Effect of spin-coating cycle on the properties of TiO_2 thin film and performance of DSSC," *Int. J. Electrochem. Sci.*, vol. 12, no. 6, pp. 5529-5538, 2017. Doi : 10.20964/2017.06.57.

[30] G. A. Velázquez-Nevárez, J. R. Vargas-García, L. Lartundo-Rojas, F. Chen, Q. Shen, and L. Zhang, "Preparation, characterization and electronic properties of fluorine-doped tin oxide films," *J. Wuhan Univ. Technol. Mater. Sci. Ed.*, vol. 31, no. 1, pp. 48-51, 2016. Doi : 10.1007/s11595-016-1328-5.

[31] M. Soliman, M. M. Hussein, S. El-atawy, and M. El-gamal, "Effect of fluorine

doping and spraying technique on the properties of tin oxide films," *Renew. Energy*, vol. 23, pp. 463-470, 2001. Doi : 10.1016/S0960-1481(00)00151-8.

Metalurgi (2022) 3: 113 - 118

METALURGI
Majalah Ilmu dan Teknologi
p-ISSN 0126-3188 | e-ISSN 2443-3926
ejurnalmaterialmetalurgi.lipi.go.id

IRON REMOVAL PROCESS FROM NICKEL PREGNANT LEACH SOLUTION USING SODIUM HYDROXIDE

Mochamad Afriansyah Zunaidi[a,*], Iwan Setiawan[b], Soesaptri Oediyani[a], Januar Irawan[b], Ahmad Rizky Rhamdani[b], Adi Noer Syahid[b]

[a]Metallurgical Engineering, Faculty of Engineering, University of Sultan Ageng Tirtayasa
Jl. Jendral Sudirman Km.3, Cilegon, Banten, Indonesia 42434
[b]Research Center for Metallurgy, National Research and Innovation Agency
Management Building 720, B.J. Habibie Sains and Technology Area, Banten, Indonesia 15314
*E-mail: mochafriansyah@gmail.com

Received: 24-07-2022, Revised: 10-11-2022, Accepted: 31-12-2022

Abstract

Indonesia is a country that has abundant mineral resources, including nickel resources in laterite ore. Nickel demand has risen significantly because of the need for nickel precursors for battery production. Nickel laterite can be processed via the hydrometallurgical route to obtain nickel precursor by leaching the laterite ore with an acid solution to produce a nickel-rich solution or PLS (pregnant leach solutions). This nickel-rich solution is then precipitated with a base solution to produce MHP hydroxides (mixed hydroxides precipitate). MHP is the primary product containing nickel and cobalt for the production of lithium battery material. PLS often contains iron impurities, which dissolve when the ore is leached. As a result, the iron must be separated in order to produce high-purity MHP. To address this issue, synthetic PLS with nickel, cobalt, and iron were created, and their concentration was simulated to match the general PLS composition. The experiment revealed that iron could be precipitated in two stages using 2.5 M NaOH solution at solution pH of 3 and 3.5. At a higher pH, nickel and cobalt can be precipitated. To investigate the effect of pH and temperature on the yield of nickel and cobalt precipitation, precipitation was carried out at pH 7, 8, and 9 and temperatures of 70, 80, and 90 °C. The results show that the highest yield was obtained at a pH of 9 and a temperature of 90 °C, with nickel and cobalt precipitation yields of 99.03% and 98.78%, respectively.

Keywords: *MHP (mixed hydroxide precipitate), iron removal, pH, temperature, precipitate*

1. INTRODUCTION

Indonesia is a country that has a wealth of natural resources and abundant mineral resources [1]. Many minerals have the potential to transform into nickel, such as sulfide compounds and oxide compounds (laterite ores) [2]. However, the dwindling amount of nickel sulfide reserves can be a problem to face in the future. Therefore, it is necessary to use laterite as a nickel source, although laterite ore contains lower nickel content than sulfide ore. Laterite nickel processing can be carried out through pyrometallurgical or hydrometallurgical processes [3]. In the nickel processing industry, hydrometallurgical nickel ore processing lines include the Caron Process, HPAL (high-pressure acid leaching), AL (agitation leaching), and HL (heap leaching) [4].

The intermediate product from the leaching process is usually called a PLS (pregnant leaching solution). The PLS is then processed by precipitation method to produce the final product, generally in the form of a MHP (mixture of hydroxide precipitate) or a MSP (mixture of sulfide precipitation). The PLS from the leaching process could also be processed before the precipitation process via a solvent extraction route to separate the dissolved metal into a different solution to produce higher-purity PLS [5]-[6]. MHP is a commercially proven technique [7]; MHP has a nickel content of around 3,8%-34%, while MSP is about 55%. MHP has received a lot of attention because it has several

DOI : 10.14203/metalurgi.v37i3.665

Metalurgi is Sinta 2 Journal (https://sinta.ristekbrin.go.id/journals/detail?id=3708) accredited by Ministry of Research & Technology, Republic Indonesia

advantages over the MSP method, such as easier precipitation to obtain nickel and cobalt as concentrates and a more accessible nickel and cobalt extraction process [8]-[9]. However, obtaining MHP precipitate with high nickel and cobalt content is challenging because there are too many impurities.

In this study, the MHP precipitation method was used, which previously carried out an iron removal process so that the precipitated nickel and cobalt could be free from iron compounds [10].

2. MATERIALS AND METHODS

The synthetic PLS (pregnant leaching solution) was prepared by first diluting a certain amount of nickel sulfate hexahydrate, cobalt sulfate heptahydrate, and iron sulfate separately in aquademin in an acidic condition. The solutions were mixed and diluted with aquademin to get 5 liters of PLS. The synthetic PLS was taken as much as 5 ml and diluted in a volumetric flask up to 100x dilution to be analyzed for elemental content using ICP-OES (inductively coupled plasma-optical emission spectrometry). Then the iron removal process was carried out using 2.5 M NaOH with a two-step process where the first stage was carried out until the pH of the solution reached 3 and the second stage until the pH of the solution got 3.5. Each of these stages is conducted for 1 hour. Then, the MHP (mixed hydroxide precipitate) precipitation process was carried out for 1 hour with temperature variations of 70, 80, and 90 °C and pH variations of 7, 8, and 9.

The obtained MHP was then dried at 110 °C for 6 hours in an oven. Furthermore, the MHP formed was weighed using a digital balance and analyzed using XRF (x-ray fluorescence) S2 PUMA to determine the elemental composition in the mixtures. XRD (x-ray diffraction) Shimadzu type 7000 analysis was carried out to determine the phases, and SEM (scanning electron microscope) analysis was also conducted to determine the morphology of the nickel hydroxide formed.

3. RESULT AND DISCUSSION

The experiment was conducted using a synthetic mixture of nickel sulfate hexahydrate, cobalt sulfate heptahydrate, and iron (III) sulfate in this study. The solution was created with a Fe, Ni, and Co ratio of 30:20:1. The synthetic PLS (pregnant leaching solution) was created by dissolving 267.86 g of ferric sulfate, 222.74 g of nickel sulfate hexahydrate, and 11.91 g of cobalt sulfate heptahydrate in 5 L of 0.2 M sulfuric acid to yield PLS with iron concentrations of 15 g/L, 10 g/L, and 0.5 g/L, respectively. The conditions for making this synthetic PLS solution adopted the research conducted by Topkaya [12], which carried out multi-step leaching of nickel limonite ore using a leaching agent in the form of sulfuric acid with nickel extraction in the range 85%-89%, cobalt extraction about 57%-71% and iron extraction around 68%-79%. Furthermore, the AAS (atomic absorption spectrometry) instrument first analyzed the PLS to determine the actual concentration of iron, cobalt, and nickel in the process, and the results are listed in Table 1.

Table 1. AAS analysis for synthetic PLS

Element	g/L
Nickel (Ni)	9.488
Cobalt (Co)	0.4937
Iron (Fe)	11.91

The iron removal process was carried out in two stages by adding 2.5 M NaOH at 80 °C and stirring at 450 rpm for 1 hour. In the process of iron removal stage 1; 45 mL of 2.5 M NaOH was added to 200 mL PLS until the pH in the solution was up to 3. The result from the iron removal process stage 1 is that iron could be selectively precipitated in the process. The iron concentration in the PLS after stage 1 could be reduced up to 99.53%, with nickel and cobalt concentration only slightly reduced to 1.265% and 0.546%, respectively. For the process of iron removal stage 2; 15 mL, NaOH 2.5 M was added to the solution to raise the pH to 3.5. The accumulated reduction value of iron concentration in the PLS from stages 1 and 2 is 99.95%, with the concentration of nickel and cobalt only decreasing by 1.311% and 1.357%, respectively. The primary purpose of the iron removal process is to neutralize acid and precipitate iron as much as possible because iron is the impurity with the highest content in PLS.

3.1 Color Change in the Precipitation Process

In the MHP (mixed hydroxide precipitate) precipitation process, several phenomena were observed, such as a color change from light green to transparent, as shown in Fig. 1.

Table 2. Results of ICP-OES analysis of PLS solution after precipitation of MHP

Element	g/L
Nickel (Ni)	0.9234
Cobalt (Co)	0,0006

Figure 1 depicts the color changes experienced by the solution prior to and after the MHP precipitation process. This color change indicates that a lot of nickel and cobalt contained in the PLS

solution have been precipitated so that the solution only had a small amount of nickel and cobalt, as shown in Table 2.

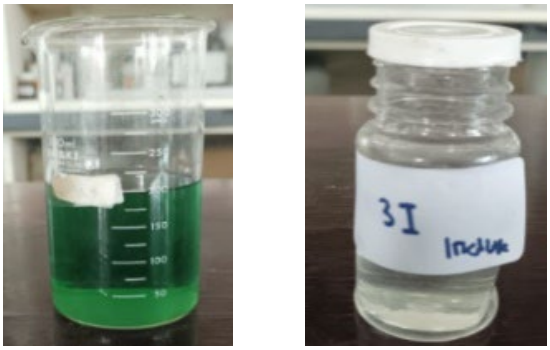

(a) (b)

Figure 1. (a) PLS before MHP precipitation process, (b) PLS after MHP precipitation process

3.2 Precipitation of MHP with Various Temperature

One of the factors that can influence the MHP precipitation process is temperature. Temperature variations were carried out in the MHP precipitation process at 70, 80, and 90 °C with a precipitation time of 3 hours and added NaOH 2.5 M 45 mL, 15 mL, and 5 mL, respectively.

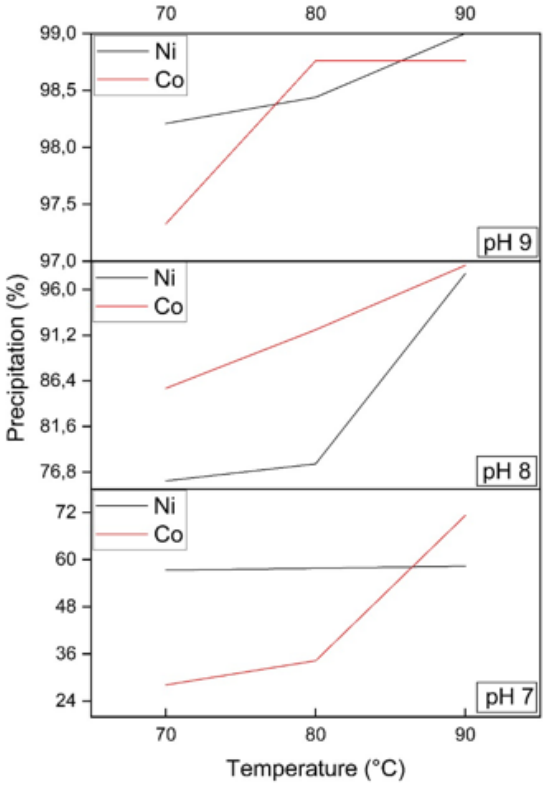

Figure 2. Effect of temperature on element precipitation

The results show that at 70 °C, the lowest nickel and cobalt content precipitated in the MHP was 57.86% and 29.11%, respectively. At 90 °C, the highest value of nickel and cobalt content precipitated was 99.014% and 98.768%, respectively. The relationship between nickel and cobalt content deposited on MHP can be seen in Fig. 2.

Based on Figure 2, it can be seen that the nickel and cobalt deposited in the MHP increased with increasing temperature. The higher the temperature of the precipitation process, the higher the recovery of nickel and cobalt precipitated [12]. The higher the temperature used, the higher the kinetic energy of the molecules of substances in the solution that will react so that the more molecules of substances that have energy more significant than the more signification energy, the more effective collisions occur, which will increase the reaction rate [12]. The higher the reaction rate, the faster the reaction will occur, so more nickel and cobalt will precipitate [11]. Based on the data obtained, it can be seen that temperature influences the MHP precipitation process, with the optimum temperature obtained at 90 °C.

3.3 Precipitation of MHP with Various pH

This research was also carried out with pH variations in the MHP precipitation process.

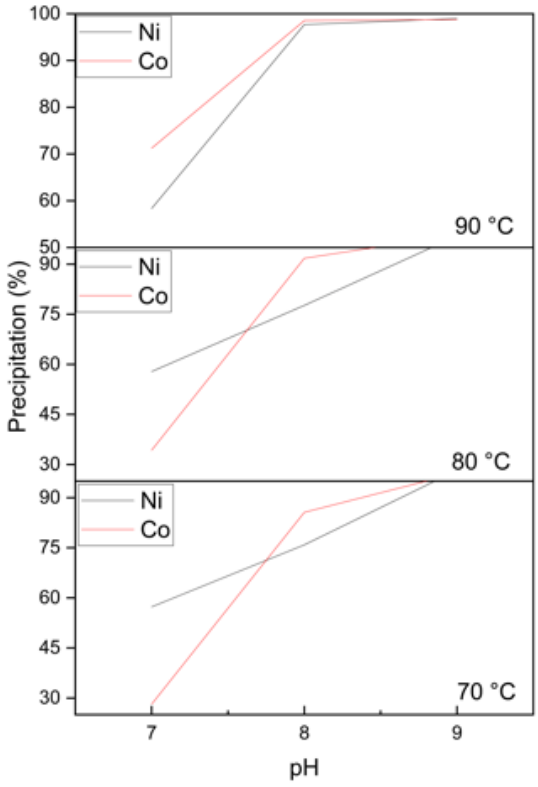

Figure 3. Effect of pH on element precipitation

With a precipitation time of 3 hours, the pH variations used were 7, 8, and 9. According to the research findings, the lowest nickel and cobalt content in the precipitate was obtained at pH 7, 57.86% and 29.10%, respectively. The highest nickel and cobalt concentrations in the precipitate were obtained at pH 9, namely 99.02% and

98.78%, respectively. If the pH variation is plotted against the nickel and cobalt precipitates recovery, a curve is shown in Fig. 3.

Based on Figure 3, it can be seen that the value of nickel and cobalt deposits in MHP increases with increasing pH. The higher the pH used, the higher the recovery of nickel and cobalt deposits; this is to research conducted by Oustadakis et. al., [12] which showed that increasing pH resulted in more significant precipitation of metal hydroxides.

3.4 XRF (X-Ray Fluorescence) Analysis on MHP (Mixed Hidroxide Precipitate)

The result of XRF (x-ray fluorescence) analysis of MHP residues at pH 9 and a temperature of 90 °C can be seen in Table 3. XRF analysis was conducted to determine the levels of nickel and cobalt formed after the MHP precipitation process. The result has a low Fe content because the iron was removed first in the previous processes. These results show that the nickel and cobalt content of the produced MHP is very high, while the iron content is very low. The iron content in the MHP XRF analysis indicates that the iron removal process was successful in removing the majority of the Fe in the solution.

Table 3. XRF Analysis for MHP synthesized a pH of 9 and temperature of 90 °C

Element	Wt.%
Nickel (Ni)	61.467
Cobalt (Co)	1.560
Ferum (Fe)	0.003

3.5 XRD Analysis on MHP (Mixed Hydroxide Precipitate)

MHP compounds were also analyzed using XRD to determine the nickel and cobalt compounds formed after the MHP precipitation process.

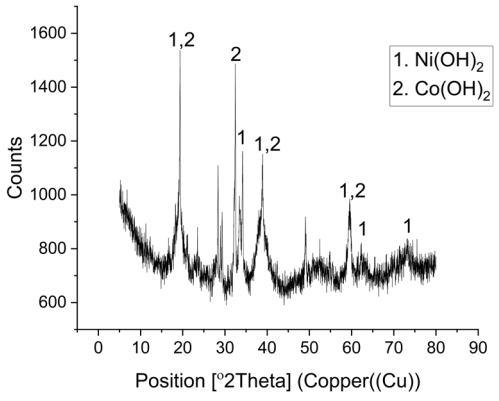

Figure 4. X-ray diffraction pattern for MHP (mixed hydroxide precipitate)

The XRD diffraction pattern was analyzed with the ICSD (inorganic crystal structure database) standard using the HSP (high score plus) software to identify $Ni(OH)_2$ and $Co(OH)_2$ compounds. The tested samples obtained that the comparison image of the X-ray diffraction pattern of the experimental MHP samples had similarities with the x-ray diffraction pattern based on the ICSD No. Standard. 98-002-4015 and ICSD No. 98-008-8940, the diffraction pattern of $Ni(OH)_2$ and $Co(OH)_2$ compounds. The XRD analysis was carried out with the range of 2θ angle of 10°-80°. The sample found typical peaks of Ni(OH)2 at 2θ (°) = 19, 33, 38, 52, 59, 62 and 70 and found peaks of Co(OH)2 at 2θ (°) = 19, 32, 38, 51, 58, 61 and 69. The higher the peak produced, the more compounds formed. Figure 4 shows a comparison image of x-ray diffraction at MHP, the result of precipitation at pH 9, and a temperature of 90 °C.

3.6 SEM (Scanning Electron Microscope) Analysis on $Ni(OH)_2$

The results of the SEM (scanning electron microscope) analysis of the MHP are illustrated in Fig. 5. SEM micrographs show that the formation of nickel hydroxide particles occurs through the aggregation of small particles. The incorporation mechanism of growing nickel hydroxide crystals has also been studied previously by Jones [13]. Elemental mapping in MHP is carried out to determine the compounds in MHP through SEM-EDS (energy dispersive spectrometry) analysis (Fig. 6).

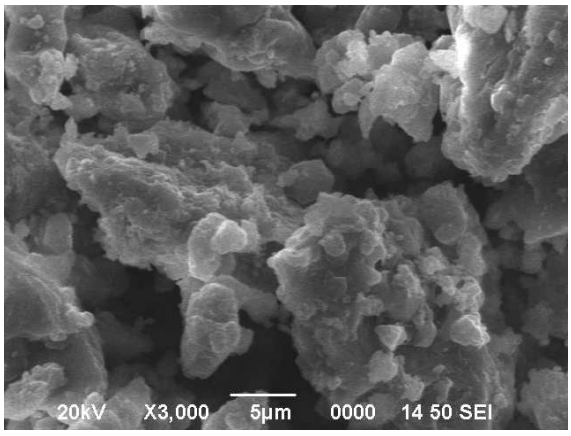

Figure 5. Morphology of $Ni(OH)_2$ at 90 °C temperature and pH 9

Several points on the MHP indicate the presence of sodium as the main impurity in the precipitate. The presence of sodium in the form of sodium ulfate produced by the reaction of sodium hydroxide as a pH regulator and sulfuric acid was also detected and can be seen in Fig. 6.

3.7 Mass of Mixed Hydroxide Precipitate

The nickel and cobalt content precipitated in MHP (mixed hydroxide precipitate) was weighed based on the study results. The highest sediment mass gain was obtained at pH 9 at 90 °C with a precipitate mass of 5.61 grams, while the lowest sediment mass was obtained at pH 7 at 70 °C with a sediment mass of 1.12 grams.

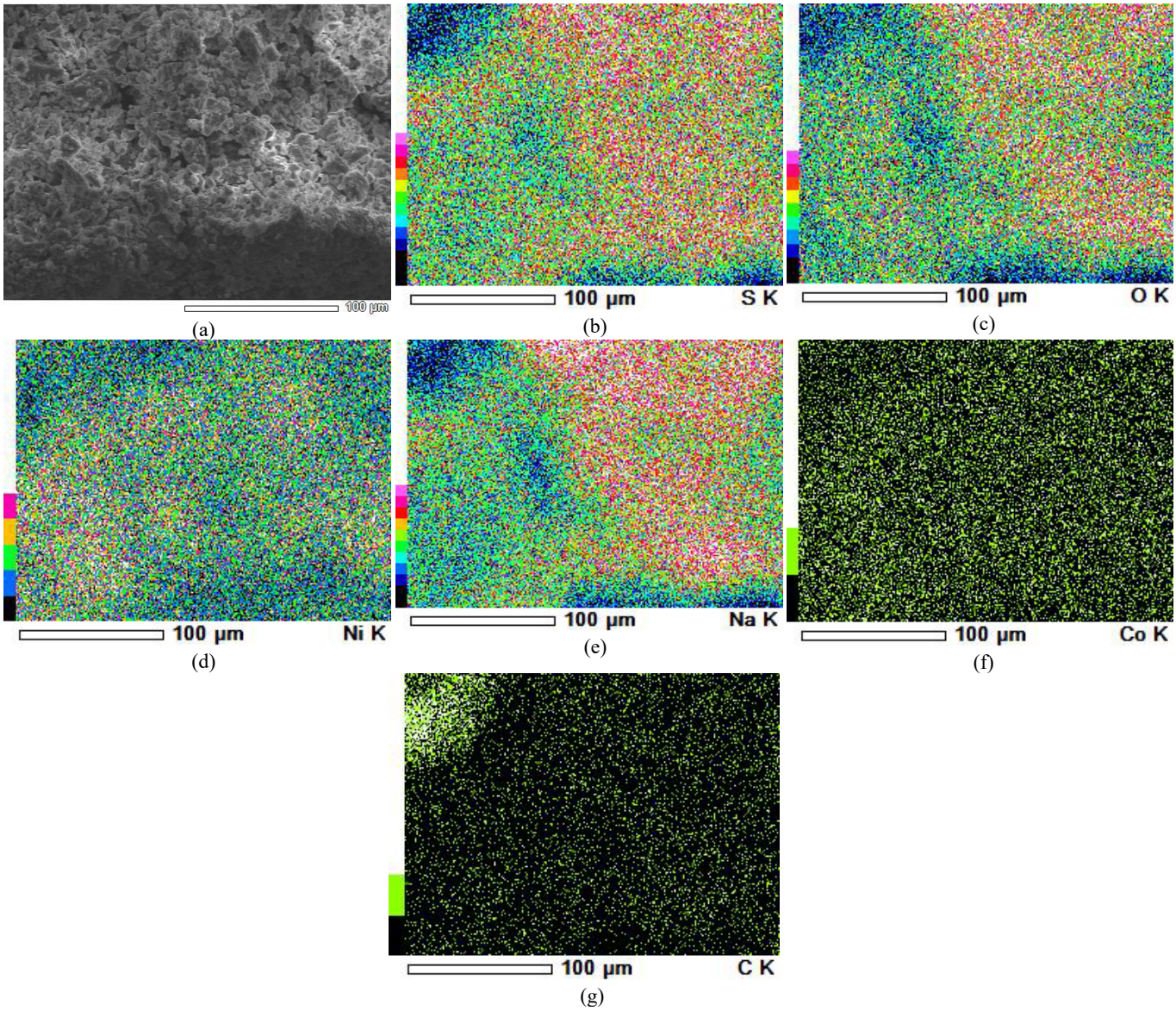

Figure 6. (a) BSE image of MHP at 90 ºC temperature and pH 9 with EDS elemental mapping of (b) Sulphur, (c) Oxygen, (d) Nickel, (e) Natrium, (f) Cobalt, and (g) Carbon

This result shows that the higher the pH and temperature, the higher the MHP precipitate obtained. Nickel content was obtained at optimum conditions, namely pH of 9 and temperature of 90°C, with a nickel content in MHP of 33.49% and cobalt of 1.738%. The results of the MHP mass measurement are then plotted in Fig. 7.

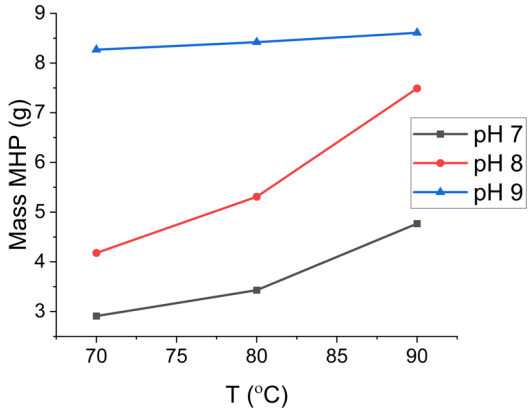

Figure 7. MHP (mixed hydroxide precipitate) mass after Ni/Co precipitation

4. CONCLUSION

This work successfully removed iron from PLS (pregnant leach solution) through two stages of precipitation. The first stage was conducted at pH of 3 and the second stage at pH 3.5. After two stages of precipitation, 99.95% of iron could be removed. The nickel and cobalt which co-precipitated in the iron removal process is only 1.311% and 1.357%, respectively, indicating that the iron removal process is selective.

Nickel and Cobalt then could be precipitated in the form of MHP (mixed hydroxide precipitate) at pH of 9 and 90 °C. The maximum value of nickel and cobalt precipitation yield are 99.03% and 98.78%, respectively. The content of nickel and cobalt in the resulting MHP are 33.49% for nickel and 1.734%, respectively.

ACKNOWLEDGMENT

This work was financially supported by the National Research and Innovation Agency (BRIN). The experiment was carried out at Research Center for Metallurgy, National Research and Innovation Agency (BRIN).

REFERENCES

[1] U.S. Geological Survey, "*Mineral commodity summaries 2021: U.S. Geological Survey*," pp. 200, 2021. Doi: 10.3133/mcs2021.

[2] K. C. Wanta, F. H. Tanujaya, R. F. Susanti, H. T. B. M. Petrus, I. Perdana, and W. Astuti, "Studi kinetika proses atmospheric pressure acid leaching bijih laterit limonit menggunakan larutan asam nitrat konsentrasi rendah," *J. Rekayasa Proses*, vol. 12, no. 2, pp. 19, 2018. Doi: 10.22146/jrekpros.35644.

[3] A. Vahed, P. J. Mackey, and A. E. M. Warner, "*Around the nickel world in eighty days': A virtual tour of world nickel sulphide and laterite operations and technologies*," Ni-Co 2021: The 5th International Symposium on Nickel and Cobalt, pp. 3–39, 2021. Doi: 10.1007/978-3-030-65647-8_1.

[4] T. Gultom and A. Sianipar, "High pressure acid leaching: A newly introduced technology in Indonesia," *IOP Conf. Ser. Earth Environ. Sci.*, vol. 413, no. 1, 2020. Doi: 10.1088/1755-1315/413/1/012015.

[5] B. Willis, "Downstream processing options for nickel laterite heap leach," *Conference: ALTA 2007 Nickel- Cobalt Conference - not published*, pp. 27, 2007.

[6] S. Hussaini, Z. T. Ichlas, S. Top, S. Kursunoglu, and M. Kaya, "Selective leaching of a mixed nickel-cobalt hydroxide precipitate in sulphuric acid solution with potassium permanganate as oxidant," *Sep. Sci. Technol.*, vol. 56, no. 14, pp. 2475-2484, 2021. Doi: 10.1080/01496395.2020.1832523.

[7] Z. T. Ichlas, M. Z. Mubarok, A. Magnalita, J. Vaughan, and A. T. Sugiarto, "Processing mixed nickel-cobalt hydroxide precipitate by sulfuric acid leaching followed by selective oxidative precipitation of cobalt and manganese," *Hydrometallurgy*, vol. 191, pp. 105185, 2020. Doi: 10.1016/j.hydromet.2019.105185.

[8] S. Kurşunoglu, "Extraction of nickel from a mixed nickel-cobalt hydroxide precipitate," *Bilim. Madencilik Derg.*, vol. 58, no. 1, pp. 45-52, 2019. Doi: 10.30797/madencilik.537644.

[9] N. A. Zainuddin, T. A. R. Mamat, H. I. Maarof, S. W. Puasa, and S. R. M. Yatim, "Removal of nickel, zinc and copper from plating process industrial raw effluent via hydroxide precipitation versus sulphide precipitation," *IOP Conf. Ser. Mater. Sci. Eng.*, vol. 551, no. 1, 2019. Doi: 10.1088/1757-899X/551/1/012122.

[10] Z. Niu, G. Li, D. He, X. Fu, W. Sun, and T. Yue, "Resource-recycling and energy-saving innovation for iron removal in

hydrometallurgy: Crystal transformation of ferric hydroxide precipitates by hydrothermal treatment," *J. Hazard. Mater.*, vol. 416, pp. 125972, 2021. Doi: 10.1016/j.jhazmat.2021.125972.

[11] C. H. Köse and Y. A. Topkaya, "Hydrometallurgical processing of nontronite type lateritic nickel ores by MHP process," *Miner. Eng.*, vol. 24, no. 5, pp. 396-415, 2011. Doi: 10.1016/j.mineng.2010.11.010.

[12] P. Oustadakis, S. Agatzini-Leonardou, and P. E. Tsakiridis, "Nickel and cobalt precipitation from sulphate leach liquor using MgO pulp as neutralizing agent," *Miner. Eng.*, vol. 19, no. 11, pp. 1204-1211, 2006. Doi: 10.1016/j.mineng.2005.11.006.

[13] A. N. Jones and N. J. Welham, "Properties of aged mixed nickel-cobalt hydroxide intermediates produced from acid leach solutions and subsequent metal recovery," *Hydrometallurgy*, vol. 103, no. 1-4, pp. 173-179, 2010. Doi: 10.1016/j.hydromet.2010.03.017.

Metalurgi (2022) 3: 119 - 126

METALURGI
Majalah Ilmu dan Teknologi
p-ISSN 0126-3188 | e-ISSN 2443-3926
ejurnalmaterialmetalurgi.lipi.go.id

OPTIMIZATION OF LATERITE ORE GRINDING PROCESS USING BALL MILL WITH RESPONSE SURFACE METHOD

Gyan Prameswara*, Flaviana Yohanala Prista Tyassena, Idi Amin, Husnul Hatimah
Mineral Chemical Engineering, Makassar ATI Polytechnic
Jl. Sunu 220, Kota Makassar, Indonesia 90211
*E-mail: gyan@atim.ac.id

Received: 29-06-2022, Revised: 04-07-2022, Accepted: 31-12-2022

Abstract

This study used a CCD (central composite design) of RSM to determine the dependence and interaction between several operating conditions that affect the grinding process using a ball mill, such as the number of balls, grinding duration, and rotational speed, on particle size at 80% product mass (P80) and mineral liberation (response surface method). The grinding process was carried out in a cylindrical ball mill with a diameter and length of 18.6 cm and 21.5 cm, respectively, as well as a steel ball with a diameter of 2.5 cm and a weight of 100 grams/ball. A sieve aperture of 180-600 microns is used to analyze the particle size distribution. The optimum data for the grinding process was obtained with the smallest response value of P_{80} (513.294 μm). It was known that the number of balls and grinding duration significantly affected the reduction of the P_{80} value in the sample. The model that can describe the influence of process variables on the P_{80} value was obtained with good accuracy. The elemental concentration and the XRD (x-ray diffraction) pattern were used to determine the mineral content of the sample. Minerals with a lower hardness scale are more easily liberated and exposed. The initial material's P80 value was 1560.89 m, while the P80 grinding process was reduced to 513.29 m under optimal conditions.

Keywords: *CCD (central composite design), grinding, RSM (response surface method), laterite, nickel*

1. INTRODUCTION

Nickel is a metal currently attracting concern due to its numerous applications, including its use in battery cathodes. The growth of the EV (electric vehicle) industry sets the stage for the rising use of high-capacity batteries. In response to this demand, the nickel refining process from primary and secondary sources must be carried out. Because saprolite resources are depleted and limonite is abundant, the investigation is primarily focused on nickel laterite discovered in limonite. Indonesia has 1.576 million tons of laterite reserves, the third-largest after New Caledonia and the Philippines [1]-[2]. The topic of the nickel refining process becomes quite intriguing to be addressed as a result of these various concerns. The nickel concentration of limonite ore ranges between 0.8 and 1.5 percent. The low nickel content is also essential when creating an optimum processing method. One of these processes is the use of a ball mill for grinding.

The preliminary laterite processing is critical for the following process stage. The grinding process is the first step in separating liberated minerals from undesired minerals and increasing surface area. Grinding consumes a significant amount of energy in the initial stages of the mineral processing process. The grinding process can consume up to 70% of the energy in a mineral processing plant [3]-[4]. Typically, the grinding step occurs towards the end of the comminution process. A ball mill is a type of grinding machine that uses a combination of impact and abrasion to reduce particle size [5]. The key to successful mineral processing is to create optimal operating conditions.

Considerable research has been conducted to investigate mineral grindability. However, few have investigated the optimization of the grinding process itself, particularly for nickel laterite. Velázquez et. al., [6] investigated the grindability of nickel laterite with various serpentine combinations. Tong et. al., [7] used a stirred mill

DOI : 10.14203/metalurgi.v37i3.655

Metalurgi is Sinta 2 Journal (https://sinta.ristekbrin.go.id/journals/detail?id=3708) accredited by Ministry of Research & Technology, Republic Indonesia

to examine the selective comminution of goethite from saprolite. Petrakis et. al., [8] used the population balance approach to examine the effect of the number of balls on particle size reduction in the ball mill during a selective grinding process on low-grade laterite. Based on the research that has been done, there hasn't been much discussion about optimization with the RSM (response surface method) in the grinding process of laterite ore using a ball mill. The goal of this study is to see how the number of balls, grinding duration, and ball mill rotational speed affect the size of 80 percent of the particles that pass through the grinding process (P_{80}). The particle distribution before and after milling was investigated using a sieve shaker with an aperture size range of 180-600 m.

2. MATERIALS AND METHODS

2.1 Mineral Characterization

The laterite ore utilized in the research was obtained from Morowali, Central Sulawesi. Elemental analysis was carried out using an XRF (x-ray fluorescence) Rigaku Primini Benchtop with a 5-minute scan duration. Table 1 shows the findings of the analysis.

Mineral phase analysis was also performed using an XRD (x-ray diffraction) SmartLab using Cu-Kα radiation in the 2θ range of 3-90°.

Table 1. The elemental concentration of laterite ore (wt.%)

Ni	Co	Si	Al	Fe	Ca
1.90	0.16	9.36	2.22	13.82	0.44
Mg	**Li**	**LOI***			
5.13	0.82	0.81			

**Lost on Ignition.*

The P_{80} value of the initial sample is 1560.89 µm. P_{80} value indicates 80% of the total particles have a size of 1560.89 µm.

2.2 Grinding Process Using Ball mill

A lifter-equipped cylindrical ball mill with a diameter of 18.6 cm and a length of 21.5 cm is used for grinding. The ball mill is powered by a motor connected to a belt. The number of balls (5-15), the duration of the grinding (5-15 minutes), and the rotation speed of the ball mill were the experiment's independent variables (8-16 rpm). The mass and diameter of each steel ball used in this study are shown in Table 2. Each experiment required 200 grams of each sample.

Table 2. Steel ball characteristic

Balls	Mass (g)	Diameter (cm)
1	80.053	2.35
2	89.542	2.78
3	89.626	2.79
4	91.752	2.80
5	91.957	2.81
6	92.254	2.81
7	92.553	2.82
8	92.607	2.82
9	92.667	2.82
10	92.701	2.83
11	93.554	2.85
12	93.853	2.86
13	93.860	2.86
14	93.860	2.86
15	93.874	2.87
Total	1374.713	
Average	91.647	2.82

Following the grinding process, a sieve with a aperture size range of 180-600 µm was performed using the Ristech Test Sieve (ASTM E 11-09). The mean diameter of solid particles was correlated with the average aperture size of each sieve. The mass fraction (percent) and cumulative mass passed are calculated using the mass of particles measured in each sieve (percent).

Table 3. Feed sample particle distribution

Aperture (µm)	Average aperture size (µm)	Retained mass (gram)	% mass (%)	Cummulative oversize (%)	Cummulative undersize (%)
+600	600.000	340.000	73.325	73.325	26.675
+500-600	550.000	16.585	3.577	76.902	23.098
+425-500	462.500	13.642	2.942	79.844	20.156
+355-425	390.000	11.179	2.411	82.255	17.745
+212-355	283.500	35.469	7.649	89.904	10.096
+180-212	196.000	10.953	2.362	92.266	7.734
-180	180.000	35.861	7.734	100.000	0.000
total		463.689	100.000		

2.3 Design of Experiment and Statistical Analysis

CCD (central composite design) was used. The Minitab 19 software is also used for data processing. This method determined the effect of independent variables (number of balls, grinding duration, and rotational speed) on the particle size value of 80% of the total particles (P_{80}). CCD employs 2n (n=3) factorial experiments, 2n axial experiments, and nc center experiments. The goal of this experiment is to identify the optimal operating conditions for the grinding of laterite ore. The model uses a second-order polynomial to correlate the response (P_{80}) to the

three independent variables, as shown in equation (1).

$$Y = b_0 + \sum_{i=1}^{n} b_i x_i + \sum_{i=1}^{n} b_{ii} x_i^2 + \sum_{i=1}^{n-1} \sum_{j=i+1}^{n} b_{ij} x_i x_j \quad (1)$$

Where Y is the response (P_{80}), b_0 is the constant coefficient, b_i is the linear coefficient, b_{ij} is the interaction coefficient, b_{ii} is the quadratic coefficient, and x_i, x_j are independent variables. Table 4 shows the grinding process level used in this experiment.

Table 4. Variable level of grinding process

Variables	Label	Unit	Level		
			-1	0	1
Number of balls	A	-	5	10	15
Grinding duration	B	minutes	5	10	15
Rotating speed	C	rpm	8	12	16

3. Result and Discussion

3.1 Mineral Characterization

Table 1 presents the concentration of each feed component. The nickel concentration in the feed was 1.9 percent, with Fe of 13.82 percent being the highest concentration in the laterite ore. Undesired elements such as Si, Mg, and Al were present at 9.36; 5.13; and 2.22 percent, respectively.

The mineral phase in the feed material is characterized via an XRD (x-ray diffraction) pattern (Fig. 1).

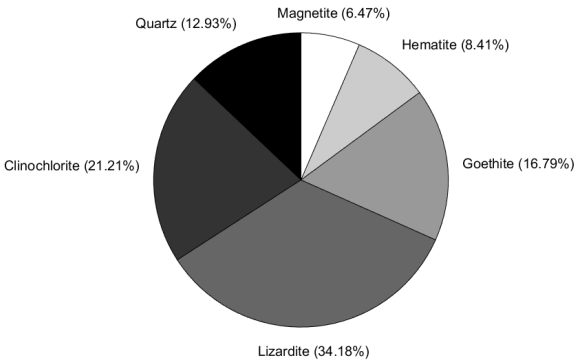

Figure 1. The mineral phase in the laterite ore

The material's XRD pattern analysis indicated that the most prominent phases were lizardite, clinochlore, goethite, and quartz, with hematite and magnetite appearing in minor amounts.

3.2 Particle Size Distribution

Particle distribution analysis on the sieve was performed by obtaining retained mass data on each sieve. A wide range of aperture sizes ranged from 180 to 600 µm. The feed material and the grinding product from a ball mill were used to investigate the influence of the number of balls and residence time on the particle size distribution of laterite ore. The frequency distribution of the feed material is more frequent and homogenous at particle diameter sizes greater than 600 µm, as seen in Figs. 2-4.

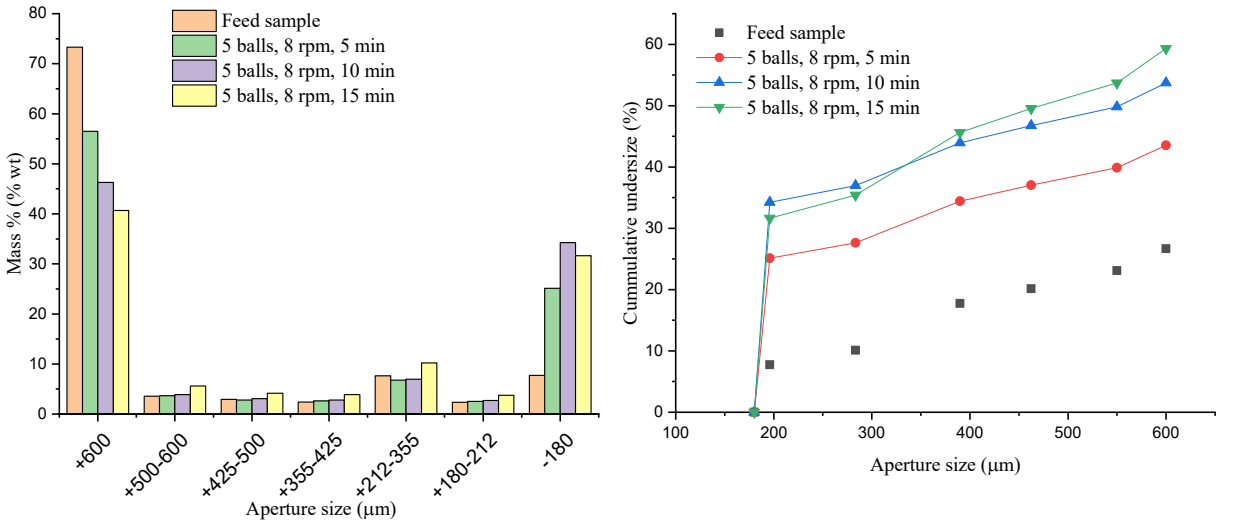

Figure 2. Particle size distribution with 5 balls and cumulative undersize

The higher the number of balls used, the more particles grind to smaller particle sizes. The diameter of laterite ore particles was uniform at sizes smaller than 180 µm at maximum operating conditions (15 balls, 15 minutes, and 8 rpm). Meanwhile, the grinding process with many balls and a short duration produces a bimodal particle distribution pattern (which has two peaks).

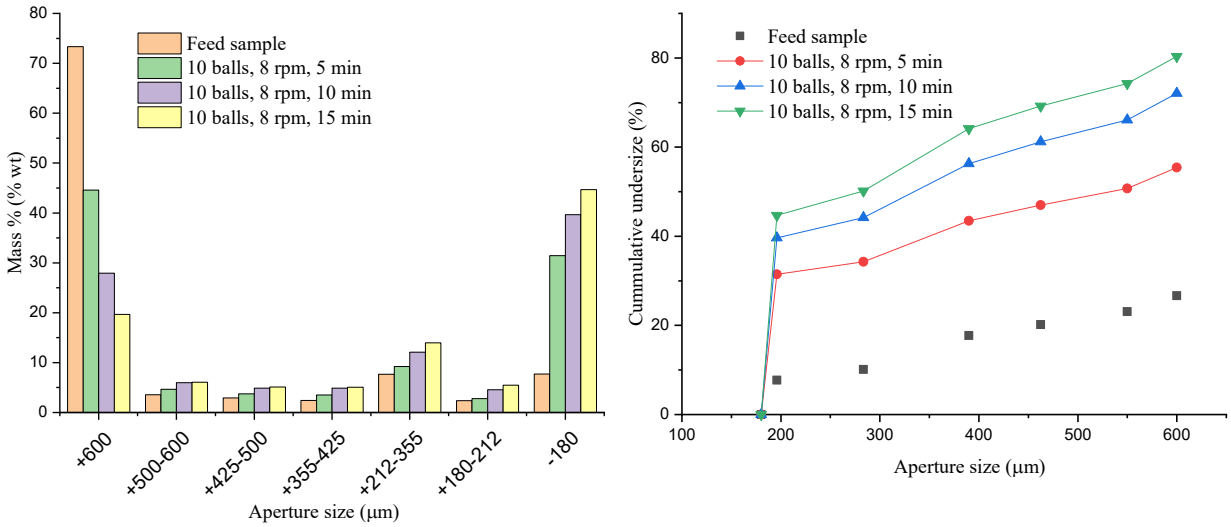

Figure 3. Particle size distribution with 10 balls and cumulative undersize

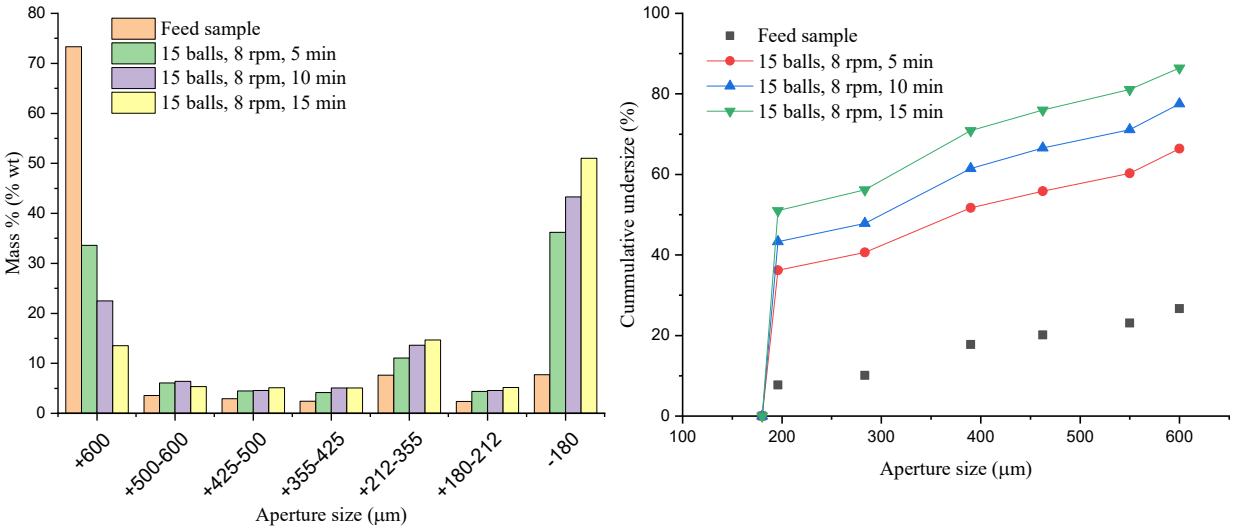

Figure 4. Particle size distribution with 15 balls and cumulative undersize

3.3 Grinding Process Optimization Using the RSM Approach

Data from three levels of the CCD (central composite design) were analyzed to find the best model to represent the relationship between the three independent variables (number of balls, grinding duration, and rotating speed) and the response (P_{80}). Table 5 shows the actual P_{80} observed in the experiment and the predicted P_{80} from the model.

A quadratic model was developed to describe the relationship between the operating conditions and the obtained P_{80}. As seen in equation (2), the model is a polynomial of order 2:

$$Y = 1810 - 102.8A - 59{,}2B - 11{,}5C + 2{,}48A^2 + 0{,}31B^2 - 2{,}04C^2 + 0{,}683AB + 1{,}849AC + 2{,}698BC \quad (2)$$

Where Y represents the P_{80} value (µm), A represents the number of balls, B represents the grinding duration (minutes), and C represents the rotating speed (rpm). The obtained model has an excellent correlation coefficient (R^2 = 0.9769), which describes the model utilized quite well.

Table 5 shows the sum of squares and mean squares for each factor and the F-value and P-value. F-value describes the distribution of the mean of the test sample or the mean square divided by the error. While the P-value shows the significance of the test variable (P-value < 5%).

In addition, analysis of variance (ANOVA) was used to explain the model obtained, as shown in Table 6. It is clear that factors A, B, C, AC, and BC are significant in this experiment. However, factors A^2, B^2, C^2, and AB are not.

Table 5. Comparison of the experimental P_{80} value and predictions from the obtained model

Number of balls	Time (min)	Rotating speed (rpm)	P_{80} (µm)	
			Experiment	Prediction
15	5	16	545.072	545.548
5	5	16	723.489	746.229
5	15	16	687.492	681.624
15	15	16	532.864	549.260
15	5	8	688.908	698.712
5	5	8	1059.760	1047.30
5	15	8	771.299	766.887
15	15	8	513.294	486.618
10	5	12	734.766	729.950
10	15	12	571.040	591.600
10	10	16	594.558	560.814
10	10	8	630.540	680.028
10	5	8	826.643	810.899
10	10	12	660.804	653.030
10	10	12	661.000	653.030

The smaller the P-Value, the greater the significance of the variable to the change in response. According to previous studies, the significance value is found in factors with a P-value of ≤ 0.05 [9]-[12].

Table 6. Analysis of variance (ANOVA)

Source	DF	Sum of squares	Mean square	F-Value	P-Value
Model	9	262869	29208	23.52	0.0014
A	1	115657	115657	93.14	0.0002
B	1	49608	49608	39.95	0.0015
C	1	36834	36834	29.66	0.0028
A^2	1	4655	4655	3.75	0.1106
B^2	1	93	93	0.07	0.795
C^2	1	1646	1646	1.33	0.3017
AB	1	2334	2334	1.88	0.2287
AC	1	10938	10938	8.81	0.0312
BC	1	24364	24364	19.62	0.0068
Error	5	6209	1242		
Lack-of-Fit	4	6208	1552	80897.9	0.026
Pure Error	1	0	0		
Total	14	269077			

A=Number of ball, B=grinding time (min), C=Rotating speed (rpm)

Figure 5 depicts the effect of the number of balls, grinding duration, and rotating speed on the P_{80} value. In comparison, the feed material's P_{80} value is 1560.89 µm. It can be seen that the number of balls and the grinding time significantly impact the value of P_{80}. The larger

This is due to the grinding process using the dry method so that the ore will quickly move in the direction of the ball being lifted by the lifters. As a result, the probability of a collision between the ball and the laterite ore is reduced. Previous research has found similar results [5], [13]-[15].

This investigation obtained the optimum process conditions for the grinding of laterite ore in a ball mill. The optimum processing conditions are 15 balls, 15 minutes of grinding time, and an 8 rpm rotational speed (Figs. 5(a)-(c)).

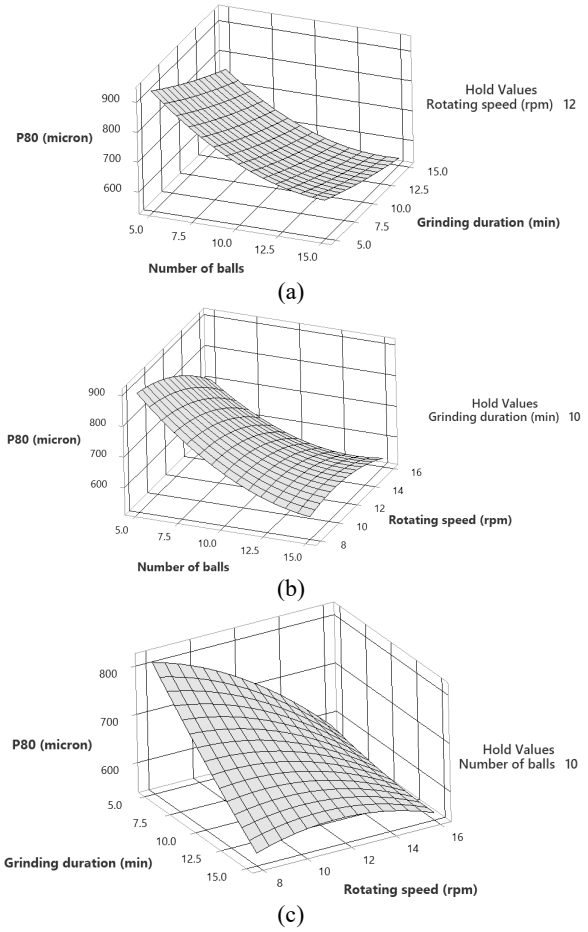

Figure 5. The effect of (a) number of balls and grinding duration, (b) number of balls and rotating speed, and (c) grinding duration and rotating speed on the P_{80} value

Figures 6 and 7 show component concentrations at optimum conditions as well as a comparison of feed material XRD patterns at optimum conditions. The decrease in P_{80} potentially indicates mineral liberation in the laterite material and an increase in the material's surface area. The P_{80} value obtained at the optimum grinding conditions was 51.29 µm.

Minerals with high hardness, such as quartz, are detected less than the feed material. This is

because the harder the mineral is to release, the stronger the bonds between the minerals.

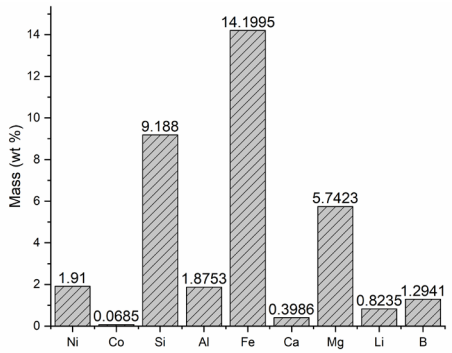

Figure 6. Elemental concentration of grinding product at optimum operating conditions

The hardness scale values of each mineral identified in laterite ore Morowali are shown in Table 7 [13]-[14].

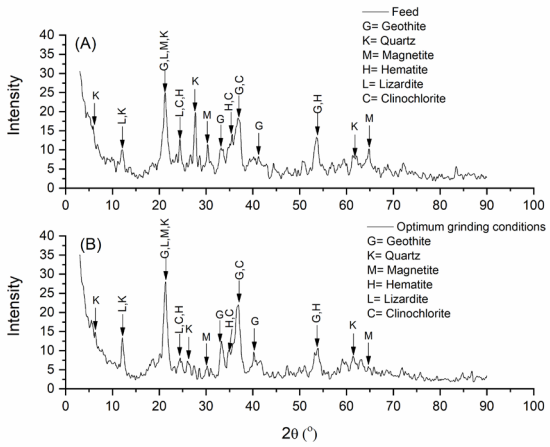

Figure 7. XRD pattern of laterite ore grinding products at optimum operating conditions

The hardness data for each of these minerals shows that the lowest to highest hardness scale values are clinochlore, lizardite, goethite, magnetite, hematite, and quartz, respectively.

Table 7. The hardness scale (Mohs's scale) of the mineral in the laterite ore Morowali

Minerals	Mohs's Hardness	Wt.%
Quartz	7	12.93
Clinochlore	2.5	21.21
Lizardite	2.5	34.18
Goethite	3.8	16.79
Hematite	6.5	8.41
Magnetite	5.75	6.47

Lizardite was the most dominant phase in the sample, accounting for 34.18 percent of the total.

4. CONCLUSION

Initial characterization data and grinding process optimization for Morowali laterite ore have been obtained. In the Morowali laterite ore, it is evident that there are nickel carrier minerals such as goethite, which contain 1.9% nickel. The most common minerals are lizardite, clinochlore, goethite, and quartz. In contrast, hematite and magnetite are only present in trace concentrations.

The size distribution of laterite ore in grinding products has a bimodal distribution. The response surface method was used to optimize the grinding process by determining the correlation between process conditions and the P_{80} value and determining the optimum grinding conditions. This optimization method applies CCD (central composite design). The analytical results show that statistical methods can assist in determining the optimum point of the laterite ore grinding process. The optimal grinding conditions were obtained using 15 balls, 15 minutes of grinding time, and 8 minutes of rotation speed. The material's P_{80} value was decreased from 1560.89 µm to 513.29 µm under these conditions. This is considered useful information for the Indonesian laterite mineral processing industry.

ACKNOWLEDGMENT

The authors would like to thank Makassar ATI Polytechnic for funding the study.

REFERENCES

[1] Kementerian Energi dan Sumber Daya Mineral, *Indonesian Minerals Year Book 2018*. Jakarta: Kementerian Energi dan Sumber Daya Mineral, 2018. Accessed: Nov. 12, 2021. [Online]. Available: https://geologi.esdm.go.id/assets/media/content/content-indonesian-minerals-yearbook-2018.pdf.

[2] S. Stopic and B. Friedrich, "Hydrometallurgical processing of nickel lateritic ores," *Vojnotehnicki glasnik*, vol. 64, no. 4, pp. 1033-1047, 2016. Doi: 10.5937/vojtehg64-10592.

[3] E. Petrakis and K. Komnitsas, "Improved modeling of the grinding process through the combined use of matrix and population balance models," *Minerals*, vol. 7, no. 5, pp. 67-84, 2017. Doi.org/10.3390/min7050067.

[4] J. V. Nava, T. Llorens, and J. M. Menéndez-Aguado, "Kinetics of dry-batch grinding in a laboratory-scale ball mill of Sn-Ta-Nb minerals from the Penouta mine (Spain)," *Metals*, vol. 10, no. 12, pp. 1687-1706, 2020. Doi.org/10.3390/met10121687.

[5] R. Zhao, Y. Han, M. He, and Y. Li, "Grinding kinetics of quartz and chlorite

in wet ball milling," *Powder Technology*, vol. 305, pp. 418-425, 2017. Doi: 10.1016/j.powtec.2016.07.050.

[6] H.-I. Yoo, "Diffusion in continuum," in *Lectures on Kinetic Processes in Materials*, Cham: Springer International Publishing, pp. 1-16, 2020. Doi: 10.1007/978-3-030-25950-1.

[7] L. Tong, B. Klein, M. Zanin, K. Quast, W. Skinner, J. Addai-Mensah, and D. J. Robinson, "Stirred milling of nickel laterites for selective comminution," in *SAG Conference*, pp. 1-20, 2015. Doi: 10.1007/978-3-030-25950-1.

[8] E. Petrakis, V. Karmali, and K. Komnitsas, "Factors affecting nickel upgrade during selective grinding of low-grade limonitic laterites," *Mineral Processing and Extractive Metallurgy*, vol. 130, no. 3, pp. 192-201, 2018. Doi: 10.1080/25726641.2018.1521578.

[9] I. Ani, J. Okafor, M. Olutoye, and U. Akpan, "Optimization of base oil regeneration from spent engine oil via solvent extraction," *Advances in Research*, vol. 4, no. 6, pp. 403-411, 2015. Doi: 10.9734/air/2015/16795.

[10] Z. N. Garba, I. Bello, A. Galadima, and A. Y. Lawal, "Optimization of adsorption conditions using central composite design for the removal of copper (II) and lead (II) by defatted papaya seed," *Karbala International Journal of Modern Science*, vol. 2, no. 1, pp. 20-28, 2016. Doi: 10.9734/air/2015/16795.

[11] E. Sasikumar and T. Viruthagiri, "Optimization of process conditions using response surface methodology (RSM) for ethanol production from pretreated sugarcane bagasse: kinetics and modeling," *BioEnergy Research*, vol. 1, no. 3-4, pp. 239-247, 2008. Doi: 10.9734/air/2015/16795.

[12] J. Bayuo, M. A. Abukari, and K. B. Pelig-Ba, "Optimization using central composite design (CCD) of response surface methodology (RSM) for biosorption of hexavalent chromium from aqueous media," *Applied Water Science*, vol. 10, no. 6, pp. 135-147, 2020. Doi: 10.9734/air/2015/16795.

[13] C. S. Sridhar, P. S. Sankar, and R. K. Prasad, "Grinding kinetics, modeling, and subsieve morphology of ball mill grinding for cement industry ingredients," *Particulate Science and Technology*, vol. 34, no. 1, pp. 1-8, 2016. Doi: 10.9734/air/2015/16795.

[14] T. S. Yusupov, E. A. Kirillova, and L. G. Shumskaya, "Mineral hardness effect on the combined mineral grinding," *Journal of Mining Science*, vol. 43, no. 4, pp. 450-454, 2007. Doi: 10.1007/s10913-007-0046-y.

[15] T. P. Olejnik, "Selected mineral materials grinding rate and its effect on product granulometric composition," *Physicochemical Problems of Mineral Processing*, vol. 49, no. 2, pp. 407-418, 2013. Doi: 10.5277/ppmp130203.

Metalurgi (2022) 3: 127 - 138

METALURGI
Majalah Ilmu dan Teknologi
p-ISSN 0126-3188 | e-ISSN 2443-3926
ejurnalmaterialmetalurgi.lipi.go.id

STRUCTURE, MECHANICAL PROPERTIES, AND OXIDATION RESISTANCE OF Mn-RICH Fe-Mn-Al ALLOYS

Resetiana Dwi Desiati, Edi Sutiawan, Toto Sudiro, Bambang Hermanto*
Research Center for Advanced Materials, National Research and Innovation Agency
B.J. Habibie Sains and Technology Area, Banten, Indonesia 15314
*E-mail: bamb045@brin.go.id

Received: 26-07-2022, Revised: 25-10-2022, Accepted: 31-12-2022

Abstract

In this study, Mn-rich Fe-Mn-Al alloys with different Al content (Al = 0, 3, and 5 % by weight) were fabricated from ferromanganese lumps using a conventional powder metallurgy technique. The samples were compacted in 1 cm steel dies using a load of 8 tons and then sintered at 1100 ℃ for 2 h in a tubular furnace under a vacuum condition of around 0.5 mbar. To evaluate the effect of Al addition to Fe-Mn-Al alloy, the Archimedes principle and Vickers hardness were applied to estimate the density and hardness of the compact alloys. Moreover, the high-temperature oxidation resistance of the alloy was evaluated at 800 ℃ for 8 cycles. The structure of the alloy before and after oxidation was studied using XRD (x-ray diffractometer) and SEM-EDS (scanning electron microscope-energy dispersive spectrometry). The XRD analysis results show that the FeMn-0Al alloy is mainly composed Fe_3Mn_7 phase, with the presence of FeAl phase at 3 wt.% Al, and Al_8Mn_5 phase at 5 wt.% Al. The density and hardness of Fe-Mn-Al alloys decreased with the increased Al content. Fe-Mn-Al alloy without Al addition exhibits poor oxidation resistance since the first cycle of the test. The results of the microstructural analysis showed that although the alloy with the addition of 3 wt.% Al showed less mass gain after being exposed for 8 cycles at 800 ℃, the Fe-Mn-Al alloy with 5 wt.% tended to be more resistant to oxidation and had no cracking defects. The structure of the oxide formed on the surface of the alloy is composed of two layers (ie; outer and inner layer) which are affected by each alloy composition.

Keywords: *Fe-Mn-Al alloy, conventional powder metallurgy, density, hardness, oxidation*

1. INTRODUCTION

The selection of alloy composition to produce high-temperature resistant steels needs to consider the combination between mechanical properties and oxidation/corrosion resistance. Fe-Ni-Cr alloy is known to have these properties [1]-[3]. However, Ni and Cr are expensive elements, so an alternative material element is needed to replace them [2]-[4].

Previously, manganese was thought to be a key element in influencing steel microstructure, mechanical, and oxidation resistance properties [2]-[5]. It is well known that Mn is an austenite stabilizer [4], [6]. Several studies [2]-[3], [5]-[7] investigated and discussed the structure and properties of Fe-Mn steel with manganese concentrations ranging from 10% to 50% by weight . Although FeMn-based alloys have been studied [5], [8], they still have potential due to the alloy system's good properties. Because of their exceptional mechanical properties, FeMn-based alloys have been used in a variety of applications, including Hadfield steel, TWIP (twinning induced plasticity) steel [6]-[7], SMA (shape memory alloy) [9], HEA (high entropy alloy), and others [10].

The addition of alloying elements such as Al was also considered to improve the mechanical properties and the resistance of steel against oxidation at high temperatures. It is well known that Al has a high affinity for oxygen [11]-[12] and played a role in oxidation resistance, which can form a protective layer of Al-oxides and some spinels that can protect against exposure to high temperatures [11], [13]-[14]. Besides Al, Mn has also a great affinity with oxygen [8], [15], and they can react with each other to form stable oxides.

DOI : 10.14203/metalurgi.v37i3.660

Metalurgi is Sinta 2 Journal (https://sinta.ristekbrin.go.id/journals/detail?id=3708) accredited by Ministry of Research & Technology, Republic Indonesia

Over the past decades, ferromanganese lump as a source of Mn alloying elements is one of the important materials for steel production. Its name is based on the major element content in ferrolump material. This material is mostly divided into three categories: low (<0.5 wt.%), medium (<2.5 wt.%), and high (~7.0 wt.%) C content [16]. Ferro lump material has the potential to be developed because it is much cheaper than high purity metal powder which is more expensive. In this study, we used ferromanganese lumps to synthesize Mn-rich iron-manganese alloys by considering the addition of Al to determine their microstructure, mechanical properties, and oxidation resistance.

The current study focuses on the structure, hardness, and oxidation properties of Mn-rich Fe-Mn-Al alloys. Furthermore, the effect of Al content of up to 5% in weight on the aforementioned properties was thoroughly clarified and discussed.

2. MATERIALS AND METHODS

2.1 Sample Preparation

Ferromanganese lump with a chemical composition as shown in Table 1 was used in this study.

Tabel 1. Chemical composition of ferromanganese (wt.%)

Element	Wt.%
Fe	19.87
Mn	78
C	1.45
Si	0.5
P	0.15
S	0.03
Total	100

Several Fe-Mn-Al alloys with varying Al content (0, 3, and 5 wt.%) are shown in Table 2.

Tabel 2. Chemical composition of Fe-Mn-Al alloys (wt.%)

Element	FeMn-0Al	FeMn-3Al	FeMn-5Al
Fe	19.87	19.27	18.88
Mn	78	75.66	74.10
C	1.45	1.41	1.38
Si	0.5	0.485	0.475
P	0.15	0.15	0.14
S	0.03	0.029	0.029
Al	0	3	5

Al powder was used from MTIKorea with a purity of 99.9%.

(a) (b) (c)

Figure 1. Starting material: (a) ferromanganese lump, (b) ferromanganese powder, and (c) aluminium powder

Firstly, the lump material (Fig. 1(a)) was crushed into powder (Fig. 1(b)) using a steel mortar and shaker mill. Subsequently, the ferromanganese powder was mixed and mechanically alloyed with different content of Al (Fig. 1(c)) as 0; 3; and 5 wt.% to obtain a uniformly mixed powder. The powder mixing was performed under wet milling condition for 2 h to avoid the powder oxidation. After that, the powder was dried in desicator.

Figure 2 shows the XRD (x-ray diffraction) spectrum of the ferromanganese and Al as the starting material. The diffraction pattern shows that ferromanganese powder is composed of Mn, $FeMn_3$, $Mn_{23}C_6$, and $Fe_{0.3}Mn_{2.7}C$ phases. While Al powder was detected by Al phase, indicating no contaminants and impurities in the powder. For the green body specimen fabrication, 2 grams of the powder was placed in steel dies with a diameter of 1 cm. The powders were uniaxially pressed using 8 tons in load for 3 min. The green body was then released from the dies and subsequently sintered at 1100 °C for 2 h in a tubular vacuum furnace under 0.5 mbar.

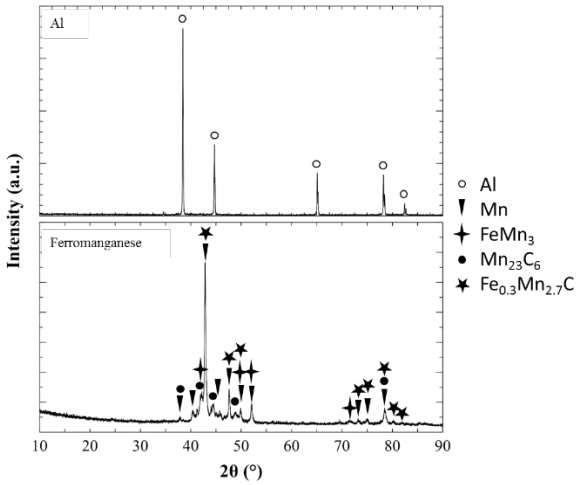

Figure 2. XRD patterns of ferromanganese and Al powder as starting material

All samples in this study were prepared using the same fabrication parameters. Following sintering, the sample's surface was mechanically polished with various grit SiC papers and DP-nap polishing for up to mirror-finish before being ultrasonically cleaned in ethanol solution. Finally, hot blowing air was used to dry the samples.

2.2 Testing and Characterization

The density and hardness of the alloys were measured using the Archimedes principle and Vickers hardness tester (LECO LM-100), respectively. The sample indentation was carried out using 300 gf for 13 s. In order to evaluate the effect of Al addition on oxidation resistance, the sample was thermally direct exposed to the

atmosphere of a muffle furnace at 800 °C. The samples were soaked in the furnace at 800 °C for 20 h/cycling and rapidly cooling at ambient temperature for 4 h. This process was repeated for 8 times. The mass gain per specific area of the sample was recorded temporarily using an electronic balance KERN ABT 220-5DM (accuracy = 0.01 mg) in order to evaluate the kinetic oxidation resistance. The crystal structure, microstructure, and element distribution/chemical analysis of Fe-Mn-Al alloys before and after high-temperature oxidation test were observed by using XRD Rigaku Smartlab with CuKα1 radiation (λ=0.15405), SEM (scanning electron microscope) Hitachi SU3500 and EDS (energy dispersive spectrometry) Horiba.

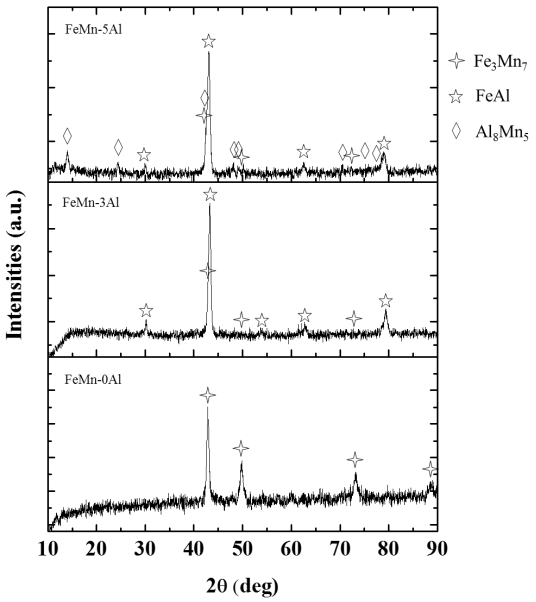

Figure 3. X-ray diffraction patterns of Fe-Mn-Al alloys with different content of Al

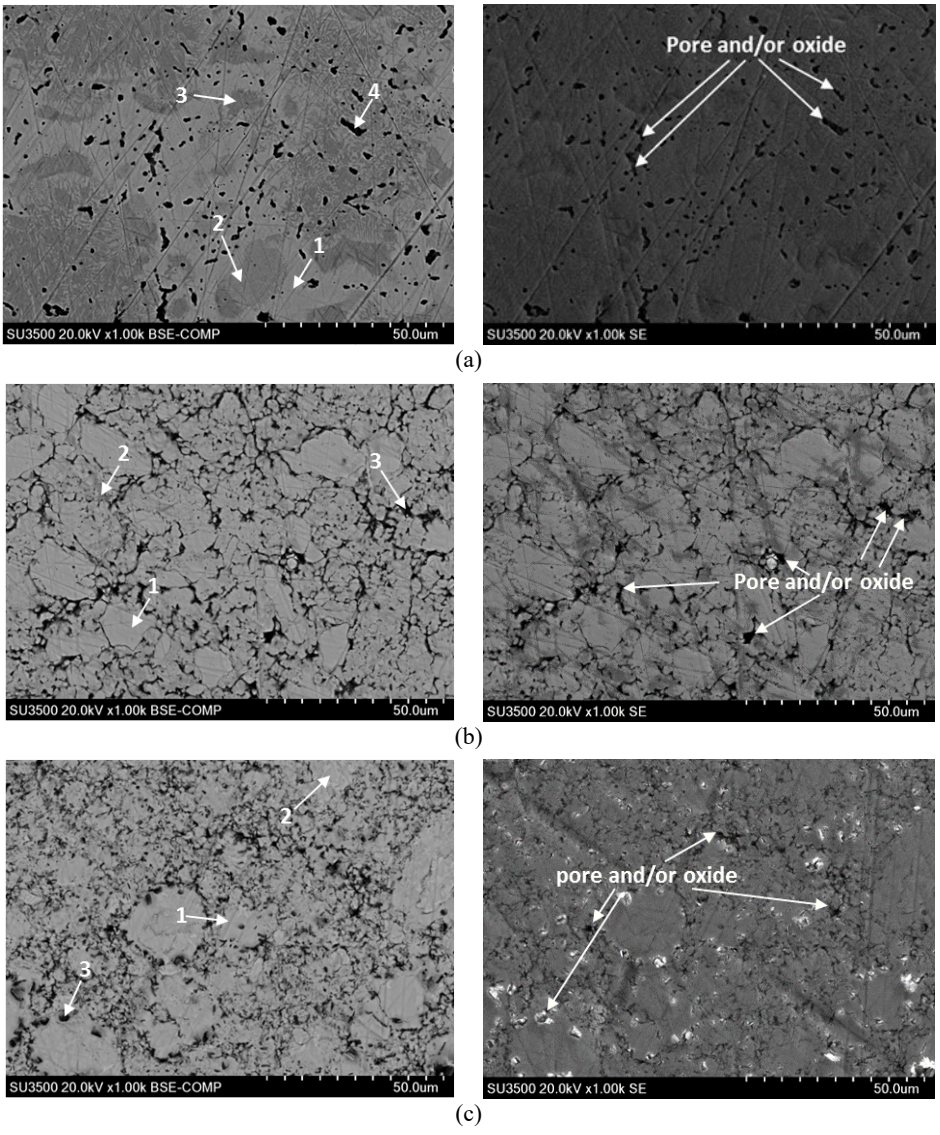

Figure 4. BSE-SE SEM surface morphologies and EDS corresponding location of Fe-Mn-Al alloys with (a) 0, (b) 3, and (c) 5 wt.% Al content

3. RESULT AND DISCUSSION

3.1 Phase Composition and Microstructure

Figure 3 shows the x-ray diffraction patterns of polished surface of Fe-Mn-Al alloys prepared by a conventional powder metallurgy technique which is vacuum sintered at 1100 °C for 2 h. As in Fig. 3, the main constituent of FeMn-0Al alloy detected by x-ray diffraction is Fe_3Mn_7 phase. Some of the diffraction peaks were not clearly visible with the addition of Al. The presence of carbides type structure is also not clearly reflected although high carbon content. It may the carbide in the same diffraction with the main detected phase, as a secondary phase of the matrix, or a mixture of phases [4]. Since carbide particles seem to be present in a small domain, the bulk technique detection by XRD may be difficult because of an overlapping peak at around 43° which makes it difficult to distinguish [17]. By addition of 3 wt.% Al, new phase was detected as FeAl. The diffraction peaks of Fe_3Mn_7 phase tends to decrease. Furthermore, with the addition of 5 wt.% of Al content, FeAl and small intensities of Fe_3Mn_7 were still detected with the appearance of a new phase of Al_8Mn_5.

Rashidi et. al., [4] reported that the manganese triggers the formation of carbides, the higher Mn will increase the concentration of carbide. In this study, an increasing the Al content will reduce the Mn content so that the carbide also tends to decrease.

The SEM (scanning electron microscope) images (BSE (backscattered electron) and SE (secondary electron)) and the corresponding location of EDS (energy dispersive spectrometry) point analysis carried out on the Fe-Mn-Al alloys sintered at 1100 °C for 2 h were shown in Fig. 4. The morphological analysis showed that the FeMn-0Al alloy had a denser and more homogeneous microstructure than the alloy with the addition of 3 and 5 wt.% of Al. Irregular black precipitates were found in Fe-Mn-Al alloys and its presence tend to increase with the addition of Al. This structure may affect the properties of alloys.

The results of BSE micrograph show that the FeMn-0Al alloy consists of three distinguished area (see Fig. 4(a)): bright (Point 1), grey (Point 2 and 3), and black areas (Point 4). Differ with Al-free alloy, the typical microstructure of 3 wt% and 5 wt% Al alloys as shown in Fig. 4(b) and 4(c) is composed of two areas mainly: grey (Point 1) and black area (Point 3). During the milling process with a shaker mill there is a collision between the ferromanganese material, steel ball, and vial. These may result an erosion from steel ball and vial that seem to be impurities. Although, due to the fact that the main element of milling balls and vial are Fe, and the ferromanganese also contains Fe. So, if there is erosion from milling balls and vials, they do not become a significant contaminant. To investigate the chemical composition of sintered Fe-Mn-Al alloys, we performed an EDS point analysis in the corresponding area of Fig. 4 and the results are listed in Table 3.

Differences in color or contrast in microstructural images from BSE SEM images usually indicate differences in elemental or phase composition of the alloy. However, point analysis (See Table 3) of EDS elements showed almost similar concentrations at all points observed in Fe-Mn-Al alloys with 0, 3, and 5 wt.% Al content. The FeMn-0Al alloy are consisting of Fe_3Mn_7 and Mn-carbide with a small concentration of Si. The concentration of Mn and C ratio was suggested as Mn_7C_3 or $Mn_{23}C_6$ phase while seen unclearly detected in the XRD result of Fig. 3.

In the FeMn-3Al alloys, the ratio of Fe, Mn, and Al content at points 1 and 2 is almost the same. It is composed of a mixture of Fe_3Mn_7, FeAl, and Mn-carbide phases. Likewise, in FeMn-5Al alloy, the Al content was detected to increase with the addition of 5 wt.% Al. The detected elements were predicted to be a mixture of Fe_3Mn_7, FeAl, Al_8Mn_5, and Mn-carbide phases.

Table 3. EDS point analysis of Fe-Mn-Al alloys: (a) FeMn-0Al, (b) FeMn-3Al, and (c) FeMn-5Al

	Point	Element (at.%)						Predicted phases
		Fe	Mn	Al	C	Si	O	
a	1	18.97	59.37	-	21.01	0.65	-	Fe_3Mn_7, Mn-carbide
	2	18.88	60.14	-	20.85	0.14	-	
	3	19.65	60.57	-	19.56	0.23	-	
	4	4.36	32.00	-	7.33	7.18	49.13	pore/oxide
b	1	9.44	40.67	21.42	28.21	0.26	-	Fe_3Mn_7, FeAl, Mn-carbide
	2	5.64	25.98	13.08	55.16	0.14	-	
	3	2.86	10.95	15.30	13.40	0.18	57.31	pore/oxide
c	1	5.76	38.02	26.33	29.76	0.14	-	Fe_3Mn_7, FeAl, Al_8Mn_5, Mn-carbide
	2	7.39	32.81	34.18	25.39	0.23	-	
	3	3.34	10.39	31.52	15.02	0.15	39.58	pore/oxide

The BSE image of Fig. 4 shows the presence of irregular black areas in all Fe-Mn-Al alloys as previously described. There are several possibilities for this area, namely pores, oxides, or a combination of these. In general, pores occur because there is not enough sintering due to several process variables as temperature and time, addition of elements, powder size, and others

[18]-[19]. High temperature can cause the evaporation of Mn during the sintering process, where it can sublimate at low temperature below the melting point [8], [15], [20]. The oxide formation may occur during the sintering process due to the high oxygen affinity of the alloying elements, which can absorb oxygen easily during powder synthesis. During milling, a significant oxidation of the particle surface can occur., oxygen can be trapped in the agglomerates, resulting in loss of ductility of the sintered sample [21]. As shown in Fig. 4, It can easily distinguish the presence of pores and oxides in sintered alloy before the oxidation test. The alloy elements are potentially oxidized during the sintering process at a vacuum pressure of about 0.5 mbar. Under these conditions, the elements that have a high affinity for oxygen to be oxidized, mostly.

The results of EDS analysis also indicate that the carbon content in all point areas is relatively high. Previous studies reported that the high carbon content may be due to the detection efficiency of light elements [22] and also on the surface of the sample, the carbon often accumulate during electron microscopy analysis [23]-[24].

It is visible from the SEM observation as shown in Fig. 4 that the Al-free alloy is denser compared to that of 3 and 5 wt.% Al alloys. Consequently, it is believed that the alloy microstructure will affect the mechanical properties of Fe-Mn-Al alloys.

3.2 Density and Hardness

The density and hardness of Fe-Mn-Al alloys with different Al content are presented in Fig. 5. The density and hardness of Fe-Mn-Al alloys decrease with the decrease of Mn and the increase of Al content.

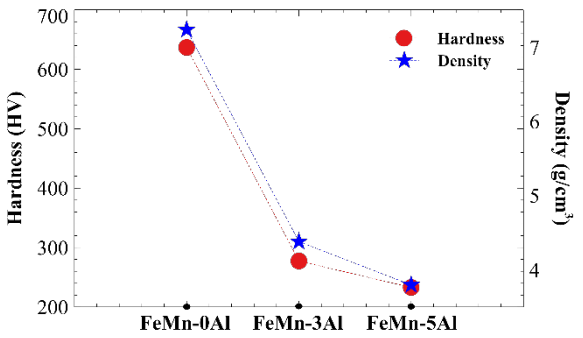

Figure 5. Density and Vickers hardness of Fe-Mn-Al alloys with different Al content

The density and hardness of FeMn-0Al alloy reached 7.127 g/cm^3 and 636.72 HV, respectively. This is reasonable when compared to pure Fe and Mn which have densities of 7.86 and 7.21 g/cm^3, respectively. On the contrary, the addition of 3 wt.% Al ($\rho \approx 2.70$ g/cm^3) leads to a decrease in density of about 4.380 g/cm^3 or almost two times lower than Al-free alloy. As Al concentration was increased to 5 wt.%, the measured density of the alloy is slightly lower than that of 3 wt% Al alloy which is 3.797 g/cm^3. Meanwhile, the hardness of the alloys decreases with the increase in Al content. It is found that the hardness of Fe-Mn-Al alloys decreases gradually to 277.37 and 232.89 HV by 3 and 5 wt.% Al addition, respectively. As with these findings, it is widely accepted that a more porous material reduces the density and hardness of the sample. This is consistent with the results of the metallographic observation described in Fig. 4. These results were correlated as reported by Rashidi et. al., [4] the hardness value is higher when manganese accumulated more in the alloys. Based on the density and properties, in general the addition of Al has been proposed to decrease the density [19], so as to further decrease the large void of the alloy [7]. In the sintering process, the addition of Al enhance material transport and increases atomic diffusion which leads to pores towards the surface of the sintered specimen [19]. This also increases the penetration of molten metal along grain boundaries. Furthermore, the addition of Al can increase sinterability and reduce the temperature of sintering process [25], which consequently increases the alloy's solubility and increases the Mn sublimation activity. The increase in Mn sublimation causes the formation of pores to increase until the end of the sintering process. At the sintering process, by adding 3 wt.% Al will possible the molten Al partially reacts with $FeMn_3$ phase to form FeAl phase. The addition of Al to 5 wt.%, except forming FeAl, molten Al also reacts with Mn and/or $FeMn_3$ to form Al_8Mn_5.

3.3 Kinetic Oxidation

The mass change of Fe-Mn-Al alloys after high temperature oxidation test at 800 °C for 8 cycles is shown in Fig. 6. Except FeMn-0Al alloys, based on the oxidation curve, it can be seen that the mass increase per unit surface area of each sample was caused by the formation of oxides during the oxidation test. It is clearly seen that Al addition significantly improved the oxidation resistance of Fe-Mn-Al alloys.

The mass gain per sample surface area of Fe-Mn-Al alloy without Al addition was dramatically decreased in the first cycle of oxidation at 800 °C, associated with a mass loss of the sample. This is due to that the sample was

break suddenly after the sample was taken out from the furnace for cooling (see Fig. 7(a)).

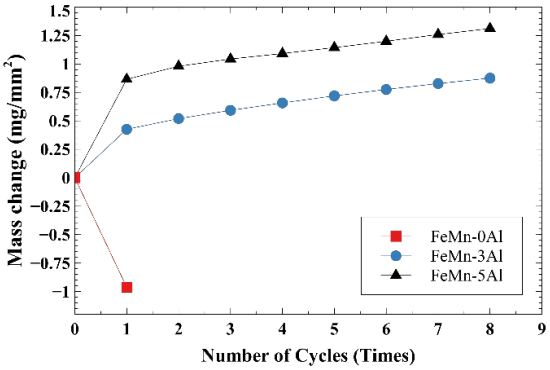

Figure 6. Oxidation curve of Fe-Mn-Al alloys after oxidation at 800 °C for 8 times

The brittle nature like a fractured surface can be observed. This deterioration and degradation could be due to the microstructure change at high temperatures [26]. It seems that there are some possible mechanisms contributing to the break of the sample during thermal shock cooling. FeMn-based alloys exhibit a shape memory effect undergoing fcc - hcp phase transformation, and there is a defect accumulation during temperature change [9]. The oxidation cycle may affect the phase strain at the heat-cooling cycle and phase reorientation. This happens and causes the accumulation of defects during the continued oxidation cycle. The mechanical properties of Fe-Mn steels are affected and depend on Mn content as reported by Kim et. al., [3] while as the Mn content increases, the ductile to brittle as the temperature changes.

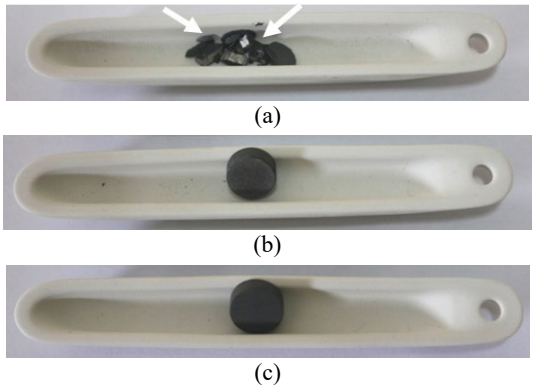

Fig. 7. Photograph of Fe-Mn-Al alloys with (a) 0, (b) 3, and (c) 5 Al after oxidation at 800 °C for 1 cycle

Some parts of the sample were break to the outside of alumina crucible, resulting in mass gain decreasing. For this reason, the high-temperature oxidation test of FeMn-0Al alloy was stopped in the first cycle. Interestingly, the aforesaid evidence doesn't occur in the Al-added alloy. It can be seen that the mass gain of the sample increase with the increase of Al concentration in the alloys (Fig. 6). The mass gain of 5 wt.% Al alloys is two time higher compared to that of 3 wt.% Al alloy.

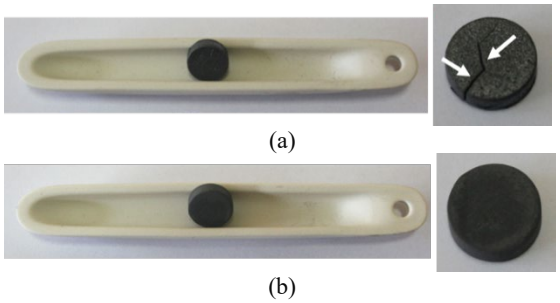

Figure 8. Photograph of Fe-Mn-Al alloys with (a) 3 and (b) 5 Al after oxidation at 800 °C for 8 cycles

Based on the results as presented above (see Fig. 8), it should be pointed out that although 3 wt.% Al alloy exhibit the lowest mass gain after exposure for 8 cycles at 800 °C, the alloy is susceptible to the oxidation induce crack formation.

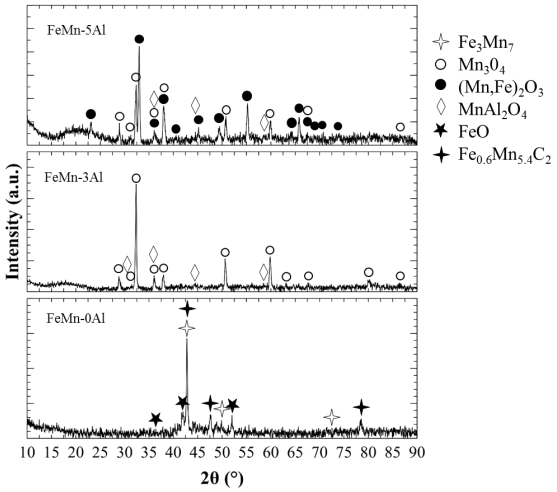

Figure 9. X-ray diffraction patterns of Fe-Mn-Al alloys with different content of Al after exposure at 800 °C for FeMn-0Al in 1 cycle, and FeMn-3Al and FeMn-5Al in 8 cycles

3.4 Phase Composition and Microstructure after Oxidation Test at 800 °C

The x-ray diffraction patterns of Fe-Mn-Al alloys after a high-temperature oxidation test at 800 °C was shown in Fig. 9. There are some different compositions of oxide scale formed on Fe-Mn-Al alloys after the oxidation test at 800 °C. The FeMn-0Al alloy forms mainly FeO scales. Since FeMn-0Al alloy gets a breakaway in the first cycle, the Fe_3Mn_7 phase was still detected, and carbide is $Fe_{0.6}Mn_{5.4}C_2$ like as XRD detected. The FeMn-3Al consists Mn_3O_4 and $MnAl_2O_4$ scales. Meanwhile, FeMn-5Al contains of Mn_3O_4, $MnAl_2O_4$, and $(Mn, Fe)_2O_3$ scales. Besides that, it looks like an increase of background in the 2θ range of 15 to 30 degrees which may the oxidized alloys have an amorphous phase.

Figure 10 shows the cross-sectional SEM images and EDS point analysis of Fe-Mn-Al alloys after the oxidation test at 800 °C for 8 cycles. While Figure 11 presents its EDS mapping analysis. Based on the contrast and brightness, the oxide layer can be divided into two main layers, namely the inner layer and the outer layer. Fe, Mn, Al, C, Si, and O elements are seen scattered in the oxide layer. The thickness of the oxide layer after exposure at 800 °C for 8 cycles, was from 50 to 60 µm and 40 to 50 µm on the FeMn-3Al and FeMn-5Al alloys, respectively.

Attention was directed to a contrast difference between the interface of the inner layer to the inside of the alloy as shown in Figure 10 (See yellow-dash arrow). This can be correlated with the BSE morphology of the cross-sectional Fe-Mn-Al alloys, especially for the Mn elements. This likely occurs an Mn depletion of the Fe-Mn-Al alloys. The Mn content increased from the inner layer towards the FeMn-3Al and 5Al alloys. It is as reported by Xu et. al., [20] Mn content increases parabolically, starting from the resin-sample interface of the sintered samples.

Based on Fig. 10, the microstructure had a random distribution from the interface scale to the inside of the alloys. Although they can be distinguished, by contrast, there are some areas that look the same but still contain other elements. The results of EDS point analysis were performed to examine the elemental composition of scales and the sintered alloys after oxidation as listed in Table 4. Furthermore, the predicted phases on those points were then confirmed by XRD and EDS mapping analysis.

Pont 1 on FeMn-3Al are composed mainly of Si, Al, Mn, Fe, and O. Thus, almost the same to point 1, point 2 mainly consists of Si, Fe, Mn, Al, and O. Point 1 and point 2 predicted to as SiO_2, and the mixture of (Fe, Mn, Al)-oxide. Point 3 and point 4 are composed of Mn, Fe, and O, and a small amount of Al and Si are predicted as Mn_3O_4 and $MnFe_2O_4$. The Si content in points 1 and 2 is higher than in points 3 and 4, while the Mn content is more at points 3 and 4. Based on the results, outer-layer is mainly consisted of the SiO_2 phase and the inner layer is Mn_3O_4. Meanwhile, a mixture of oxides (Fe, Mn, Al) as $MnAl_2O_4$ and Mn_3O_4 is spread on outer layer.

In FeMn-5Al alloy, point 1 in the outer layer is composed of Si, Al, Mn, Fe, and O which are predicted as SiO_2 and the mixed oxide of (Fe, Mn, Al). Elsewhere in the outer layer, point 2 contains Mn, Al, Si, Fe, and O. Although it contains mainly Mn, this area is still influenced by Si content as in point 1. Point 2 is predicted as Mn_3O_4, $MnAl_2O_4$, SiO_2, and a little amount of $MnFe_2O_4$. Point 3 containing a high concentration of Mn and O is predicted as Mn_3O_4. Whereas Point 4 is mainly composed of Mn, Al, O, and a small concentration of Fe that is predicted as Mn_3O_4 and Al_2O_3.

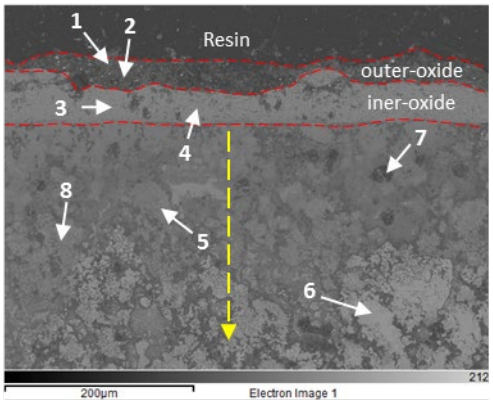

(a)

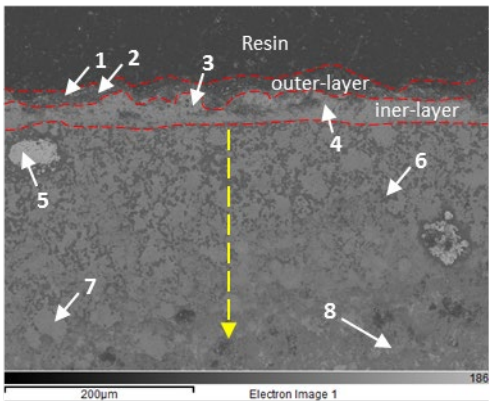

(b)

Figure 10. The cross-sectional SEM images and the corresponding EDS point analysis of (a) 3 and (b) 5 wt.% Al alloys after oxidation test at 800 °C for 8 cycles

Beneath the oxide layer there are oxygen concentrations at points (5, 6, 7, and 8), and (5, 6, and 7) in FeMn-3Al and FeMn-5Al alloys, respectively. This evidence indicates that there is internal oxidation occurs inside alloys. Firstly, during the initial oxidation due to the presence of pores oxygen freely diffuses into the alloy and reacts with the elements. The pores can become access or diffusion paths between the elements and reacting oxygen when the oxidation test is carried out at a temperature of 800 °C. This access is formed from an area called the depleted zone Mn as described previously.

The results of the EDS mapping analysis indicate the concentrations of Al and O have high contrast. These may react with each other to form Al-oxide, along with other elements. It is possible because Al has a high affinity to oxygen [12]. It is also confirmed from the EDS mapping of Fig. 11 that there are concentrations rich in Mn, Al, and O in FeMn-3Al and rich in Fe, Mn, Al, and O in FeMn-5Al under the inner oxide.

The addition of Al to Fe-Mn-Al alloys may encourage the formation of Al-oxides and/or their mixtures which then could become more of a barrier or barrier for the next diffusion process, so this causes the thickness of FeMn-5Al scales to be thinner than FeMn-3Al alloy. The previous studies report that an Al_2O_3 has a low oxygen diffusion rate, which can act as a barrier to oxygen diffusion [6], [13]. Although Al-oxide is not detected by XRD because it is not possible to measure deeper into the alloy, this is the reason why it does not form on the alloy surface even though the oxide is more protective when formed at the alloy surface or interface.

Table 4. EDS point analysis of Fe-Mn-Al alloys after oxidation test at 800 °C: (a) 0Al, (b) 3Al, and (c) 5Al

	Point	Element (at%)					Predicted phases
		Fe	Mn	Al	Si	O	
a	1	1.98	3.54	5.71	53.59	35.19	SiO_2, (Fe,Mn,Al) oxide
	2	5.75	5.13	4.12	50.03	34.96	
	3	8.31	31.24	0.79	0.05	59.62	Mn_3O_4, $MnFe_2O_4$
	4	7.32	29.84	0.83	0.06	61.94	
	5	10.02	20.88	10.79	0.16	58.15	(Fe,Mn,Al) oxide
	6	22.38	54.23	15.63	0.91	6.85	Fe_3Mn_7, Al_2O_3
	7	11.65	17.65	31.34	3.42	35.94	Fe_3Mn_7, Al_2O_3
	8	4.44	11.05	23.44	0.09	60.98	Fe_3Mn_7, Al_2O_3
b	1	8.59	11.24	15.15	23.03	41.99	SiO_2, (Fe,Mn,Al) oxide
	2	2.83	39.09	10.51	7.96	39.61	Mn_3O_4, $MnAl_2O_4$, SiO_2 $MnFe_2O_4$
	3	1.21	34.93	0.58	0.22	63.05	Mn_3O_4
	4	2.74	37.87	6.99	0.60	51.79	Mn_3O_4, Al_2O_3
	5	52.72	45.99	0.30	0.41	0.58	Fe_3Mn_7
	6	1.83	2.88	33.56	0.13	61.11	Al_2O_3
	7	7.66	20.12	11.78	0.20	60.25	Fe_3Mn_7, Al_2O_3
	8	2.86	11.72	24.10	0.14	61.18	Fe_3Mn_7, Al_2O_3

The difference contrast was also seen between Fe, Mn, and O concentrations in FeMn-3Al and FeMn-5Al which correspond to inner oxide layer. The presence of Fe, Mn, and O in the inner layer, suggests it is composed of $MnFe_2O_4$ scales. Besides that, the distribution of Mn, Al, and O in the outer layer can also be observed. As seen in Fig. 11, the Al distribution in FeMn-5Al is more clear than in the FeMn-3Al alloy. It can be correlated to the presence of the $MnAl_2O_4$ scale as detected by XRD. This is also confirmed as a mixture of (Fe, Mn, and Al)-oxide predicted on EDS point analysis. Kurokawa et. al., [14] report the addition of Al in Fe-Cr-Mn alloys increases oxidation resistance by the formation of spinel oxide $MnAl_2O_4$ which contributes to the suppression of pore formation.

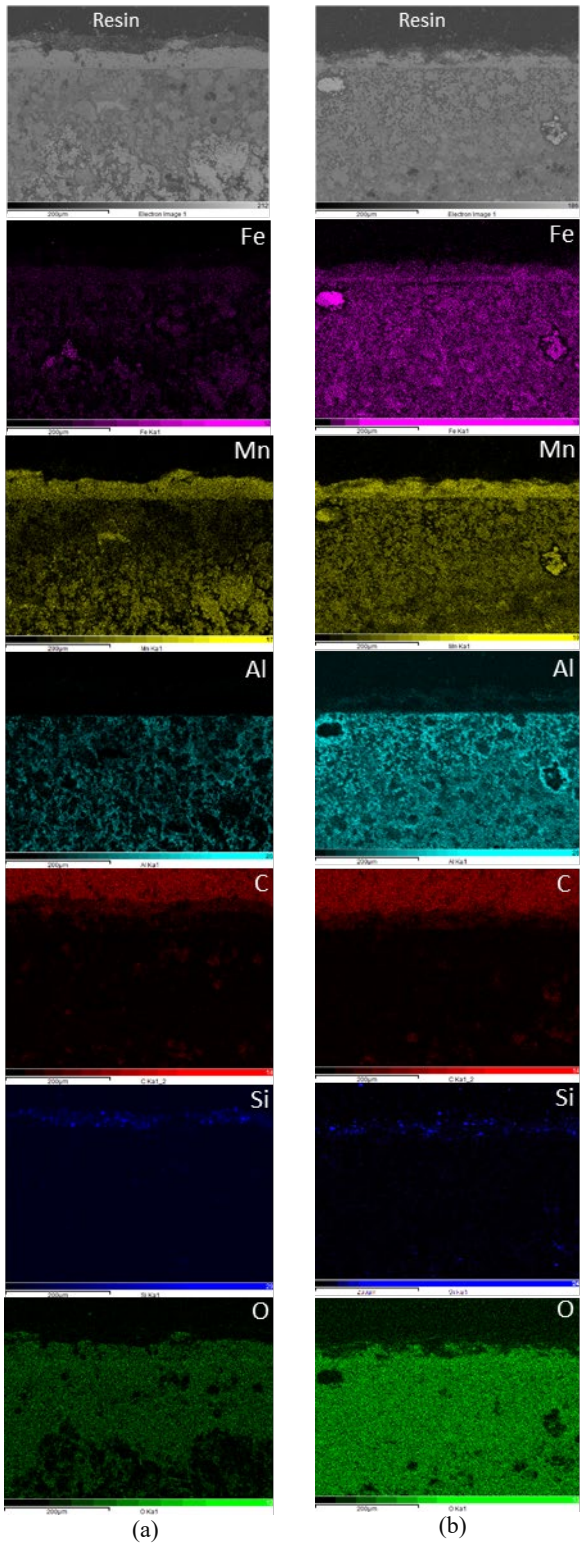

(a) (b)

Figure 11. BSE cross-sectional morphologies and EDS mapping of Fe-Mn-Al alloys with (a) 3 and (b) 5 wt.% Al content after oxidation at 800 °C for 8 cycles

The distribution of Si content in the outer layer can also be seen in Fig. 11. Si may have combined with Fe and Mn elements to form an oxide mixture. However, elemental point analysis reveals Si content, whereas XRD analysis does

not. It is feasible in the form of amorphous SiO_2, which appears as background noise in the XRD spectrum.

On the other hand, even though the O content is widely distributed, the distribution of C concentration tends to slightly decrease on the inside of the sintered sample after oxidation. Evaporation appears to occur when oxidation from the carbide phase reacts with oxygen to form CO and/or CO_2 gaseous, leaving the initial location and forming pores. It causes the formation of microcracks, resulting in a faster diffusion path [6]. Furthermore, the carbon oxidation decreases after the formation of the $MnAl_2O_4$, $MnFe_2O_4$, and Al_2O_3 scales, as do the oxidation times.

Based on the results of this study, it was found that the oxide layer formed on the FeMn-3Al alloy has the best oxidation resistance but breakaway oxidation occurs. The increase of 5 wt% Al content evident could prevent crack defects during high-temperature exposures at 800 °C due to the presence of Al-oxide or their oxide mixtures. The higher Al content provides more possibility of Al- oxide formation which can heal porous defects and enhance the prevention of carbon oxidation during high-temperature exposures. This is also the reason why the addition of Al has a significant contribution to the growth of scales.

4. CONCLUSION

In this study, the effect of Al addition on the structure, density, hardness, and high-temperature oxidation resistance of Fe-Mn-Al alloys has been presented and discussed. Based on the results obtained, the microstructure homogeneity of the Fe-Mn-Al alloy decrease with the increase of Al content. Irregular black area precipitates were found in Fe-Mn-Al alloys and their presence tends to increase with the addition of Al. The density and hardness of Fe-Mn-Al alloys decrease with the decrease of Mn and the increase of Al content. The Al addition leads to a significantly improved oxidation resistance of Fe-Mn-Al alloys. The Fe-Mn-Al alloy by 5 wt.% Al exhibits good resistance toward oxidation at 800 °C for 8 cyclic and had no cracking defects. Although shows a better oxidation curve than FeMn-5Al, the presence of cracks is found in FeMn-3Al alloy. During oxidation, the presence of the Al8Mn5 phase in the FeMn-5Al alloy causes the formation of Al-oxide and/or their mixture, which acts as a barrier and heals aporous defects.

ACKNOWLEDGMENT

The authors would like to thank the Research Center for Advanced Materials, National Research and Innovation Agency (BRIN) for providing processing and characterization facilities.

REFERENCES

[1] X. W. Zhou, M. E. Foster, and R. B. Sills, "An Fe-Ni-Cr embedded atom method potential for austenitic and ferritic systems," *J. Comput. Chem.*, vol. 39, no. 29, pp. 2420-2431, 2018. Doi: 10.1002/jcc.25573.

[2] M. B. Abuzriba and S. M. Musa, "Substitution for chromium and nickel in austenitic stainless steels," in *2nd International Multidisciplinary Microscopy and Microanalysis Congress*, vol. 164, E. K. Polychroniadis, A. Y. Oral, and M. Ozer, Eds. Cham: Springer International Publishing, 2015, pp. 205-214. Doi: 10.1007/978-3-319-16919-4_27.

[3] J.-S. Kim, S. Yong Shin, J. Eun Jung, J. Young Park, and Y. Won Chang, "Effects of tempering temperature on microstructure and tensile properties of Fe-12Mn steel," *Mater. Sci. Eng. A*, vol. 640, pp. 171-179, 2015. Doi: 10.1016/j.msea.2015.05.036.

[4] M. Mohd. Rashidi and Mohd. Hasbullah Idris, "Microstructure and mechanical properties of modified ductile Ni-resist with higher manganese content," *Mater. Sci. Eng. A*, vol. 574, pp. 226-234, 2013. Doi: 10.1016/j.msea.2013.02.038.

[5] A. Mondal, D. Pilone, A. Brotzu, and F. Felli, "Effect of heat treatment on mechanical properties of FeMnAlC alloys," *Procedia Struct. Integr.*, vol. 33, pp. 237-244, 2021. Doi: 10.1016/j.prostr.2021.10.029.

[6] W. Peng, Z. Wu, Y. Xu, Q. Ran, W. Xu, J. Li, and X. Xiao, "Internal oxidation behaviour of Fe-Mn-Al-C duplex light-weight steels with good combination of strength and ductility," *Corros. Sci.*, vol. 120, pp. 148-157, 2017. Doi: 10.1016/j.corsci.2017.03.005.

[7] J.-E. Jin and Y.-K. Lee, "Effects of Al on microstructure and tensile properties of C-bearing high Mn TWIP steel," *Acta Mater.*, vol. 60, no. 4, pp. 1680-1688, 2012. Doi: 10.1016/j.actamat.2011.12.004.

[8] A. Šalak, M. Selecká, and R. Bureš, "Manganese in ferrous powder metallurgy," *Powder Metall. Prog.*, no. 1,

pp. 19, 2001.
[9] M. E. Evard, A. A. Volkov, F. S. Belyaev, A. D. Ignatova, and N. A. Volkova, "Microstructural modelling of plastic deformation and defects accumulation in FeMn-based shape memory alloys," *Procedia Struct. Integr.*, vol. 2, pp. 1546-1552, 2016. Doi: 10.1016/j.prostr.2016.06.196.
[10] P. Chowdhury, D. Canadinc, and H. Sehitoglu, "On deformation behavior of Fe-Mn based structural alloys," *Mater. Sci. Eng. R Rep.*, vol. 122, pp. 1-28, 2017. Doi: 10.1016/j.mser.2017.09.002.
[11] L. Stratil, V. Horník, P. Dymáček, P. Roupcová, and J. Svoboda, "The influence of aluminum content on oxidation resistance of new-generation ODS alloy at 1200 °C," *Metals*, vol. 10, no. 11, pp. 1478, 2020. Doi: 10.3390/met10111478.
[12] J. Gao, Shixi Liu, Xiaojun Wang, and Wenbin Wang, "Effects of high oxygen-affinity elements on microstructure of Cu-Cr alloy ingots," in *2013 2nd International Conference on Electric Power Equipment - Switching Technology (ICEPE-ST)*, Matsue-city, Japan, pp. 1-4, 2013. Doi: 10.1109/ICEPE-ST.2013.6804309.
[13] X. Zhang, Z. Deng, H. Li, J. Mao, C. Deng, C. Deng, S. Niu, W. Chen, J. Song, J. Fan, M. Liu, and K. Zhou, "Al_2O_3-modified PS-PVD 7YSZ thermal barrier coatings for advanced gas-turbine engines," *Npj Mater. Degrad.*, vol. 4, no. 1, pp. 31, 2020. Doi: 10.1038/s41529-020-00134-5.
[14] K. Kurokawa, Y. Mizuta, and H. Takahashi, "Oxidation of Fe-Cr-Mn-Al stainless steels," in *High Temperature Corrosion of Advanced Materials and Protective Coatings*, Elsevier, pp. 91-96, 1992. Doi: 10.1016/B978-0-444-88970-6.50015-4.
[15] A. Šalak and M. Selecká, "Thermodynamic conditions for the Mn–O system in sintering of manganese steels," in *Manganese in Powder Metallurgy Steels*, Cambridge: Cambridge International Science Publishing Ltd., pp. 5-21, 2012. Doi: 10.1007/978-1-907343-75-9_2.
[16] B.-D. You, B.-W. Lee, and J.-J. Pak, "Manganese loss during the oxygen refining of high-carbon ferromanganese melts," *Met. Mater.*, vol. 5, no. 5, pp. 497-502, 1999. Doi: 10.1007/BF03026165.
[17] S. T. Oyama, Ed., *The Chemistry of Transition Metal Carbides and Nitrides*. Dordrecht: Springer Netherlands, pp. 530, 1996. Doi: 10.1007/978-94-009-1565-7.
[18] N. Kurgan, "Effect of porosity and density on the mechanical and microstructural properties of sintered 316L stainless steel implant materials," *Mater. Des.*, vol. 55, pp. 235-241, 2014. Doi: 10.1016/j.matdes.2013.09.058.
[19] H. Sazegaran, H. Bahari, A. M. Naserian-Nik, and F. Khorramshahi, "Archives of metallurgy and materials archives of metallurgy and materials," vol. 67, no. 1, pp. 105-111, 2022. Doi: 10.24425/AMM.2022.137478.
[20] Z. Xu, M. Hodgson, K. Chang, G. Chen, X. Yuan, and P. Cao, "Effect of sintering time on the densification, microstructure, weight loss and tensile properties of a powder metallurgical Fe-Mn-Si Alloy," *Metals*, vol. 7, no. 3, pp. 81, 2017. Doi: 10.3390/met7030081.
[21] A. Bolsonella, F. Naimi, O. Heintz, T. Tricone, H. Couque, and F. Bernard, "Influence of oxygen induced during high-energy ball milling process on the mechanical properties of sintered nickel by SPS," *J. Alloys Compd.*, vol. 856, pp. 157869, 2021. Doi: 10.1016/j.jallcom.2020.157869.
[22] F. C. Miguens, M. L. d. Oliveira, R. V. Marins, and L. D. d. Lacerda, "A new protocol to detect light elements in estuarine sediments by X-ray microanalysis (SEM/EDS)," *J. Electron Microsc. (Tokyo)*, vol. 59, no. 5, pp. 437-446, 2010. Doi: 10.1093/jmicro/dfq013.
[23] J. Konopka and T. F. Scientific, "Options for quantitative analysis of light elements by SEM/EDS," Technical Note, pp. 1-2, 2013.
[24] L. L. A. Nisa, B. Hermanto, S. Aritonang, M. T. E. Manawan, and T. Sudiro, "Mechanical properties and high-temperature oxidation of (WC-12Co) + $MoSi_2$ hardmetals," *Int. J. Refract. Met. Hard Mater.*, vol. 109, pp. 10, 2022. Doi : 10.1016/j.ijrmhm.2022.105987
[25] H. Ghezelbash, A. Zeinali, N. Ehsani, and H. R. Baharvandi, "The effect of aluminum additive on pressureless sintering of SiC," *J. Aust. Ceram. Soc.*, vol. 55, no. 4, pp. 903-911, 2019. Doi: 10.1007/s41779-019-00310-0.
[26] A. M. Babakr, A. Al-Ahmari, K. Al-

Jumayiah, and F. Habiby, "Sigma phase formation and embrittlement of cast iron-chromium-nickel (Fe-Cr-Ni) alloys," *J. Miner. Mater. Charact. Eng.*, vol. 07, no. 02, pp. 127-145, 2008. Doi: 10.4236/jmmce.2008.72011.

AUTHOR INDEX

SUBJECT INDEX